Alma Mater Studiorum – Università di Bologna

DOTTORATO DI RICERCA IN

Meccanica e scienze avanzate dell'ingegneria
Ciclo XXVI

Settore Concorsuale di afferenza: 09/A1

Settore Scientifico disciplinare: ING-IND/05

TITOLO TESI

ENHANCEMENT OF TRAJECTORY DETERMINATION OF ORBITER SPACECRAFT BY USING PAIRS OF PLANETARY OPTICAL IMAGES

Presentata da: **Davide Silvestri**

Coordinatore Dottorato	**Relatore**
Prof. Vincenzo Parenti Castelli	**Prof. Paolo Tortora**

Esame finale anno 2014

“I can live with doubt and uncertainty. I think it's much more interesting to live not knowing than to have answers which might be wrong.”

Richard Phillips Feynman

Summary

The subject of the present thesis is about the enhancement of orbiter spacecraft navigation capabilities obtained by the standard radiometric link, taking advantage of an imaging payload and making use of a novel definition of optical measurements. An ESA Mission to Mercury called BepiColombo, was selected as a reference case for this study, and in particular its Mercury Planetary Orbiter (MPO), because of the presence of SIMBIO-SYS, an instrument suite part of the MPO payload, capable of acquiring high resolution images of the surface of Mercury.
The use of optical measurements for navigation, can provide complementary informations with respect to Doppler, for enhanced performances or a relaxation of the radio tracking requisites in term of ground station schedule.
Classical optical techniques based on centroids, limbs or landmarks, were the base to a novel idea for optical navigation, inspired by concepts of stereoscopic vision. In brief, the relation between two overlapped images acquired by a nadir pointed orbiter spacecraft at different times, was defined, and this information was then formulated into an optical measurement, to be processed by a navigation filter.
The formulation of this novel optical observable is presented, moreover the analysis of the possible impact on the mission budget and images scheduling is addressed.
Simulations are conducted using an orbit determination software already in use for spacecraft navigation in which the proposed optical measurements were implemented and the final results are given.

.

Sommario

Il soggetto della presente tesi riguarda la navigazione di sonde orbitanti attorno a pianeti o lune del Sistema Solare e in particolare l'integrazione alle classiche misure radiometriche dell'informazione aggiuntiva fornita da un *payload* ottico, per la quale è stata data definita una nuova tipologia di osservabili ottiche per la navigazione spaziale. La missione BepiColombo dell'Agenzia Spaziale Europea (ESA) diretta a Mercurio è stata utilizzata come riferimento per le simulazioni perché questa missione comprende una sonda planetaria orbitante chiamata MPO, dotata di uno strumento per l'acquisizione di immagini ad alta risoluzione della superficie di Mercurio, SIMBIO-SYS che bene si presta ai requisiti della metodologia proposta.
L'utilizzo di misure ottiche per la navigazione, può fornire informazioni complementari alle classiche misure Doppler, permettendo di ottenere possibili miglioramenti delle performance o un rilassamento dei vincoli richiesti per la pianificazione di periodi di tracciamento radio delle stazioni di terra.
Tecniche di navigazione ottica classica basate su centroidi, bordi dei target o punti salienti sono stati la base per lo sviluppo di una nuova tecnica di navigazione ottica, ispirata ai concetti di visione stereoscopica. In breve, la relazione tra due immagini sovrapposte, acquisite da una sonda orbitante a differenti istanti, che punta verso il nadir, è stata definita, e la sua informazione è stata formulata sotto forma di misure ottiche, processabili da un filtro di navigazione.
La formulazione di questa tipologia differente di osservabili ottiche è presentata. Inoltre l'analisi di un possibile impatto sul budget di missione ed eventuali soluzioni per la pianificazione di immagini per questa metodologia, sono affrontati.
Una serie di simulazioni sono state effettuate, utilizzando un software di determinazione orbitale già utilizzato per navigazione di sonde interplanetarie, nel quale sono state integrate le osservabili ottiche proposte e i risultati ottenuti sono presentati.

Acknowledgments

I would like to thanks my family for the support, Prof. Paolo Tortora and all friends that contributed to this research, directly and indirectly.

Contents

List of Figures

List of Tables

Nomenclature

Abbreviations

AOCS	Attitude Orbit Control System
AME	Absolute Measurement Error
APE	Absolute Pointing Error
BELA	BepiColombo Laser Altimeter
CP	Corner Point
CCD	Charged-Coupled Device
DSN	Deep Space Network
DN	Data Number
DTM	Digital Terrain Model
DEM	Digital Elevation Model
DDOR	Delta-Differential One-Way Range
ESA	European Space Agency
ESTRACK	European Space Tracking
HRIC	High Resolution Imaging Channel
ISA	Italian Spring Accelerometer
ISS	Imaging Science Subsystem
JAXA	Japan Aerospace Exploration Agency
LKT	Lucas-Kanadé-Tomasi
MERMAG	Mercury Magnetometer
MPO	Mercury Planetary Orbiter
MMO	Mercury Magnetospheric Orbiter
MFL	Multi-Frequency Link
NEAR	Near Earth Asteroid Rendezvous
NASA	National Aeronautics and Space Administration
NAC	Narrow Angle Camera
NAIF	NASA's Navigation and Ancillary Information Facility
OpNAV	Optical Navigation
OTM	Orbit Trim Maneuver
ODP	Orbit Determination Program
PM	Pattern Matching
RANSAC	Random Sample Consensus
RU	Range Units
SEP	Sun-Earth-Probe Angle
SIMBIO-SYS	Spectrometers and Imagers for MPO BepiColombo Integrated Observatory SYStem
SLAM	Simultaneous Localization and Mapping
SIFT	Scale Invariant Feature Transform
SRP	Solar Radiation Pressure
SURF	Speeded Up Robust Features
SAR	Synthetic Aperture Radar
TCM	Trajectory Correction Maneuver
VLBI	Very Long Baseline Interferometry

WAC	Wide Angle Camera
WBRS	Wide Band Ranging System

1 Introduction

In 2005, the University of Bologna, financed a researched based on the feasibility of an attitude sensor, capable of estimating the tri-axial orientation of a Terrestrial spacecraft. The proposed approach, renamed STARS (Bevilacqua, 2010), was to acquire, on orbit, with an high resolution camera, the images of Earth surface in the optical spectrum and to elaborate them in pairs to rebuild the complete attitude of the satellite.
Successively the Radio Science laboratory of the University of Bologna begun a research project, about the estimation of the rotational state and, in particular in the estimation of the obliquity of Mercury by means of the use of high resolution images. The project, is based on the use of a series of pair of images, spreaded in an optimized way, on the surface of Mercury and processed by an hoc estimator (Milani, 2001).
The subject of the present research, applies to the mission BepiColombo and exploits the concepts of the research developed by STARS for the evaluation of the impact of pairs of high resolution overlapped images for the navigation of orbiter spacecraft around the Planets or Moons of the Solar System, and deeply intertwined with the field explored by the rotation experiment of BepiColombo, as the research of crossovers in the field of view of the camera for the planning of the acquisition of couples of images.
It is important to be noted that, diversely from what is done in case of probes data processing for the extraction of scientific data, navigation teams must constraints on robust and quick procedures and algorithms for the upgrade of the probe state as new measurements arrives. Almost real-time systems are required in such a way that possible divergences from the reference trajectory may be promptly corrected.
The opportunity of using images for the navigation, lies therefore in the possibility of being easily processed and implemented in a navigation software, producing navigation benefits in a time coherent to the one requested by standard procedures.
For the Cassini probe (a JPL/NASA mission orbiting around Saturn) an optical navigation methodology, called OpNAV, is used, that satisfies the aforementioned requirements and is used for navigation (Gillam S., 2008).
This typology of measurements is extracted from images which includes a close-up of one or more Moons of Saturn over a background of known stars, for which the direction on the celestial sphere is known with high accuracy thanks to star catalogs.
The information is therefore angular but in order to use this information, the moon should be sufficiently small to occupy only a little portion of the field of view of the navigation camera. This kind of information is important for the update of Saturn Moons ephemerides, showing an important role in spacecraft navigation.
The Dawn probe had used instead a series of images at different altitudes of the Vesta, highly unknown asteroid, to characterize, at various steps, both the rotational state of this celestial body, both its gravitational and topographical model, with an iterative procedure. This methodology is necessary for highly uncertain bodies and requires the definition of a series of distributed landmarks around its surface (which order number may be has high as hundred points).
These coordinates, defined in a body-fixed reference frame, are included in the estimation filter, providing moreover, an elevation model, that for an asteroid is highly inhomogeneous. In this case, it is necessary a complex ad hoc system, capable of estimating an high number of georeferenced points, extracted from images, and then comparing them with reference images, as part of a global

orbit determination process of the probe (Owen, 2001). From the point of view of the estimation, the computational power required is higher and possibly subject to degradation effects due to the high number of parameters in the play.
A possible trade-off between the two aforementioned methodologies is presented which fits in an intermediate mission scenario, in particular, for an orbiter spacecraft around smooth moons or rocky planets, therefore excluding highly inhomogeneous asteroids or bodies with an haze or an atmosphere, and with an high resolution optical payload (in terms of ground resolution), it is possible to schedule the acquisition of pairs of images and use them to assist navigation, integrating the information on the line of sight Earth/Probe given by Doppler measurements with the local Target/Probe geometrical informations. The constraint given by an information that relates two images acquired at different times through the orbit, become an orbital constraint information and needs not to cope with the estimation of absolute landmarks therefore reducing the estimation burden.
In this field, MPO probe is a perfect candidate for the evaluation of the impact of this methodology because it carries the High Resolution Imaging Channel HRIC, part of the instrument SIMBIO-SYS, which purpose it to generate an high resolution map of Mercury.
The fields explored in the course of this PhD thesis are, the planning of image acquisitions for this navigation approach, the correlation of the images for the extraction of observed optical measurements, the mathematical formulation of the optical observables and partial derivatives with respect to different parameters, estimated or considered in the estimation filter and finally the development of a simulation environment in which the methodology was validated and its impact in navigation evaluated in various cases, showed in the final chapter.
This PhD research, was developed at the Radio Science Laboratory of the University of Bologna and for a six month stage at the NASA Jet Propulsion Laboratory.

Please feel free to contact the Author at d.silvestri@unibo if you have suggestions or to obtain the most updater revision of this Thesis.

2 Basics of Spacecraft Navigation

Spacecraft navigation, is referred both to satellites in Earth Orbit and deep space probes traveling through the solar system, aided by a variety of measurements.
The main objectives when dealing with a spacecraft are the near real-time estimation and prediction of the trajectory and the planning of the engine burns for maintaining the reference trajectory, that is the trajectory defined in a design phase, optimizing the trade-off between science objectives and costs.
The spacecraft position and velocity, usually referred as its state, can only be inferred by observing in a certain way, i.e by means of measurements. Primarily used in this field are:

- Range measurements from Earth Stations to the Spacecraft as a time delay
- Spacecraft Line-Of-Sight velocity directly toward or away from Earth observing station, called also Doppler measurement
- Spacecraft angular position as seen from Earth, as ΔDOR or VLBI measurements
- Optical measurement using on-board cameras or by means of ground-based lasers pointed to the spacecraft

A combination of these measurements is selected based on the characteristics of the mission as the spacecraft category and the mission scenario. During the operative phase of the mission a schedule is generate providing a periodic tracking coverage of the spacecraft. During cruise, the journey from Earth to the target, a spacecraft is generally supported by Range and Doppler measurements, then the target approach phase follows and these Earth-based measurements may be augmented with complementary optical measurements relatives to the target planet (or one of its satellites) against a star background, for which we have a very accurate database as the Tycho-2 catalogue. t
The support of optical observables is explained by the fact that the measurement is between the spacecraft position relative to the target, instead of the spacecraft state with respect to the Earth-based Station. One of the best examples was the case of the NASA Voyager 2 spacecraft encounter with Neptune. During this phase of the mission, classical radiometric measurements were used for the estimation of the spacecraft in the line-of-sight direction while accurate estimation of the cross-line-of-sight direction was entirely dependent upon optical observations of Neptune and its satellites (Riedel, 1989). There are also exceptions as only radio missions or automatic navigation systems that relied only on optical measurements (Riedel, 2000).
The more the necessity of exploring asteroids or reaching for far distance, the higher the added value given by measurements independent by the distance covered between Earth and the Probe.
But navigation is not only collecting measurements, but also a deep understading of the Solar System dynamics and the environment impacting on measurements and the probe. In brief, to navigate is the process in which measurements and a sufficiently complete model of the dynamic of the probe and its surrounding are elaborated in a fairly complex filtering to output a statistical description of where the spacecraft is at a certain epoch and with what uncertainty. This process is called orbit determination.
The main informations required for the process of orbit determination of a probe, depends on the effects that perturb its trajectory, the effects that acts on the measurements and eventual calibrations and, since most of the measurements used for spacecraft navigation, uses an Earth-based link, also a very accurate knowledge of the Earth motion, rotation and deformation is needed.
To evaluate the goodness of the model, a comparison is done between the observed measurements and the measurements computed with models. the comparison provides residuals, differences between the two kind of measurements. If the residuals are zero mean and with a white noise distribu-

tion due to uncorrelated measurement errors, the conclusion is that the model and the trajectory of the spacecraft are well known for the noise level of the observed measurements otherwise, if deterministic signals (signatures) are superimposed in the residuals, something in the model or in the parameters that enters the modek, is wrong. The orbit determination program normally uses iterations to compute linear corrections to apply to the parameters of the models in a weighted linear least-squares estimation, and to try to converge to a set of corrected parameters that fits the observed measurements. The optimal solution is defined as the set of parameters that minimizes the weighted sum of squares of residuals. If this condition is not reached, the knowledge of the model may be not sufficiently accurate and better models may be activated.

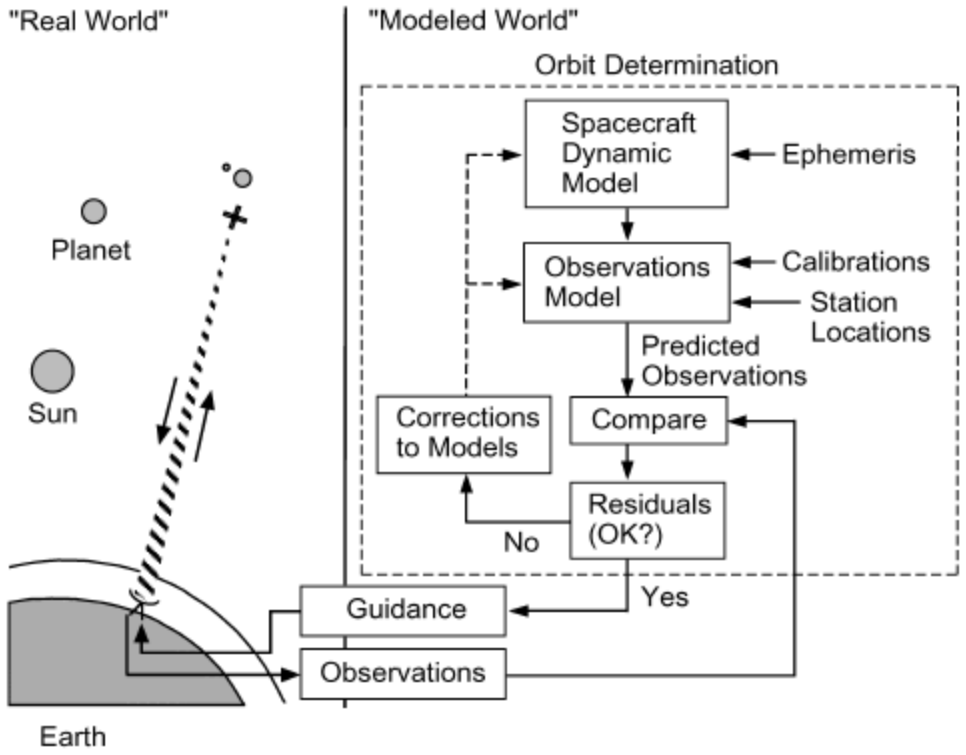

Figure 1 Orbit determination procedure

Once the trajectory solution is reliable, navigators can generate guidance commands to correct the spacecraft trajectory if necessary. This process is continuously iterated.

The main measurements used for deep space navigation are extracted from an Earth-based coherent radiometric link, as Doppler and range. The tracking link is made with internationally allocated frequency bands at X-Band and Ka-Band. The Doppler measurement comes directly from the carrier of the radiometric signal, while range is obtained with a ranging signal mixed into the carrier. Both these measurements can be used one-way, two-way or three-way. the selection of one of these solutions depends on the level of accuracy required. Indeed a two-way signal, is a signal transmitted from Earth using an ultra stable clock (Maser) used to generate the transmitted frequency. This frequency is received by the spacecraft, multiplied by a transponding ratio to avoid interference, and retransmitted back to Earth, in coherent mode. Otherwise, in a one-way link, is the spacecraft that uses an internal clock (Ultrastable Oscillator) required for the generation of the downlink frequency, but as the clock suffer of drift and fluctuations, similarly will be the downlink frequency that will not be as stable as would have been using a two-way coherent mode, contributing to a signal degradation.

The move toward higher frequencies is driven by the requirement in terms of accuracy of the signal. in fact dispersive effects, i.e. frequency dependent degrading effects, are reduced when raising the frequency by a factor of $\sqrt{f}$. Typical dispersive effects are due to charged particles in the ionosphere and solar plasma.
Higher frequencies means also that the telemetry can have an higher download data rate, the advantages are evident in case of missions with on-board high resolution cameras. The bottleneck of the downlink throughput is clearly a key element in the design of some deep space missions. For example the annual estimated data volume for the BepiColombo MPO Spacecraft of about 1550 Gigabit (Fluente De La, 2013).

Another very accurate measurement comes from the spacecraft position in the sky relative to a quasar. This methodology is called VLBI (Very Long Baseline Interferometry). This observation requires two stations usually in two different continents, to obtain a very long baseline between the two. The two stations track the spacecraft simultaneously then, they change target, pointing toward a quasar (known with very high precision). The correlation of the signals yields a very accurate triangulation from which the angular position is inferred (Thornton, s.d.).

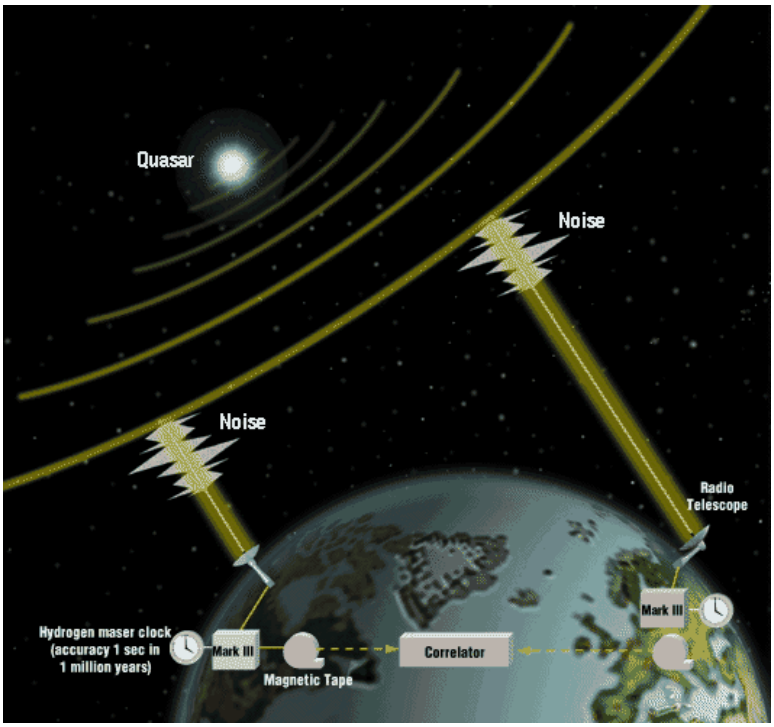

Figure 2 VLBI methodology

2.1 Radiometric measurements

The typical allocated frequencies used for modern deep space communication are showed in the following table

Table 1Allocated Deep Space Frequencies

Band	Uplink Frequency [GHz]	Downlink Frequency [GHz]
X	7.145 – 7.19	8.4-8.45
Ka	34.2-34.7	31.8-32.3

The ground station network is composed primarily by NASA's Deep Space Network (DSN) and ESA's ESTRACK. Those stations are distributed around the globe in such a way they cover most of the emisphere reducing the time of shadowing due to the rotation of the planet, a seasonal change of emisphere, and so on.
The coherency is obtained multiplying the on-board received frequency by a transponding ratio, typical values for this ratio are showed in the following table

Table 2 Transponding ratios

Uplink	Downlink		
S – band	240/221	880/221	3344/221
X – band	240/749	880/749	3344/749
Ka – band	240/3599	880/3599	3344/3599

2.1.1 Range

Spacecraft range is measured by the round trip transit time of a ranging signal generated at one of the deep space stations. A ranging signal, consisting of a sequence of sinusoidal tones derived from the station frequency standard, is phase modulated onto the transmitted carrier signal. The spacecraft receiver locks on and tracks the uplink carrier via a phase-locked loop that produces a reference signal coherent with the uplink carrier. this reference signal is used to demodulate the ranging signal, which is then passed through a low-pass filter, currently with an upper cutoff frequency of less than 2 MHz (Thornton, s.d.).The ranging signal is phase modulated onto the downlink carrier, a signal coherent with the uplink but offset in frequency. A phase-locked loop at the receiving station produces a reference signal coherent with the received signal. this reference signal is used by the ranging assembly to demodulate the downlink signal. The received range code is compared against a model of the transmitted range code to determine the round trip transit time. range measurements are quantized in steps referred to as range units (RU). The size of a n RU depends on the frequency of the highest component of the code and is currently about 28 cm. Another ranging capability uses a pseud-random noise code rather than a sequence of tones. this code will ensure more efficient use of the downlink power.

2.1.2 Doppler

an approximate expression for the received frequency from a spacecraft receding from Earth is

$$f_R = \left(1 - \frac{\dot{\rho}}{c}\right)\frac{1}{f_T} \quad (1)$$

where $\dot{\rho}$ is the spacecraft instantaneous slant range rate and f_T is the transmitted carrier frequency from the spacecraft.
The Doppler measurement thus provides information on the spacecraft topocentric range rate, or the range change over a count time T_c.
The most accurate ranging and Doppler measurements are obtained via a two-way tracking mode for which the transmitting and receiving stations, and hence the frequency standards, are the same. For some missions, this configuration is impossible due to the great distance, for a two-way tracking mode, we will have a doubled contribute of Doppler shift, the one affecting the uplink and the one affecting the downlink.

2.2 Orbit determination procedure

Orbit determination is based on a linear iterative weighted multidimensional least-square filter. The set of observed measurements z_o can be also computed by a mathematical model that depend on a custom set of parameters.

$$z_T = z(q_T) \quad (2)$$

where the true value of the parameters may be seen as the actual value plus some unknown correction.

$$q_T = q_0 + \Delta q \quad (3)$$

then the set of computed values based on a nominal value of the parameters is

$$z_c = z(q_0) \quad (4)$$

Expanding the true observable in a Taylor serie gives

$$z_T = z_c + \frac{\partial z}{\partial q}\Big|_{x=x_c} \Delta q \quad (5)$$

rewritten as

$$\frac{\partial z}{\partial q}\Big|_{x=x_c} \Delta q = z_T - z_c \quad (6)$$

now replacing the "true" observables with the observed observables gives a residual vector that can be now computed $z_o - z_c = b$
This can be seen as a set of condition equations. the matrix of partials of observables is called A.

$$A\Delta q = b \quad (7)$$

If M is the number of observables and N is the number of parameters to correct and M> N, the problem is over determined and the solution can be found minimizing the root square sum of the residuals $\|b\|^2$, or in other form, premultiplying the former equation by its transpose

$$A^T A\Delta q = A^T b \quad (8)$$

which is a set of N normal equations that can be inverted to solve for Δq

$$\Delta q = (A^T A)^{-1} A^T b \quad (9)$$

each condition equation can then be divided by the measurement uncertainty $S = diag\left(\frac{1}{\sigma_1}, ..\right)$. The condition equation becomes now dimensionless

$$SA\Delta q = Sb \quad (10)$$

in normal form

$$(A^T WA)\Delta q = A^T Wb \quad (11)$$

where W is the weighting matrix.
The information matrix is $\Lambda = A^T W A$, and its inverse is the covariance matrix $P = \Lambda^{-1}$
It is important to observe that P is independent of the residuals, and a covariance analysis can be performed before measurements are made.
The next step is to add an apriori covariance to the problem, because the parameter should not change too much with respect to the initial guess given. this additional constrain can be viewed also as an additional set of observations (Tapley, 2004).
A well-known problem is the instability of the inversion, and of near-singular information matrices or Kalman techniques that possibly produce negative elements on the diagonal of the covariance matrix.
The solution is to work with a square root of either the covariance matrix or the information matrix that gives no loss of precision and no possibility of negative eigenvalues. This methodology is called factorization and the U-D filter is an example

$$P = UDU^T \quad (12)$$

where P is decomposed in an upper triangular matrix U and diagonal matrix D. this methodology permits also to process measurements one at a time.
A square root information filter SRIF works instead on the information matrix and uses

$$P^{-1} = RR^T \quad (13)$$

using the Householder transformation to re-triangularize R (Bierman, 1977).
To complete the spectrum of orbit determination filtering techniques, one have often to deal with families of related parameters as stochastic accelerations, pointing angles of images and so on. the total number of these parameters is not generally known in advance and each condition equation has partials with respect to only one parameter in each family. In the filtering process only one parameter per family is used, and going backward to improve estimates of earlier values of stochastic parameters is called smoothing.
Consider parameters are used in the estimation when the uncertainty associated is known but the estimation is not desired. to consider a parameter is sufficient to include its covariance matrix inside an augmented covariance matrix, but when the parameters correction is computed and reiterated, the correction of the consider parameters is reinitialized to zero. With the definition of consider parameters is associated the sensitivity matrix, composed by the partials of solve for parameters x with respect to consider parameters y.

$$S_{xy} = \frac{\partial \hat{x}}{\partial y} = -\Gamma_x^0 (A_x^T W A_y) \quad (14)$$

where

$$\Gamma_x^0 = (A_x^T W A_x + P_x)^{-1} \quad (15)$$

with the aforementioned square root formulation

$$\Lambda_x = R_x^T R_x \quad (16)$$

$$S_{xy} = -R_x^{-1} R_{xy} \quad (17)$$

The influence of a consider parameter to the solve-for parameters is resulted from the perturbation matrix where the error in the estimated solve-for parameters due to a one-sigma error in a set of consider parameters y is

$$P_{xy} = S_{xy}\bar{\sigma}_y \quad (18)$$

with

$$\bar{\sigma}_y = diag\left(\Gamma_y^{0.5}\right) \quad (19)$$

2.3 Classical optical navigation

It was already proven in past missions that the use of a camera for optical navigation as a support for radiometric tracking with Earth or as an autonomous system is a successful choice and in some situation a requirement. Moreover radiometric tracking is also expensive and suffer of shadowing periods due to geometry of the Earth-Probe-Target system and the light time is also a constraint for extremely distant spacecraft as it can for a Pluto mission (10 hours). In short, in the space field, the capability of having an extended portfolio of measurement instrument and therefore typologies of informations, can open new frontiers for deep space mission otherwise impossible to realize from a technological or economical point of view.
Informations extracted from images and already used in one of the Orbit Determination Software that the University of Bologna can access for science is Monte of the Jet Propulsion Laboratory, are the one obtained in cruise and during nominal operations, targeting planets or moons, seen as points or little objects in a background of star, or analyzing the limb of the body during the approach. Another experimental methodology is used for low orbit or descent. In this latter case it is necessary a complex orbit determination setup able to estimate in parallel a batch of georeferenced landmarks.

2.3.1 Landmark navigation for Asteroids

The first use of optical landmark navigation using craters has been used operationally at first by the Near Earth Asteroid Rendezvous (NEAR) mission. Eros was reached in 2000 by NEAR spacecraft launched in 1996. Used for support in Doppler navigation for close flybys and low altitude orbits on a very undetermined body as it can be an asteroid with also a very complex rotational state. Tracking of individual landmarks given by craters detection was done, enabling orbit determination accuracies on the order of the camera resolution of meters exceeding the accuracy that could be obtained from radiometric data alone at that time. At that time the entire process was done manually (Cheng Yang, 2002).

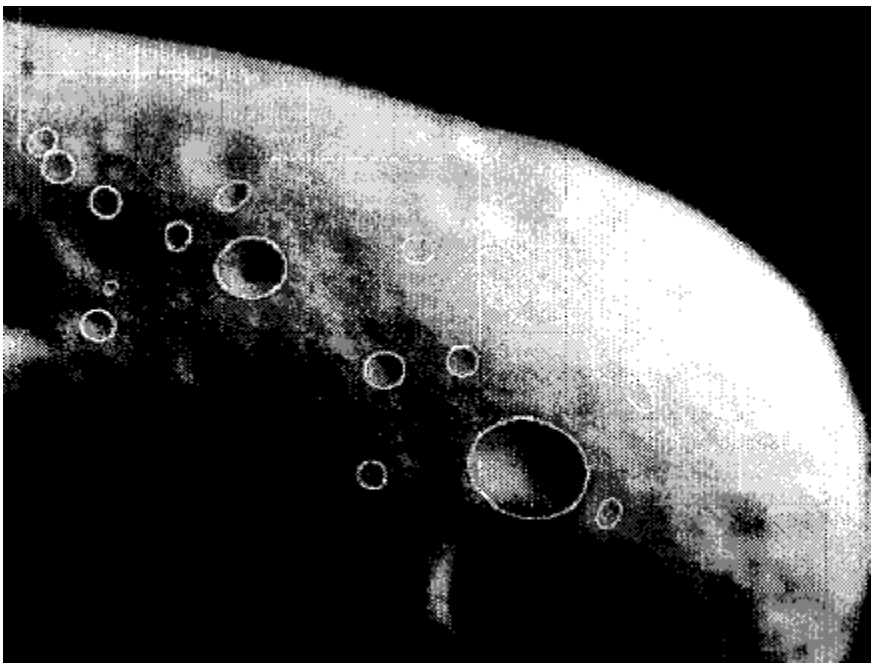

Figure 3 Near landmark navigation at Eros asteroid using craters detection

Successively with the Dawn spacecraft launched in September 2007, that reached Vesta in 2011 it was possible to apply optical navigation. A key aspect of optical navigation at Dawn is the extensive use of landmark navigation during most of mission phases. This technique in addition to real-time navigation operations support can be used also for determination of key physical characteristics of Vesta, such asteroid pole and shape and assist mission design and science operations. In this mission a new methodology was used that consisted in the use of limb scans, and landmarks, defined not by craters or particular features but by centers of small digital terrain and albedo models (landmark maps) that extends over a fraction of the surface (Mastrodemos, 2011).

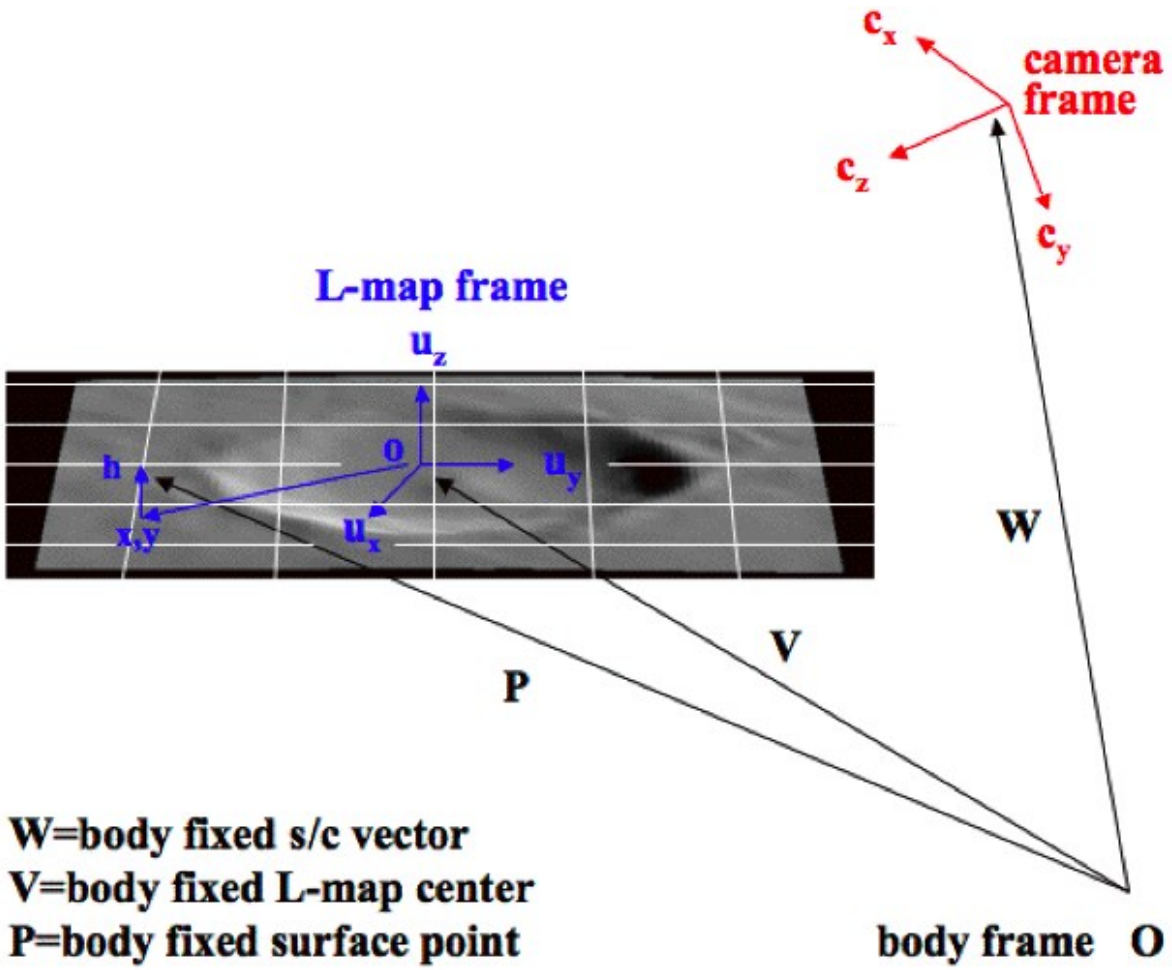

Figure 4 Landmark map geometry

Similarly ESA has an optical navigation strategy for Rosetta encounter with comet 67P/Churyymov-Gerasimenko. This is a mission that will exploit landmark navigation together with classical optical star-based navigation for Lutetia and Steins Asteroids fly-by thanks to its 4 cameras payload; 2 navigation cameras and 2 Osiris cameras(WAC & NAC) (Munoz, 2012).

2.3.2 New Horizons and OSIRIS-Rex Optical Navigation

KinetX Aerospace is currently developing an OpNav software to ensure support to New Horizons to the Pluto system and OSIRIS-Rex to asteroid 1999 RQ_{36}. This software uses spacecraft imaging to determine the spacecraft trajectory and targets ephemerides. Precise target-relative navigation required for critical mission events at extreme distances from Earth, exploit optical navigation for cross line-of-sight information to de-correlate estimates of spacecraft state from the target body ephemeris. In particular there are two basic optical informations, the star-based and the landmark-based ones. Landmarks navigation is particularly suited for touch-and-go (Jackman, 2013).

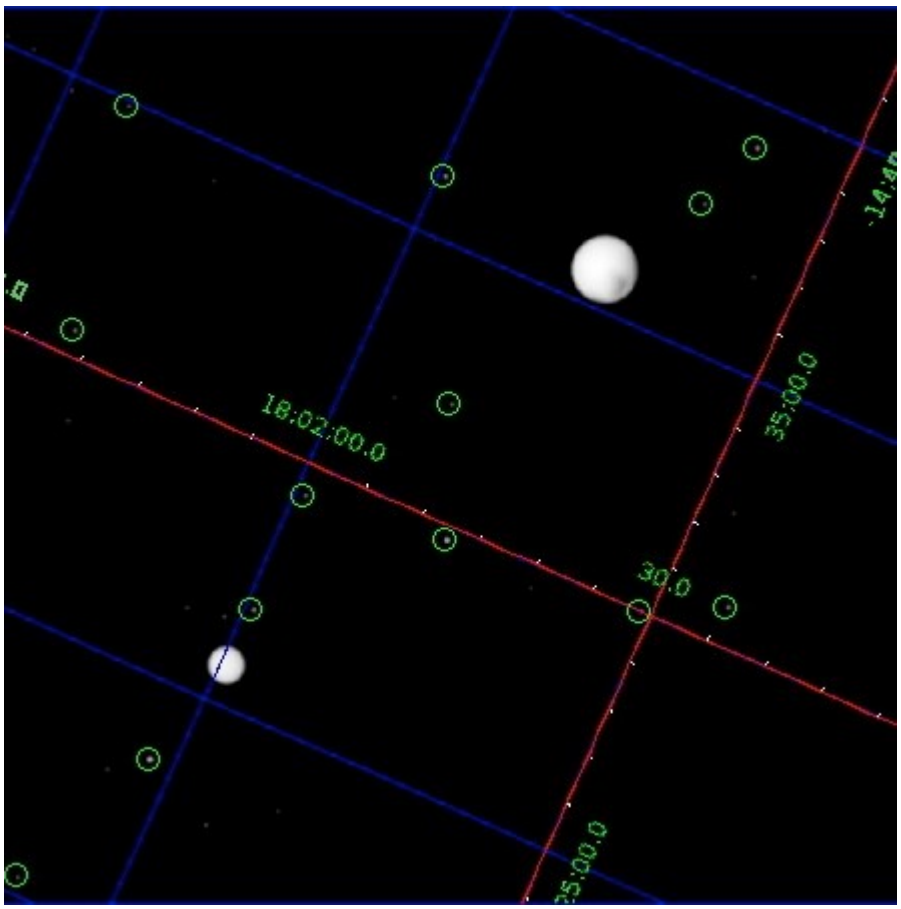

Figure 5 Star-based OpNav with simulated Pluto and Charon .

3 Pattern Matching

3.1 Features selection

A comparison of two images requires the extraction of a significant set of features from both.
A basic rule for the application of one typology of feature with respect to another is that if the acquisitions are close in time, corner point features may be sufficient, while if acquisitions are distant in time, different feature descriptors, i.e. features based on transformed spaces will be best suited, having properties of scale, deformation and illumination invariance.
Feature types:

- Geometrical, e.g. craters (features extracted from an image)
- Statistical, uses the entire image in a geometrical way.
- Photometric, less dependent by the surface geometry but by the photometric characteristics
- Local, e.g. areas with high photometric gradients, only sliding windows or regions of a frame are analyzed (ambiguity problems solved with global features).
- Global

Some example of features based on transformed spaces are:

- SLAM; pose estimation and map buildings of the environment.
- SIFT; appearance based approach, it's an image recognition method that extract scale, rotation, viewpoint invariant feature points reaching sub-pixel accuracies.
- SURF; image tracking partially inspired by SIFT but several times faster.

Historically the first tracked features were geometrical, i.e. Craters on asteroid Eros, mapped by NEAR Shoemaker (Owen, 2001).

3.2 Features Tracking

Once a sufficient number of features is extracted, it is necessary to track the displacement of the pixels between the two images.
The more the information present in the images, the higher the probability of success of feature extraction and tracking. The most informative features are the one that characterize not only the observed pixel but the one that characterize a window of a certain dimension around the pixel. In general, uniqueness of the feature is higher if the window dimension is higher, but sensitivity to shadowing, occlusion and other factors works in the opposite way. Only a trade-off between the two phenomena permit to select the optimal feature window dimension.
Various Methods for features tracking are

- Correlation-like method
- Fourier methods (frequency dependent noise, low computational capabilities)
- Mutual information methods (for multimodal registration)

3.3 Corner points extraction

Corner points, based, as the name implies, on points of high photometric contrast, are fast to extract and track. They can be extracted easily from noiseless, sharp images. Though, by their nature, they have little characteristics of uniqueness and, consequently, also a low information tent. However, images that have a high number of corner points, define a spatial arrangement that increases the uniqueness. Moreover, these features are calculated on very small patches (local feature), therefore they are extremely robust to occlusions.
The selected algorithm for corner detection is the one provided by Lucas Kanade and Tomasi (KLT detector), because is a very low computational demanding methodology providing the possibility for a real-time on-board implementation (Tomasi, 1991).

The KLT detector compares two frames, given that they share a fraction of the framed scenario. In particular, higher photometric gradient, are searched thorough the image, in both horizontal and vertical directions), that correspond to two borders that cross.
Mathematically this search is done computing for each point of the image, the two eigenvalues of the covariance matrix of the gradients.

$$\boldsymbol{C}(\boldsymbol{s},\boldsymbol{l}) = \begin{bmatrix} \boldsymbol{g}_x^2(\boldsymbol{s},\boldsymbol{l}) & \boldsymbol{g}_x(\boldsymbol{s},\boldsymbol{l})\boldsymbol{g}_y(\boldsymbol{s},\boldsymbol{l}) \\ \boldsymbol{g}_x(\boldsymbol{s},\boldsymbol{l})\boldsymbol{g}_y(\boldsymbol{s},\boldsymbol{l}) & \boldsymbol{g}_y^2(\boldsymbol{s},\boldsymbol{l}) \end{bmatrix} \quad (20)$$

The window dimension and the Threshold value for the smaller eigenvalue is selected. Afterward the list of CP is sorted and passed to the tracking algorithm.
When sampling a body from two different pose (attitude and position), there is a mathematical transformation that links the two view. Basic transformations types applicable to an image are:

- Rotation
- Translation
- Reflection
- Subsampling
- Interpolation
- Zooming
- Rectification
- Scale
- Shear
- Affine
- Perspective
- Projective
- Warping

Corner point features are translation invariant and , for little rotation, also rotation invariants.
First tests were conducted with Matlab® Built-in algorithms with sub pixel lever performances. Whenever this level is not achieved because of degraded illumination conditions, more sophisticated methodologies may be considered.
Examples of two synthetic images of the same landscape, generated by DEIS, with different illumination conditions

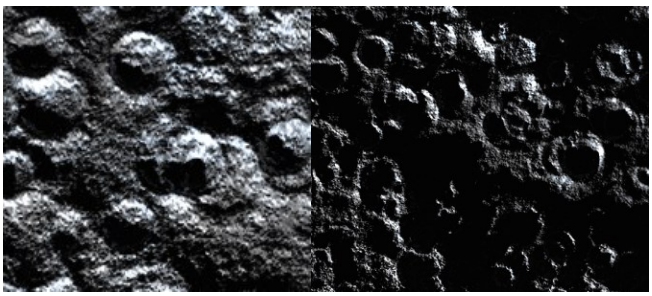

Figure 6 Sample synthetic image of Mercury surface at different illumination conditions 512x512p

The search for corner points is feasible at different scale levels, because there is the same information content regardless of the image resolution. The following set of images was extracted by a single image, where different illumination conditions are also present. Is evinced that corner points can be found in each of those conditions, varying the threshold and window dimensions accordingly.

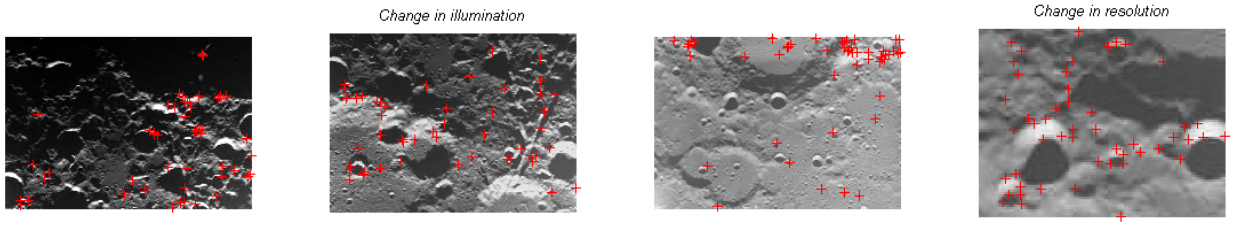

Figure 7 Corner point extraction at different scale and illumination conditions

3.4 KLT tracking

A pair of set of features, one for each of the two images to be tracked is then labeled uniquely by means of a matching algorithm. An high number of features Is needed to obtain a significative sample of displacement vectors on which to apply a statistical methodology.
The optimal KLT tracker for corner point features has been defined in (Shi, 1994).
Given a couple of images I and J, the algorithm goal is to minimize the residual difference between the two windows W, that define the CP in each image. This minimization is done differencing the difference functional

$$\varepsilon(d_x, d_y) = \iint_W [J(x,y) - I(x + d_x, y + d_y)]^2 dxdy \quad (21)$$

by searching for the d vector that minimizes this error.
At the end of the iteration process, the functional is checked with the resultant d vector by computing

$$E(x,y) = \sum_W J(x,y) - I(x + d_x, y + d_y) \quad (22)$$

KLT is limited by little translations, one solution to avoid this problem is to apply the methodology in a pyramidal approach.

The last problem is that some of the correspondences obtained may be wrong. An iterative procedure can automatically remove the outliers (wrong correspondences), for example using a Random Sample Consensus algorithm (RANSAC).

A pattern matching result of displaced syntetic Mercury images using a Matlab® algorithm is showed in the following image.

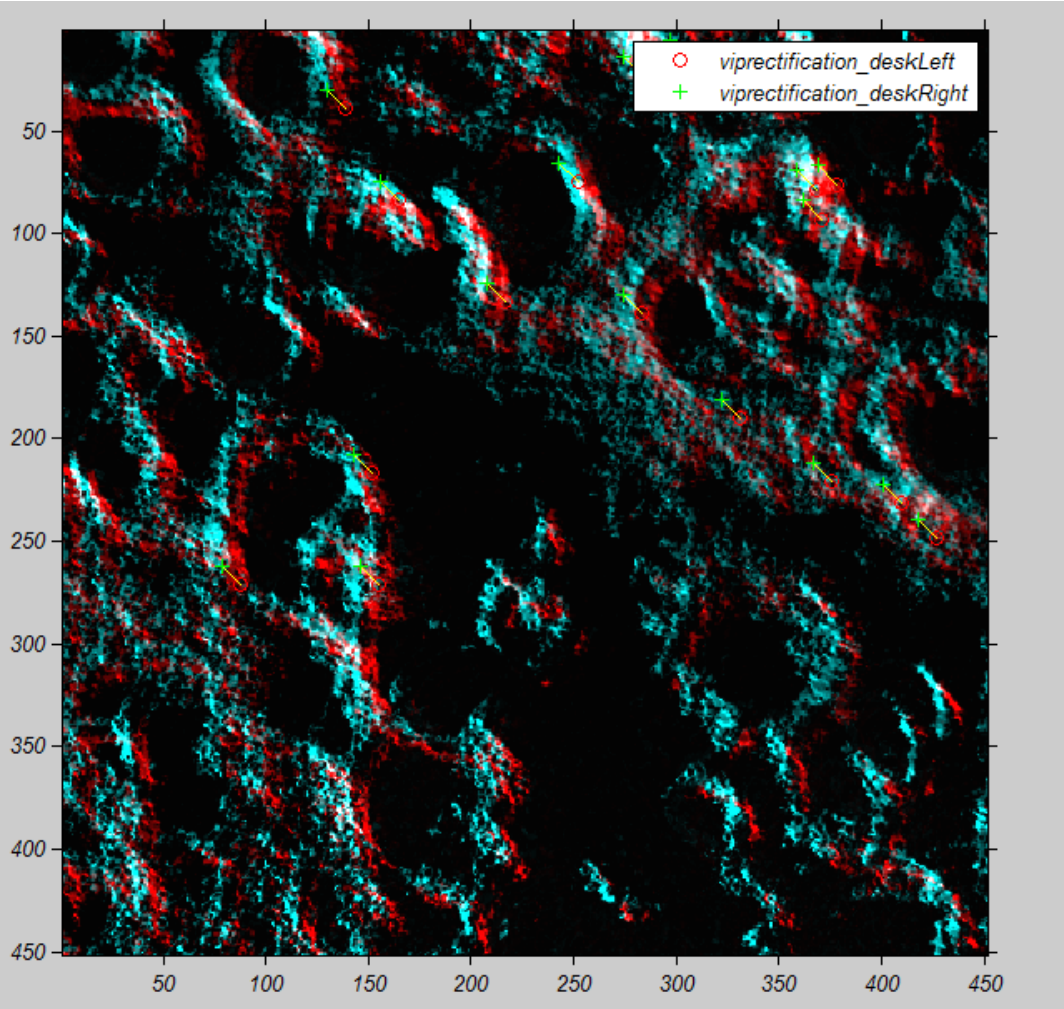

Figure 8 Pattern matching result on synthetic Mercury images

After the matching is completed, a one-to-one relation between CP in the first and second image is given.

4 Crossover Optical observables alternatives

A brief review of possible definitions of optical observables from pair of images acquired by an on-board camera orbiting around a planet or a moon, is described, then, the formulation selected for the present study is developed for an implementation in an orbit determination software.

4.1 Homographic projection

Is a concept originated from computer vision, in particular from the homographic projection of stereoscopic vision (Bevilacqua, 2010).
In this formulation for spacecraft applications with only one camera, the boresight is not the distance between two cameras observing the same area but between two different spacecraft positions through the orbit with an area of field of view in common between the two times of acquisition.

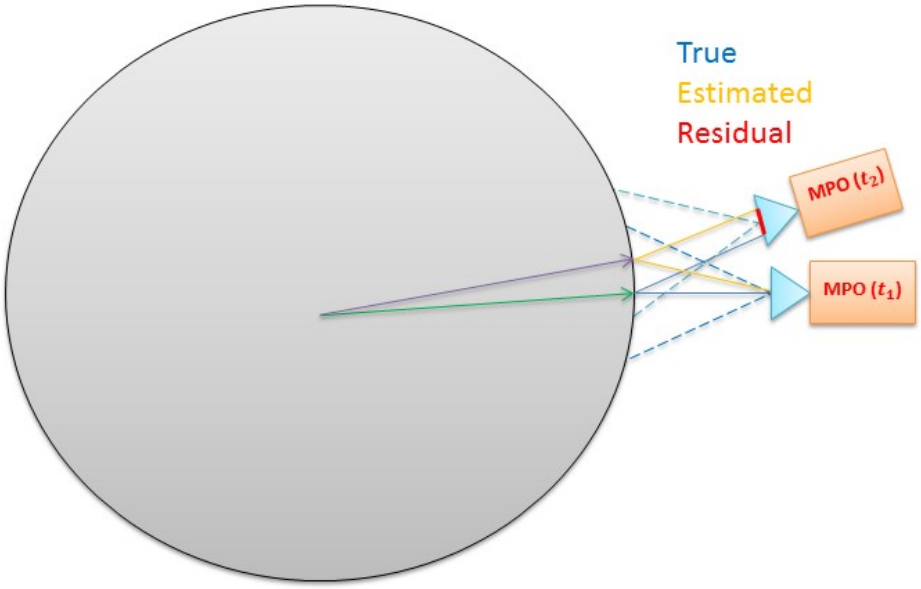

Figure 9 Homographic projection scheme

The equations form is based on two orthographic projections used in a sequential chain, where the camera plane pixel coordinates of a reference images are projected into the camera plane of an overlapped image. The residuals are the differences between the computed camera pixel coordinates and the observed camera pixel coordinates in the overlapped image.

$$z(t_2) = Hz(t_1) + C(X(t_1) - X(t_2)) \quad (23)$$

$$\Delta z = z_{comp}(t_2) - z_{obs}(t_2) \quad (24)$$

This methodology permits to have measurement units equal to the one from Cassini OpNAV.

Landmarks indicated in the figure are a subproduct of the intersection with an approximated target body as an ellipsoid of the rays coming from the camera. Landmarks are not necessarily estimated in this procedure.

4.2 Landmark misregistration

This alternative methodology is originated from the MORE Rotation Experiment, where each landmark (or tipepoint) can be indicated with a body fixed (TERF coordinates) position generated from the orthographic projection of the image points onto the surface of the target body.

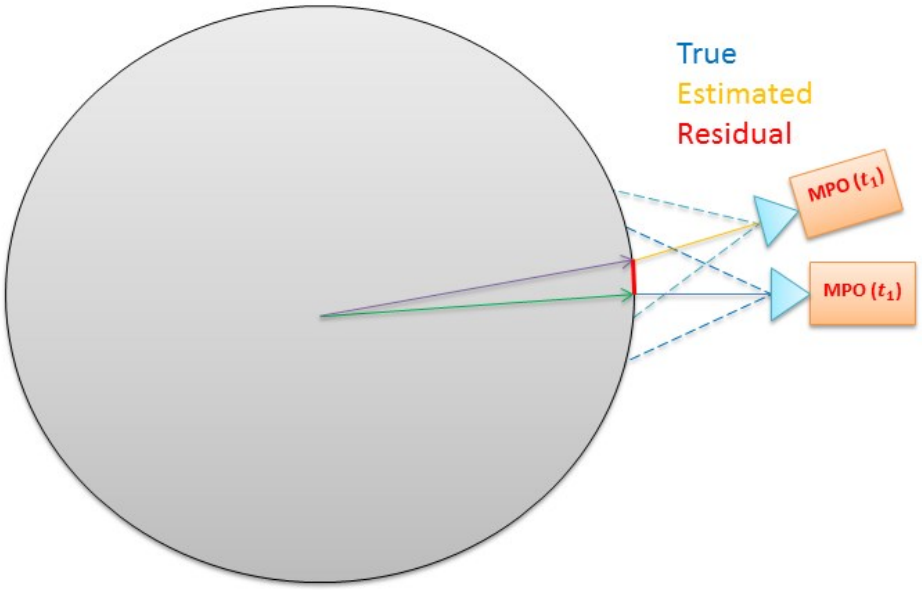

Figure 10 Landmark misregistration scheme

The difference of the two landmarks position misregistration error is the residual to be minimized.

$$\Delta\rho = R_2 - R_1 = M(t_2)r_2 - M(t_1)r_1 \quad (25)$$

where r_1 and r_2 are the landmark inertial position on the surface of the planet, computed by a ray intersection of the camera features. M is the rotation matrix from an inertial to a bodyfixed planetary reference frame and $\Delta\rho$ is the misregistration that for a perfect knowledge of models and state attitude and position, should be zero(Meriggiola, 2012).

4.3 Landmarks estimation

A ficticous tie-point or a series of geometric landmarks on the surface of the target body representing a crater, are selected from reference images and included in the estimation. From a first pair of images the body-fixed position of the landmark is computed thanks to pose estimation, then as soon as more images of the same area arrives, the better this vector can be estimated, constraining at the same time the orbit for the next navigation solutions.
This methodology was already applied for Near Spacecraft at Eros Asteroid, where nearly 1000 landmarks were estimated (Owen, 2001).

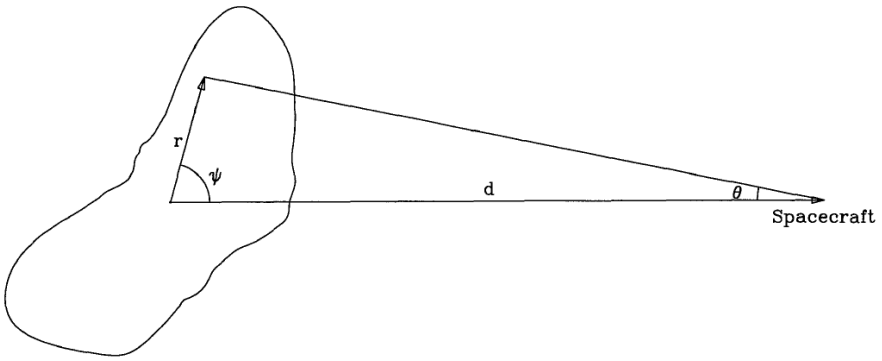

Figure 11 Optical navigation scheme at Eros

4.4 Definition and construction of the optical observables from pair of images

The method developed in this thesis is the one that take inspiration from stereoscopic vision. This methodology is built in similarity to the OpNAV used by Cassini during survey of satellites positions with respect to a background of stars. As in the OpNAV the Optical Observables here defined are measured in pixel units and instead of observing a geometrical landmark, it is observed a ficticous center defined as the focal axis build up from the reference image of the pair and the pose of the camera at the reference time. This is also the reason why, the estimation is not augmented by landmarks positions. It is intended to define a constraint between two orbits for an easy to process information for real-time navigation. Moreover the images may be successively reprocessed in a global estimation filter with a landmark-like formulation, to improve scientific knowledge of the target, by reconstructing its topography, rotational state and gravity field.

The starting point is to have a couple of images that have a superimposition of the shooted area.
An optimized pattern matching process is then executed selecting the correct one as a function of illumination condition and pose variations between the pair, to maintain generality, although, in this research only Corner Points were studied, because of the particular condition of a nadir pointing orbiter with high resolution images that is MPO.
If the pattern matching do not fail, a set of displacement vectors of each feature is given, that can be reduced to the displacement vector of the center of the first image on the second image mainly due to spacecraft change of pose.
This information is sufficient to define a bidimensional optical observable that contains this displacement as sample and line (s,l) in the second image.

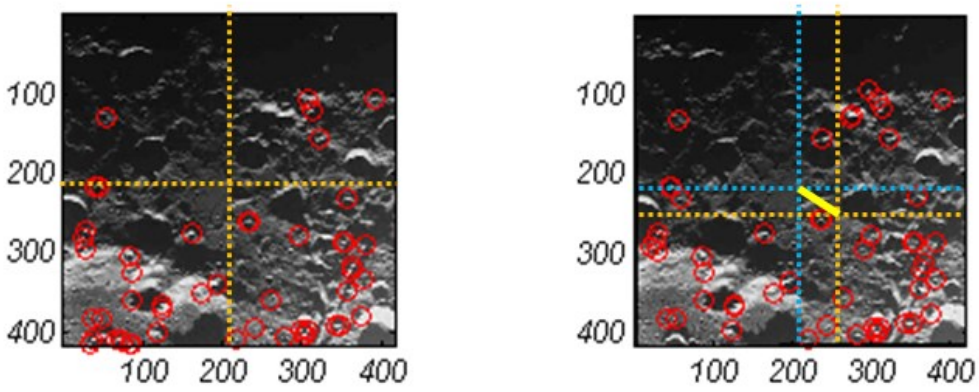

Figure 12 Reference image and displacement vector represented on the secondary image

The next step is the mathematical formulation of this bidimensional coordinate vector with respect to the first image and the estimation parameters. It is briefly reviewed the structure of the formulation that is developed in depth in another chapter of the Thesis.
The model used for the camera is the pinhole model, that is sufficient for cameras as HRIC and ISS NAC, that describes with an orthographic projection the relation between the image plane of the camera and 3D points in a reference frame centered in the focal center of the camera.

$$z\left(t\right) = K\mathbb{T}_C^I\left(\mathrm{t}\right)\left[P_I\left(t-\tau\right) - X_I'\left(t\right)\right] \quad (26)$$

in this formulation z(t) represent the coordinates in the reference system of the CCD sensor, therefore in adimensional pixels units of the 3D surface point represented by the target computed by the difference between the camera position vector $X_I'\left(t\right)$ with respect to a reference coordinate system, and the observed point $P_I\left(t-\tau\right)$definet with respect to the same coordinate system.
The effect of light time propagation Is considered by adding a light time delay τ . K represent the intrinsic matrix, dependent only on the characteristics of the camera as the focal length and the pixel dimension in units of length. $\mathbb{T}_C^I\left(\mathrm{t}\right)$ is the rotation matrix that convert the observed point to an inertial reference frame to a camera reference frame.
If an overlap is present in the two images, the observed point can be described with two orthographic relations at the two shutter times of the two images t_A e t_B. Afterward one equation can be can be substituted in the other obtaining a formulation in which pixels coordinates in the reference are related with pixels in the secondary image

$$z_C(t_B) = Hz\left(t_A\right) + K\mathbb{T}_C^I(t_B)X_I'(t_A) - X_I'\left(t_B\right)] \quad (27)$$

H is a linear Homography taking into account the relative rotation between the two images while the nonlinear term takes into account the displacement due to spacecraft different position at the two different sample times.

$$H = K\mathbb{T}_C^I(t_B)\mathbb{T}_C^I(t_A)^{-1}\mathrm{K}^{-1} \quad (28)$$

An orbit determination filter will requires residuals and partial derivatives.
The residuals are easily computed subtracting from the displacement computed by the PM process, the observed observable, the displacement computed by the procedure aforementioned, the computed observable.

$$r(t_B) = z_O(t_B) - z_C(t_B) \quad (29)$$

Partial derivatives are obtained from computed observables mathematical expression differencing with respect to estimation parameters. The formulation will take the following shape:

$$\frac{\partial z}{\partial q} = \frac{\partial z}{\partial s_B}\frac{\partial s_B}{\partial q} + \frac{\partial z}{\partial s_A}\frac{\partial s_A}{\partial q} + \frac{\partial z}{\partial q} \quad (30)$$

Where q is the set of parameters considered in the estimation, s_A is the state of the spacecraft at shutter t_A and similarly s_B refers to the state at the shutter time t_B.

5 Missions Overview

In this chapter Cassini and BepiColombo missions are described. For this study Cassini was an important reference mission because it was well known and comprised the use of OpNav. The other mission is the one that serve well as a simulation test-bed of the proposed optical observables. Both the missions carry an imaging experiment described with detailed literature. Moreover Cassini NAC Camera is a consolidated and well tested instrument, with almost 17 years of operations, and its calibration procedures and problems are well known and solved. Although simulations are devoted primarily to obtain possible applicable results to MPO, it is necessary also to refer to legacy missions to have the strongest confidence in the values and various aspects of what concern navigation and optical systems.

5.1 Cassini Probe

The Cassini spacecraft was launched on October 15, 1997, with a payload of twelve scientific instruments for the exploration of the Saturnian planetary system. Since reaching its destination on June 30, 2004, Cassini and its companion mission to Titan, Huygens, have successfully acquired and transmitted back to Earth a wealth of informations, allowing for an unprecedented look at some of the solar system's most varied, dynamic, and once-mysterious landscapes.
This mission carry on-board an Imaging Science Subsystem (ISS) that is the Cassini's primary optical navigation tool on board. The ISS consists of two separate cameras, the Narrow-Angle Camera (NAC) and Wide-Angle Camera (WAC), which are boresight-aligned and have fields-of-view of 0.35 degrees and 3.5 degrees, respectively. The cameras have been designed for maximum flexibility: their photometric and spectral sensitivity, linearity and dynamic range, optical resolving power, and wide variety of compression and other data collection modes can accommodate a vast array of targets and imaging situations. In terms of real-world resolving capabilities, the NAC can achieve pixel scales as small as a few tens of meters on targeted satellites.
Cassini Spacecraft Frame is oriented by means of reaction wheels, providing an highly stable pointing for the ISS cameras. For example, in star images during the cruise phase a typical pointing variation of about 18 μrad (3 NAC pixels) over the course of 50 minutes.
During flight the determination of the inertial attitude of Cassini is done thanks to analysis of the position of the stars measured by a star tracker (SRU). The accuracy of this system for the absolute pointing is of 60 μrad. The mounting of the SRU in the $+X_{S/C}$direction provides this absolute accuracy for the NAC camera only in the line direction $-X_{S/C}$, while in the sample direction$-Z_{S/C}$ the accuracy strongly depends on the distribution of stars in the SRU field of view, degrading the sample direction to about 900 μrad.

5.1.1 ISS NAC Camera

The ISS Narrow-Angle Camera (NAC) is an *f*/10.5 reflecting telescope with an image scale of ~6 μrad/pixel, a 0.35 x 0.35 degree field of view, and a spectral sensitivity from 200-1100nm, which is spanned by 24 filters, arranged in two filter wheels of 12 filters each. The CCD detector is a 1024 x 1024 pixel wide, with pixels of 12μm .

Figure 13 ISS Nac Camera (Credit NASA)

Geometric fidelity in this camera is very good across the field of view , due to its optical design and narrow viewing angle. Ground-based and in-flight measurements indicate geometric distortion of less than a pixel in the corners of the NAC field of view.
Point spread function measurements were considered, also with dark current measurements planning with closed shutter .
A command for on-board pixel summation for increasing signal-to-noise or decreasing data volume is also present (Knowles, 2012).

5.2 BepiColombo MPO Orbiter

BepiColombo is an interdisciplinary mission to Mercury scheduled for launch in 2015, arriving at Mercury in 2021. It is a joint mission between ESA and JAXA consisting of 2 complementary spacecraft: MPO and MMO.

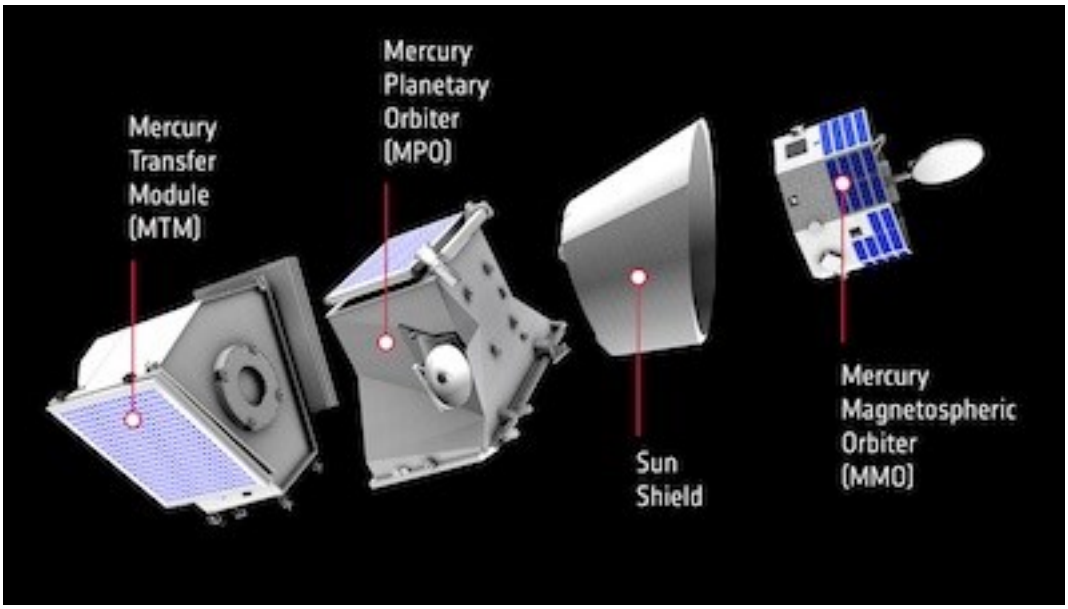

Figure 14 BepiColombo cruise configuration

MMO is the Magnetospheric Orbiter of JAXA, while MPO (Mercury Planetary Orbiter) is a Mercury polar orbiter optimized for study of the planet, with an initial orbit of 400 km at periherm and 1500 km at apoherm, with a period of about 2.3 hours and a nadir pointing attitude. The 6 years cruise will be exploited for a test of Einstein's theory of general relativity.

After the capture into the Mercury sphere of influence, MPO will be inserted into a polar orbit of 400 km of altitude at periherm and 1500 km of altitude at apoherm.
The mission duration is 1 year, with eventually one year of extension. The orbit itself is not maintained.

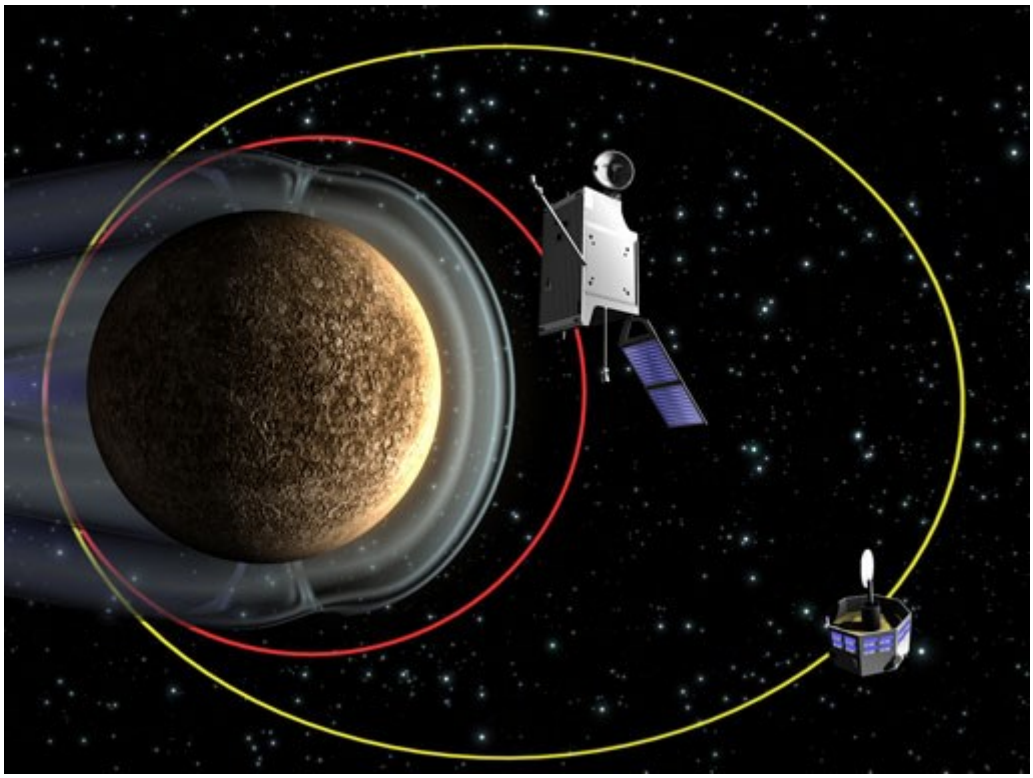

Figure 15 MPO and MMO orbit

The main instruments onboard the MPO spacecraft are the laser altimeter BELA, the Italian spring Accelerometer ISA, the magnetometer MERMAG, the radio-science experiment MORE, the spectrometers and imagers SIMBIO-SYS.

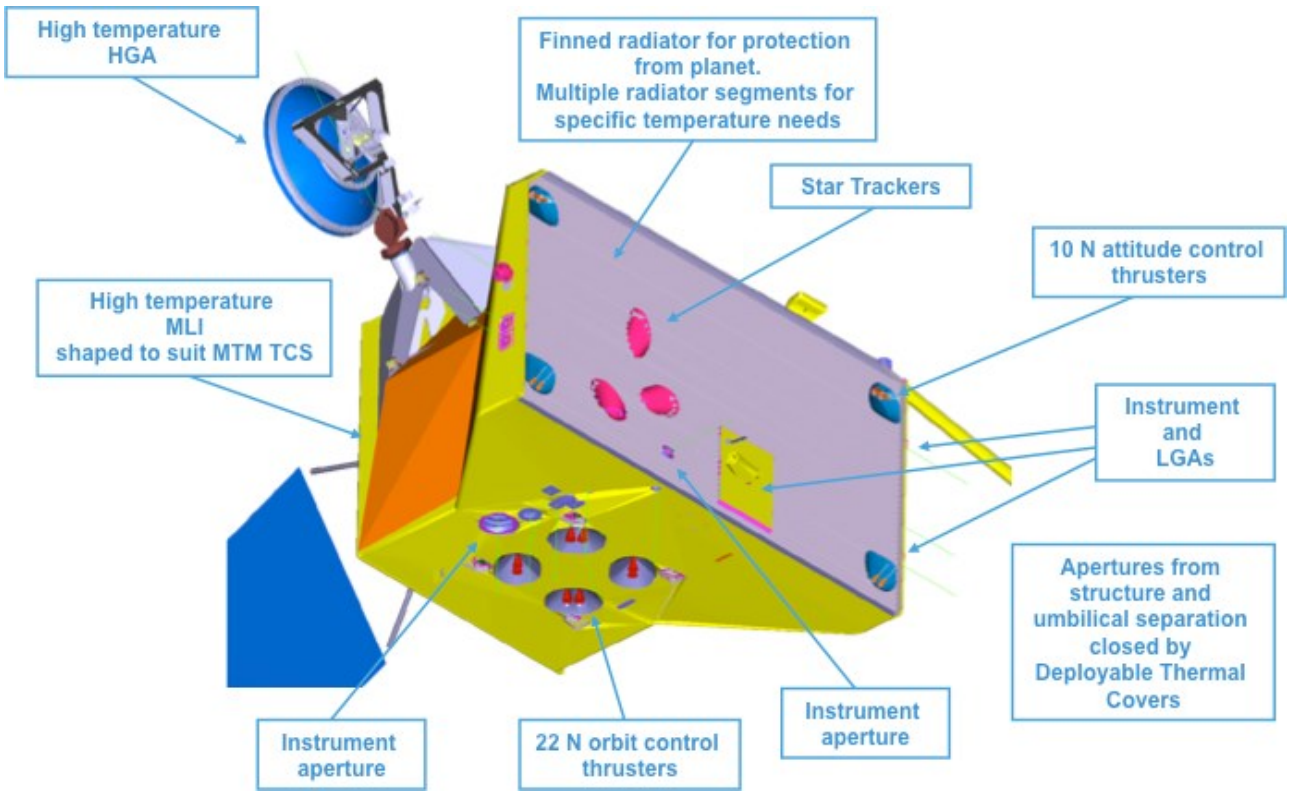

Figure 16 MPO main systems and shape

An important constrain for this mission is due to the high temperatures impacting on MPO at perihelion and aphelion. Thermal limitations of the solar arrays requires to reduce the angle between them and the sun direction, reducing the power available for payload operations and Ka-Band transmitter operations.
Another constraint to the mission is the necessity to plan a wheel off-loading twice a day (24 hours) with attitude control thrusters, because of the nadir pointing attitude controlled by a 3-axis stabilized system.
The mass of the spacecraft at injection will be of 1075 kg and the payload power of 100 to 150 Watt. The communication system is at X/KA band with a 1 meter high-gain steerable antenna.

5.2.1 HRIC

The High resolution Imaging Channel (HRIC) of the instrument SIMBIO-SYS is a state-of-the-art instrument that will allow to observe Mercury surface at an unprecedented resolution, and also, selected regions of Mercury will be of paramount importance in support of experiments aiming to the identification of Mercury orientation parameters (Palli, 2012)

HRIC is an *f*/8 modified catadioptric Ritchey-Chretien telescope with an image scale of ~12.5 μrad/pixel, a 1.47 x 1.47 degree field of view, and a spectral sensitivity of 400-900nm. The focal length is of 800 mm and is equipped with a dedicated refractive camera, in order to correct the field of view covered by a detector of 2048 x 2048 pixels and a pixel size of 10 μm. The expected pixel scale at periherm is of 5m/pixel (400km from the surface) (Zusi, 2009).

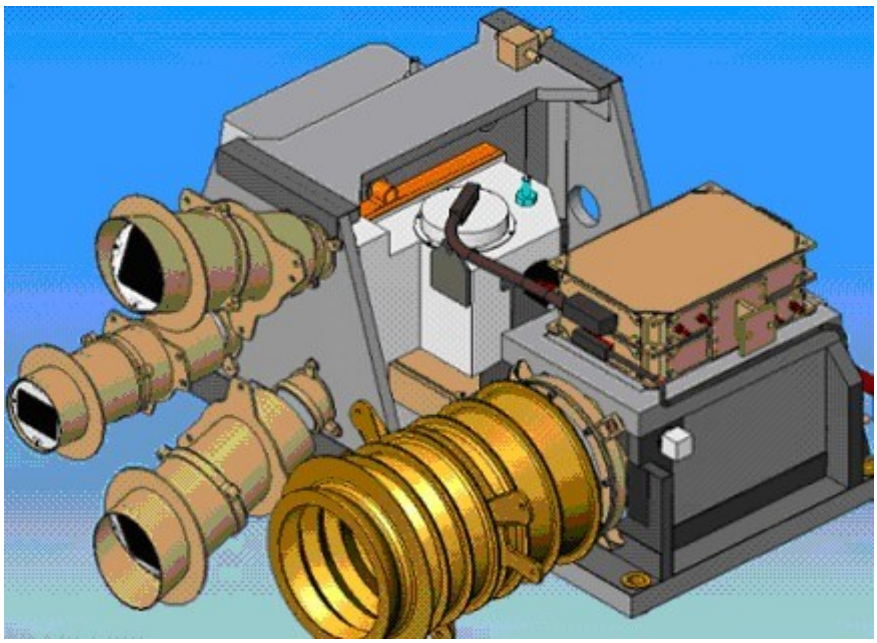

Figure 17 SIMBIO-SYS HRIC Large aperture on the right. Credits INAF

6 Operative considerations

6.1 Calibration of a Spacecraft Imaging Instrument

Although image calibration is a fundamental phase of the preprocessing of an image it will be only briefly described here. It is considered necessary for the reconstruction of the camera deformation, for the modeling of the point spread function and so on and, in general for scientific use of raw images. The calibration of the camera is done in two different phases of the mission, on ground with an instrument test-bed during its validation and in-flight.
The main goal of a calibration is to associate the data number (DN) values recorded at each pixel in an image to actual physical units of incident intensity, thus having a quantitative measurement for science operations.
Equations relating DN to intensity can be found in every basic text of image preprocessing.
For Cassini a calibration software already exist and is called CISSCAL (Knowles, 2012). This software provides the basic functions for the calibration of a raw image and process the image to correct the following contributes:

- LUT conversion
- Bitweight correction
- Bias subtraction of the DN zero-exposure level of the CCD chip.
- 2-Hz noise removal (a particular coherent noise found in Cassini ISS images)
- Dark current and residual bulk image subtraction
- A-B pixel pairs corrections due to artifacts created by anti-blooming
- Linearization of CCD response
- Flatfield removal
- Conversion from DN to flux
- Application of correction factors
- Application of geometric corrections (e.g. pin-cushion distortion)

A similar software for the conversion of MPO raw images to calibrated intensity images it is expected. This research considers calibration given, therefore when talking about images or observables, it will be always about an already-calibrated one.

6.2 Images acquisition planning

Together with the research in term of complementarity between radiometric and optical measurements is necessary to understand if it is possible to schedule optical navigation campaigns and how. Three main strategies are considered:

- Sequential schedule
- Referenced schedule
- Sparse schedule

The sequential schedule can be designed for a polar orbiter as MPO. Thanks to this orbital geometry and accounting for the natural rotation of Mercury, the field of view of the camera at high latitude, swap the surface of the Planet, generating overlap areas, which may be exploited for producing optical observables periodically. These images may be acquired at both poles or it can be chosen to select only one pole.

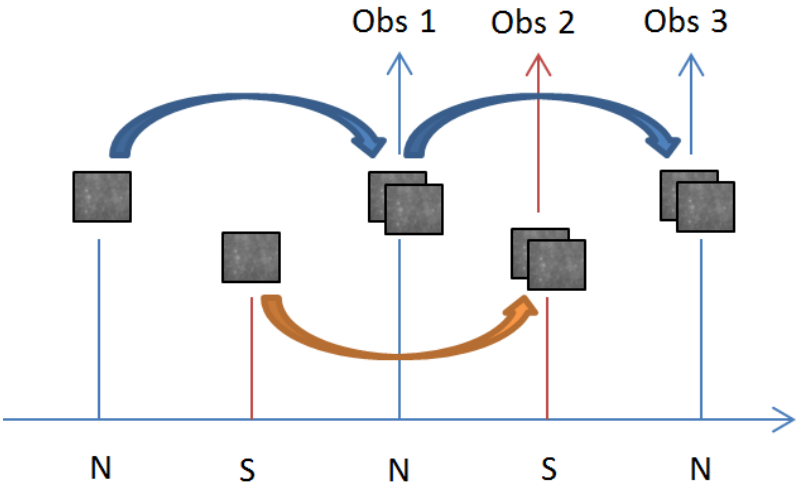

Figure 18 Images Sequential planning

For MPO, one day sampling time with sufficient superposition of the images is possible, allowing also to have a reduced change in illumination conditions.

A reference schedule is similar to the sequential one but more constrained in terms of overlap chances, because the planet rotates. The scheme is to have a reference image from which all other images are referred to. The sampling time may be very long, because it is necessary to wait until another condition of overlapping happens again, or it is necessary to schedule off-nadir pointing schemes to have short time coverage. this methodology may be also used for a sequential strategy in which a relaxed sample time may be requested to reduce the data volume.

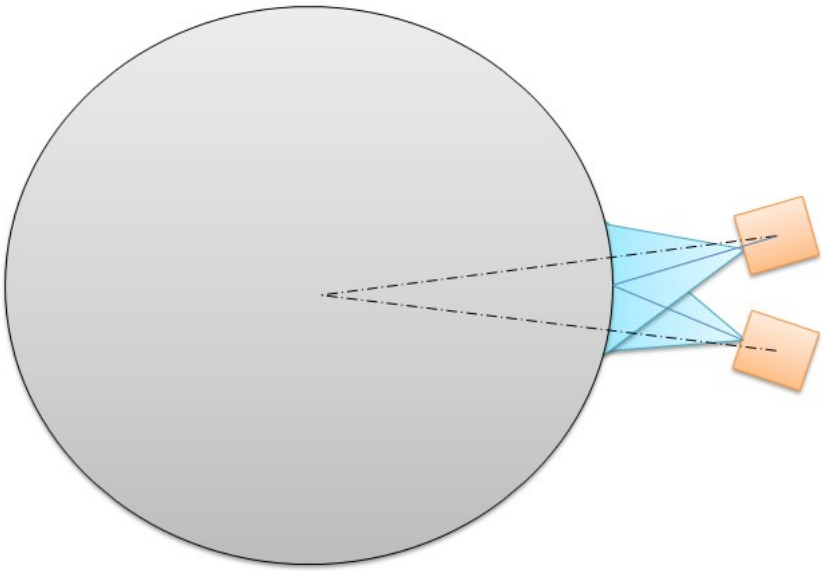

Figure 19 Off-Nadir Overlap Strategy

The number of observables, $C_{n,2}$, produced by n acquired overlapped images can be computed with permutations

$$C_{n,2} = \frac{D_{n,2}}{P_k} = \frac{n!}{(n-2)!2!} = \binom{n}{2} \quad (31)$$

This methodology may be applied to a sequential planning after a full translation of 360° on the

planet pole has been done, giving also the possibility of a registration of old observables with new data.

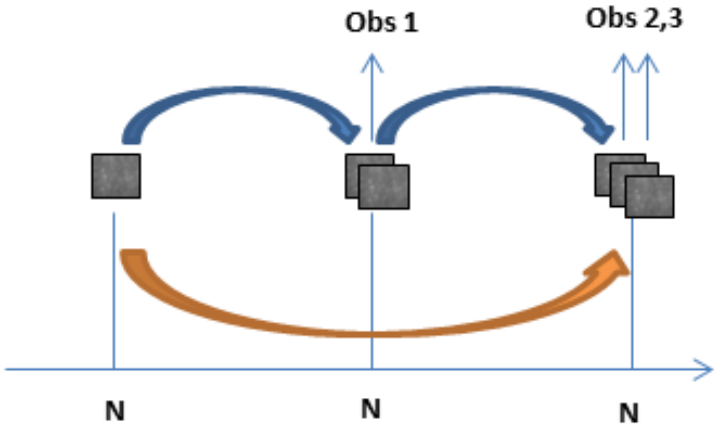

Figure 20 Image Referenced planning

At longer timespans it is possible to produce sparse images at various latitudes, this is the scheme adopted for the MORE Rotation Experiment in which the libration amplitudes were to be estimated from. It is in general a method more suited for science purposes than navigation because it depends also to long period effects.

6.3 Images acquisition sources

Possible sources of overlapped images can be obtained from

- ad hoc observation campaign; requires a trade off with the imaging Team if the spacecraft carries only a science camera and no navigation cameras. It afflicts in a negative way the data volume for science objectives if no particular action is taken.
- Overlapped areas from a Mosaicing campaign; in this case, there is no impact on the data volume, there is less flexibility for the navigation team, to obtain optical measurements at the requested time. An optimized planning of the mosaicking in a trade-off between navigation and science requirements, may result in a more homogeneous distribution of optical measurements through time.

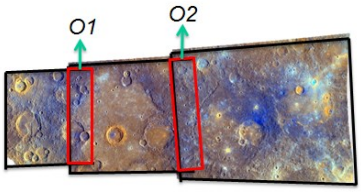

Figure 21 Source of optical overlap observables from planet mosaiking procedure

- overlapped areas from SAR swaths; radar images can be also considered (eg. Titan multiple flyby swats) also if the resolution is lower with respect to optical images. Permits to use the methodology also to broader scenarios,as for cloudy moons/planets like Titan. A resolution of 350m @950km altitude is achievable for a SAR system. Landmarks mismatch is the dominant source of error (1pixel accuracy) (Stiles, 2008).

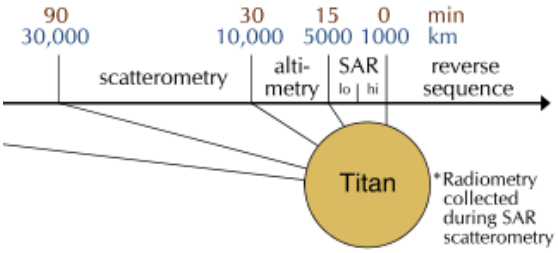

Figure 22 SAR range of use

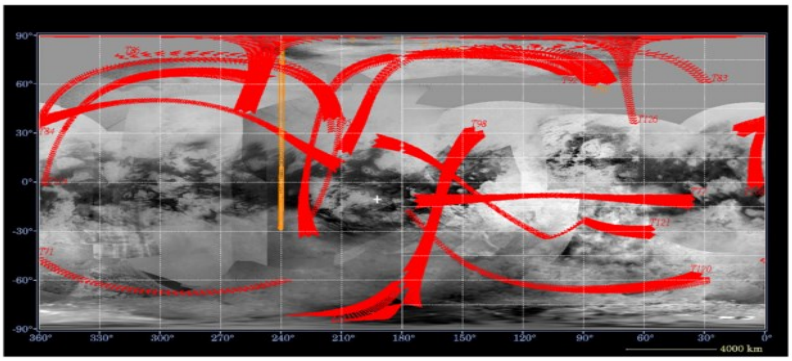

Figure 3-4. Titan SAR coverage from the Solstice (XXM) mission. The swaths are shown on an ISS basemap.

Figure 23 Titan SAR Swath Crossover

6.4 Crossover finding methodologies

A possible method is proposed in (Palli, 2012), useful for sparse images with apriori defined constraints in terms of illumination variation conditions and surface position. It considers the ground-track of the camera view when it's smaller, then calculate the angle in the ellipsoid to have a grid sufficiently small to catch that view. The term used is "view belonging to a node". It can be showed that each node, i.e. the resolution of the planet spatial grid, using the scenario of MPO at the higher resolution (periherm) has to be lower than 0.24° with a number of surface faces of 1.2e6.
For sequential polar images, a simpler and quicker algorithm was implemented for the present study. The algorithm only requires an input latitude and a constraint in overlap dimensions between two sequential images, then it compute the pair of shutter times in ET time to be used for the computation of the optical observables.

6.5 Overlap constraint

There is a limitation due to planet rotation that gives rise to a maximum sample time between two images.
The altitude of the S/C at a certain true anomaly is expressed by:

$$h(\vartheta) = \frac{a(1-e^2)}{1+ecos(\vartheta)} - r_{\varnothing} \quad (32)$$

With an MPO polar orbiter of 400x1508 km with an equatorial semi major axis in the planet body-fixed reference frame, the altitude at an elevation of 88° with respect to the planet equator is $h(88°) = 845\ km$.

Then the ground resolution is

$$res_{GT} = h\frac{dx}{f} \quad (33)$$

Where dx is the pixel size and f is the focal length.
The ground track resolution is therefore for the HRIC camera, 10.6 m/pixel at 845 km of altitude.
For example a ground track resolution of 9m at a latitude of 80° the limit on sample time for a requested overlap of 10% is (but as low as a 5% is acceptable for ill-conditions in PM):

$$T < \frac{l_{cam} res_{GT} \eta}{\omega_p r_p \cos(\lambda)} = 3\ Orbits(6.9\ h)$$

where

$$l_{cam} = 2048\ pixel$$
$$res_{GT} = 9m/pixel$$
$$\eta = 0.90$$

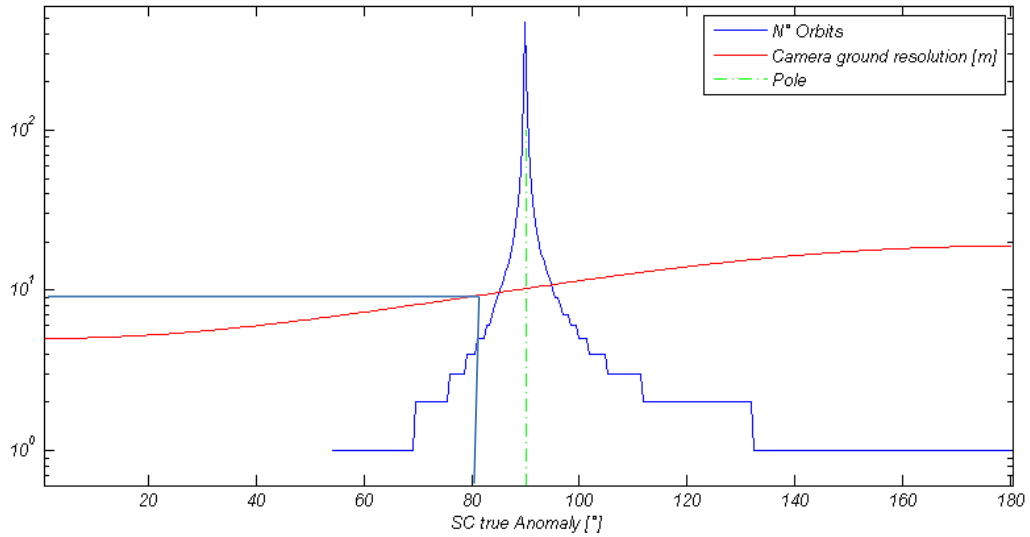

Figure 24 MPO polar orbit ground resolution and sample time constraints with an elliptical orbit of 400x1508km

At an higher latitude of 85°, we can reach 7 orbits and at 88°, 18 orbits (43.66 h) .
A latitude of 88° provides a max of 11.16° of azimuth variation.

6.6 Subset image dimensions

It is now estimated the minimum required image dimension and the consequent effects on the throughput with a square image. A strip image with the smaller side parallel to the Along-Track direction would be also acceptable, because it would reduce the constraint on the sampling time. It is acceptable to use a 5% or more of a full image for ill-conditioning avoidance in pattern matching procedure.
A 5% of a 2048x2048 (4.19Megapixel) is equivalent to a square image of 458x458 pixels.
If each pixel is defined in b/w with 14bit, an Image dimension of 7.3 Mbytes (the images will be compressed in jpeg format, this value is highly conservative) is obtained and a subset of 5% image dimension is of about 0.37Mbytes.

In an 80 days arc, 120 images are obtained if the sample time is, for example, 0.5d. The consequent navigation data volume becomes of about 60 MByte/arc. This is the dimensioning requirement, negligible with respect to the total downlink of 1550 Gb/y for MPO.

Table 3 Optical navigation throughput requirements in terms of data downlink

MPO total Downlink	1550 Gb/y
Optical navigation downlink: **10% of sampled image downloaded** **80d imaging arc length per year (radiom. Weakness period)** **0.5d of sampling time**	<120Mb/y
Optical navigation downlink: **10% of sampled image downloaded** **Continuous arc length** **0.5d of sampling time**	<600Mb/y

Furthermore with an on-board corner point extractor, the data set is not the entire overlapped image area but only a set of 2D image coordinates with a certain set of characteristics defined apriori, reducing the throughput of the methodology from Megabytes to Kilobytes (each pattern matching may produce a set of 500/1000 corner points per image).

6.7 Illumination variations

The scheduling for sequential polar images was achieved with a constraint of FOV visibility that permits overlap between two sequential images but also the illumination variations are to be evaluated.

A solar day on Mercury is about 176 terrestrial days. Therefore a mean azimuthal relative velocity of the sun as seen on the surface is about

$$\bar{\omega}_s = \frac{360}{176} = 2°/d$$

That's not a conservative value in our case, because we may have also inversion in a solar day, so we should take the peak velocity

$$\max(\omega_s) \cong 3.4°/d$$

Sun elevation for the targeted feature is about the colatitude of the feature because Mercury axial tilt is i=2.11'=0.035°
Sun azimuth in the feature sdr is

$$Az_{sun} = \Delta t \omega_{m\_solar\_day}$$

Where $\omega_{m\_solar\_day} = 2\pi/186d$

At near polar latitude, the dawn produces very elongated shadows that moves with the planet rotation changing abruptly the illumination conditions. With a latitude of acquisition of 86°, an interval of 10 orbits between samples is obtained, equivalent to 1 day of sampling time.

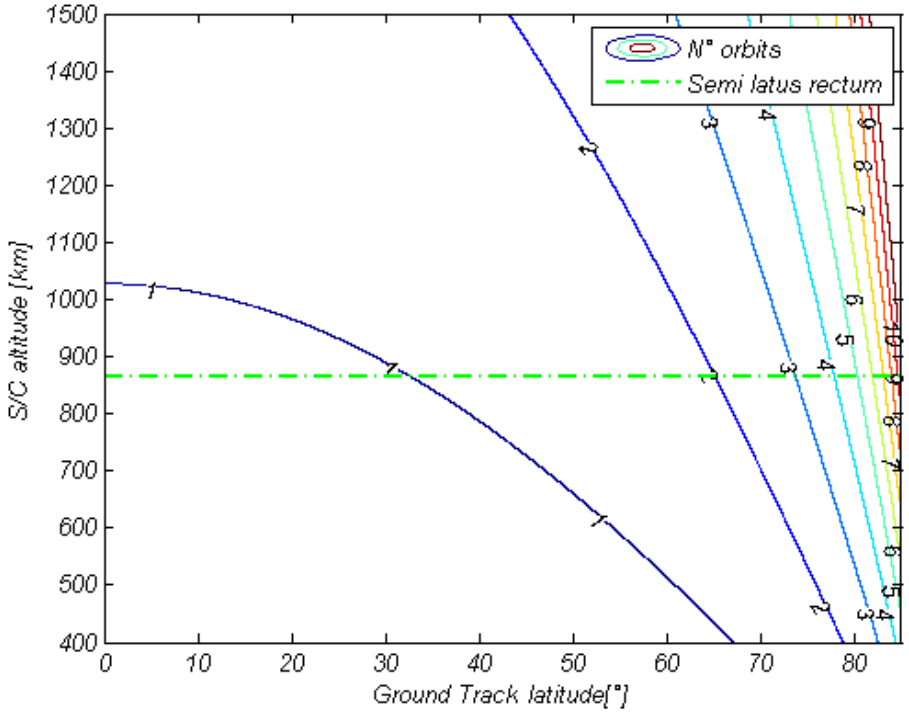

Figure 25. Isolines representing the number of successive orbits with 5% overlapping on Mercury's surface

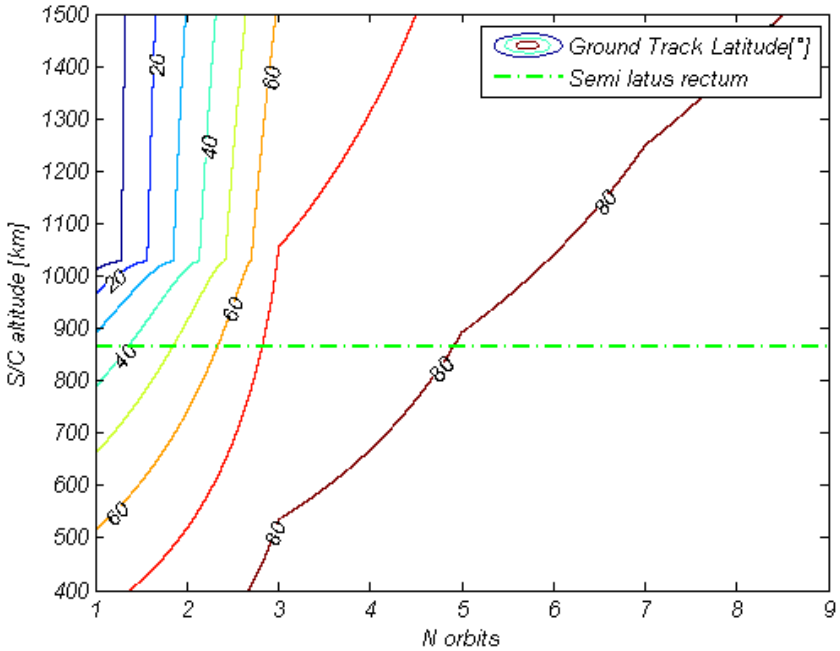

Figure 26. Isolines representing the latitude for which successive orbits undergo a 5% overlap at Mercury

Consequently an interval of 5-10 orbits between samples (equivalent to about 1 Earth day) at an observed latitude of 85° should be the baseline for a possible Mercury scenario.
The following figure represent isolines of solar Azimuth variation during mission time as a function of images acquisition frequency (image sampling time). It can be inferred that, for low impact in

pattern matching done using photometric salient points it is necessary to maintain a low sample time, otherwise it is necessary to use more sophisticated pattern matching that mix alternatives solution for shadowing compliance. Non equispaced sampling can also be chosen exploiting the non-homogeneity of the variation of azimuth (due to the particular behavior of the Sun at Mercury sky).

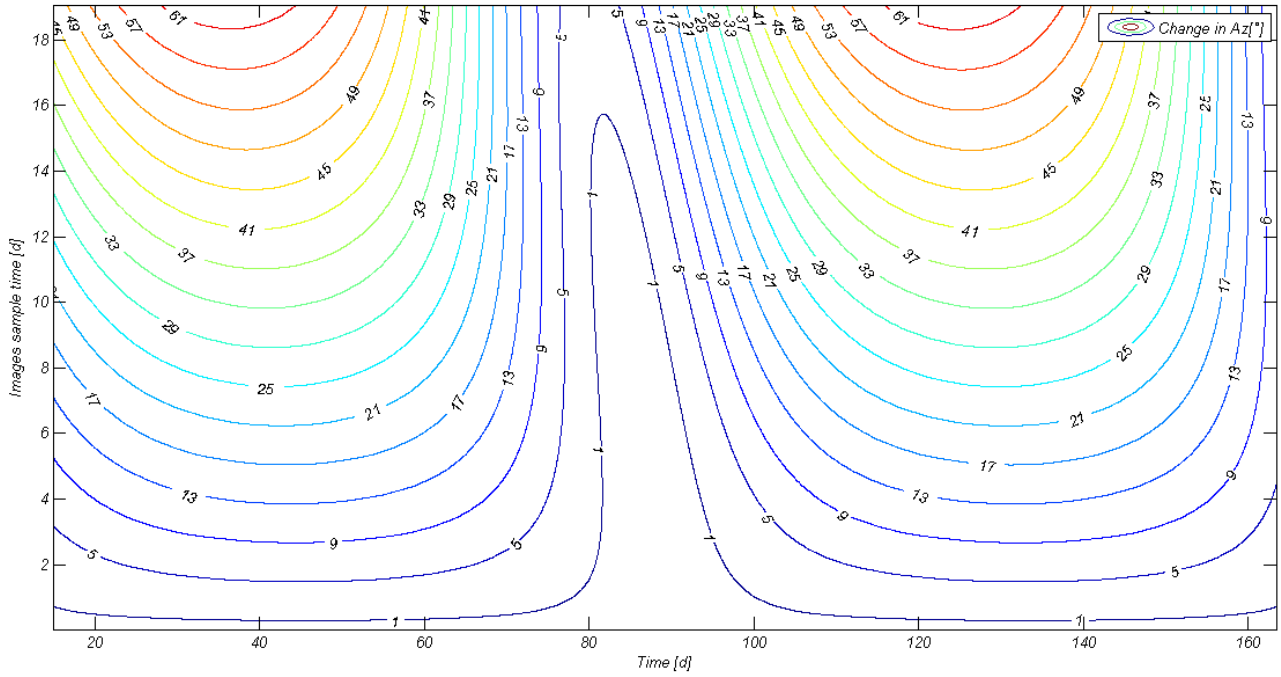

Figure 27 Solar Azimuth variation for an observer on the surface of Mercury at a latitude of 88° as a function of sampling time and mission time

In conclusion as a function of selected dT the illumination variations at

$$\Delta Az_{max} = T_s \max(\omega_s)$$
$$\Delta Az_{max}(85°) = 1.1°$$
$$\Delta Az_{max}(88°) = 2.2°$$

These are acceptable values for a pattern matching algorithm.
The relation between ground track elevation/azimuth and spacecraft true anomaly is the following (neglecting the planet inclination and considering a polar orbiter)

$$\begin{cases} Lat = \vartheta \ \ if\ \vartheta \in [0\ 90°] \\ Lat = 180° - \vartheta\ if\ \vartheta \in [90\ 180°] \end{cases}$$
$$El \approx 90 - Lat$$

As the real images from MPO will not be available in the next future, an operative scenario was built by replacing the camera Team output with the S/W simulator developed by the Computer Vision Group (CVG) of DEIS, capable of generating on demand synthetic images of the surface of Mercury for the analysis of the performance of a navigation algorithm for orbiter spacecraft. This analysis close the loop in an end-to-end evaluation of an optical navigation system, from images acquisition to navigation solutions.

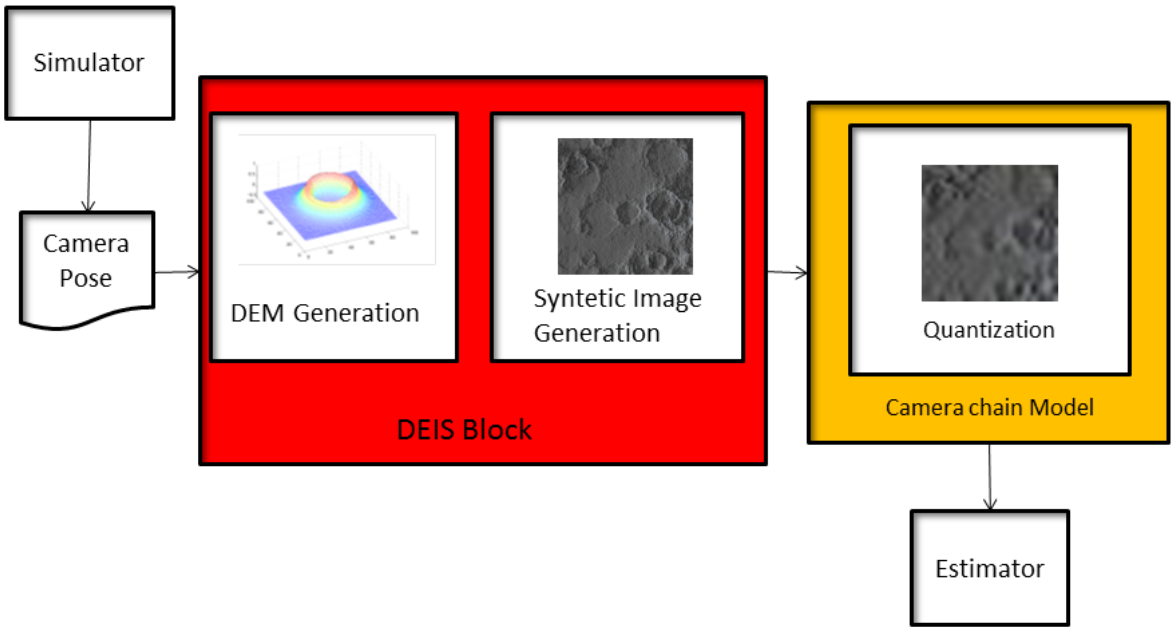

Figure 28 End-to-end synthetic optical navigation simulator

6.8 *Synthetic images simulation*

The procedure followed by DEIS to produce a trustworthy set of synthetic images is to

- build a Digital Elevation model (DEM) of the Mercury surface; random distributed impact craters, fractal details with Brownian motion algorithm;

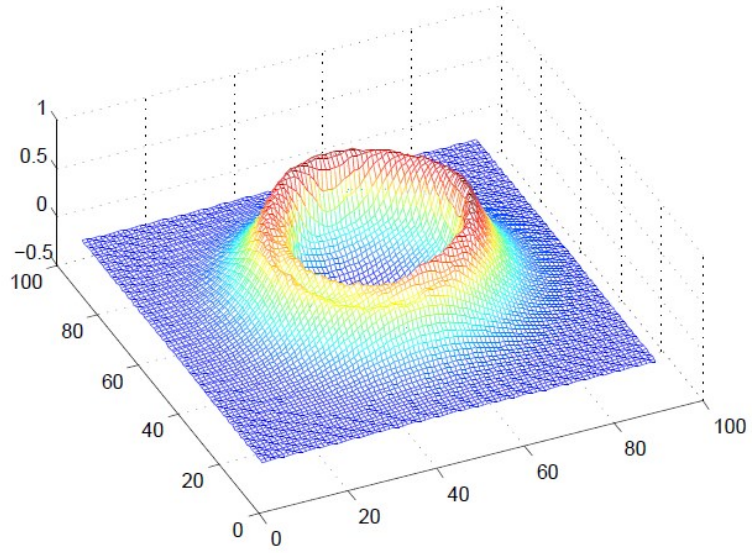

Figure 29 Crater DEM

- Raytracing of the final DEM, according to given altitude of the S/C and Sun azimuth and elevation angles

A set of images was requested to evaluate the PM in a sequential planning with operative constraints:

- Lat=88°: allows to carry out 2 tests varying sampling time from 8 h to 16 h (equivalent to a variation in azimuth from 5° to 10° between a pair of images). Sun elevation of 2° for the synthetic images.
- Lat=85°: permits to make 1 test with sample time of 8 h (equivalent to a variation in azimuth of 5° between a pair of images). Sun elevation of 5° for the synthetic images

Those two cases were generated sweeping from 0° to 90° with steps of 5°.
The total number of images was of 36; 18 images for the first case and 18 for the second.

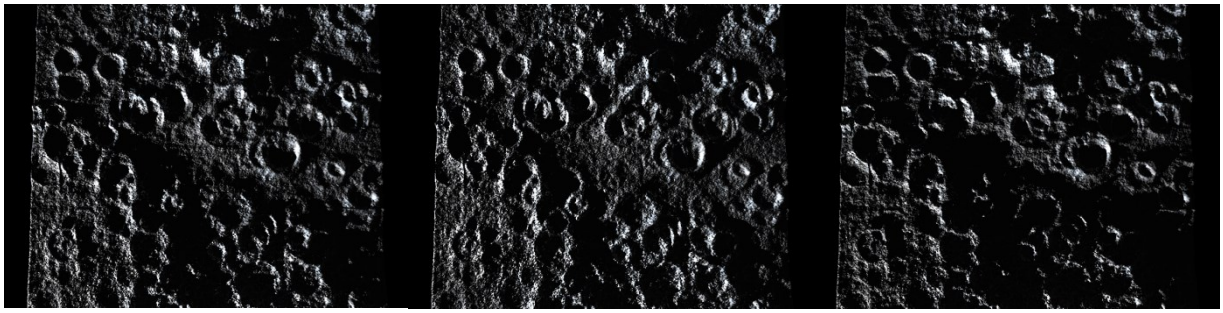

Figure 30 Az=[127 113 95] El=[7 10 12] 800x600 pixel

This analysis has been done to support CP usability due to the low computational demanding algorithm for extraction and matching.

6.9 Corner Points Extraction and Pattern matching

The Matlab® computer vision toolbox was used in this phase where corner points are detected by means of the Minimum value Shi & Tomasi corner detector.

The Matlab® *matchFeature* function was selected for this task, providing the features most likely to correspond and whose strongest matches are selected for the evaluation of the translation. Almost an exact matching is reached, as a consequence of the lacking of optical deformation models and a subtle time varying noise present in the camera hardware chain. The addition of those effects is currently in phase of implementation.

Capabilities of enhancement and reduction of the area of pattern matching (variable overlap as a function of images sampling time) and shape are implemented for future use as shown in Figure 31.

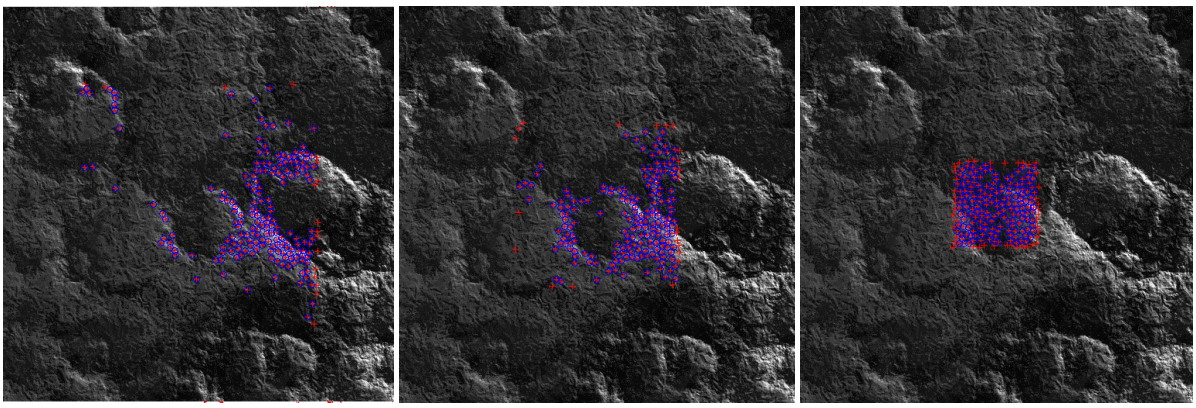

Figure 31 Variable simulated overlap for an image pair

The setup of synthetic images was processed and the qualitative evaluation of the pattern matching is consistent with the expectations, i.e. the shadowing effect degrades the pattern matching in terms of n° of matches found. also the sun angle with respect to the normal, producing more pronounced shadows, bias negatively the result of the matching.

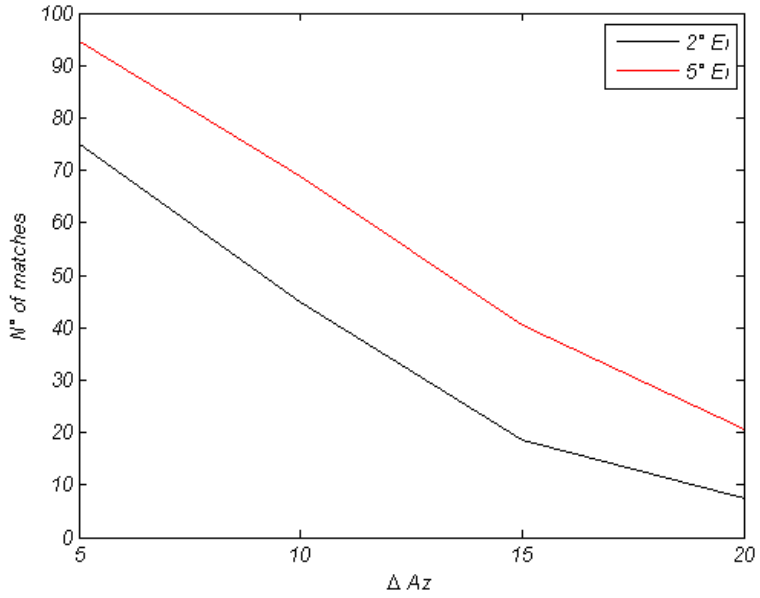

Figure 32 Matched points with varying Azimuth variation (shadows contribution to the Pattern Matching) on synthetic images of Mercury

A condition in which variations in solar Azimuth and Elevation are extreme, other solutions can be adopted, requiring probably a ground-based processing of the images.
The following table from (Palli, 2012) describe what could be possible alternatives

Table 4 Features pattern matching predispositions to change in Sun Az and El

PATTERN MATCHING ROBUSTNESS TO CHANGES OF SCALES AND ILLUMINATION				
PM METHOD PARAMETERS	Δ ALTITUDE	Δ ELEVATION	Δ AZIMUTH	NOTES
SCALE INVARIANT "GRADIENT BASED" FEATURES (SIFT, SURF)	High	Limited	Very limited	No dependence on surface features
GEOMETRIC FEATURES	Moderate	Moderate	Limited*	Preprocessing required
TRANSFORMED FEATURE SPACE + COMBINED MATCHING AND SHAPE FROM SHADING	Moderate**	High	High	Preprocessing required

7 Errors in Optical Observables

7.1 Error budget

An insight on the impact of optical observables to orbit determination can be evaluated apriori with an error budget in which all the sources of indetermination are taken into account. This analysis is used also for the successive process of simulation in which the errors described hereafter, are accounted for.
The main error sources described in this chapter depends on:

- Doppler and range accuracies
- S/C attitude
- Camera intrinsic parameters
- image time-tagging
- pattern matching

7.1.1 Doppler and Range

A Range Rate (Doppler) measurement, key element for orbit determination, depends on a multitude of factors that determine its accuracy. Without exploring in detail the full spectrum of contributes (the reader may refer to literature for a complete survey), only one major contribution is here considered; dispersive noise. This contribution is ionosphere and solar plasma dependent, in particular, for what concern the solar plasma, its contribution give rise to a wave shape in the noise, with the maximum amplitude centered in the condition in which the Sun-Earth-Probe angle reach zero, i.e. in a solar conjunction, while reaches the minimum in solar opposition. A well known methodology for the removal of this noise term at low SEP angles is to use a multifrequency link (Tortora, 2003), where the presence of a triple link composed by coherent X/X, X/Ka and Ka/Ka Band permits to build a linear combination of the three bands, deducing the uplink and downlink dispersive Doppler contribution that can be easily removed from the Doppler signal, generating a “plasma-free” synthetic frequency used for enhanced orbit determination.

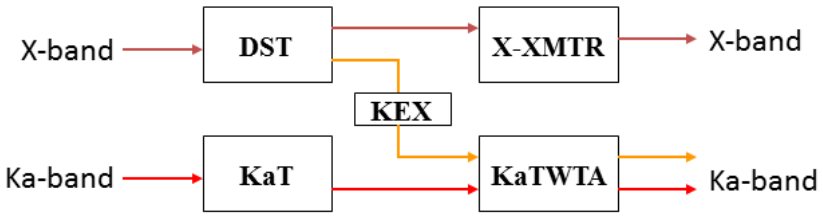

Figure 33 MPO Multifrequency Link Scheme

With the help of other studies about Cassini and MPO predicted accuracy, it is build a Doppler and range error budget for some particular conditions as Solar conjunction and opposition, and use of the triple-link, used successively for realistic simulations.

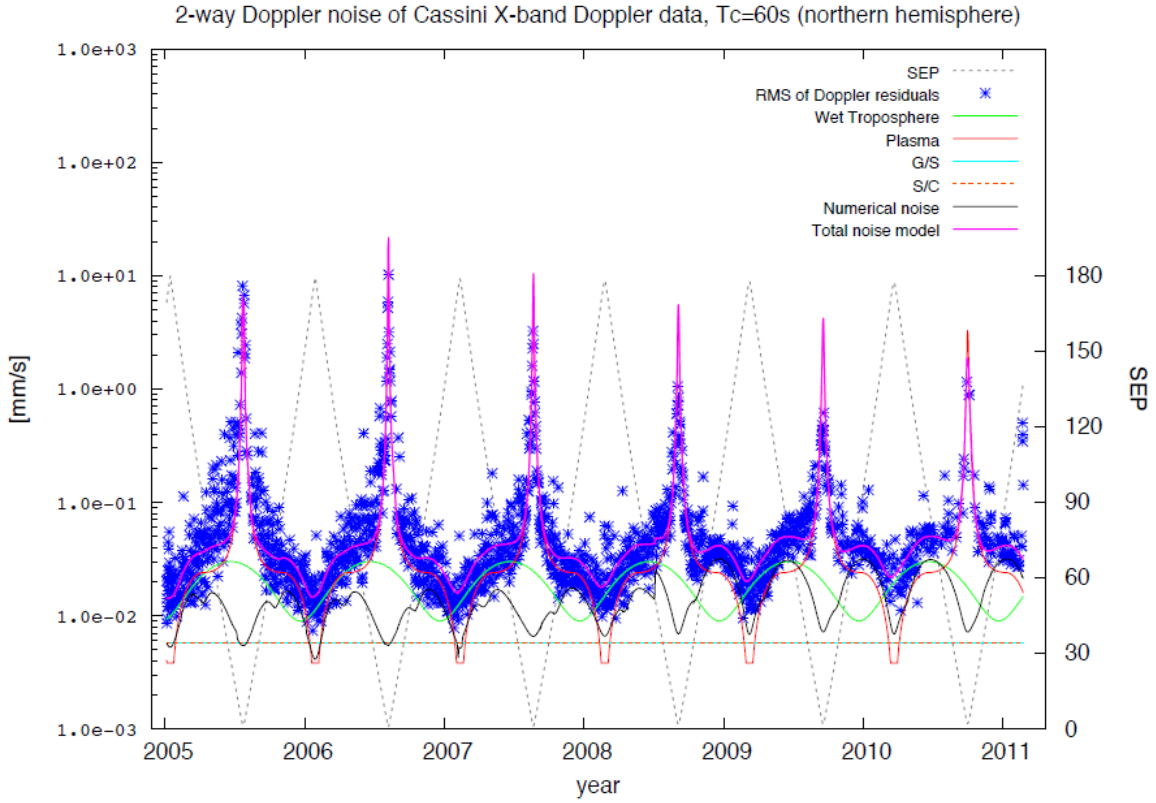

Figure 34 RMS of Cassini Doppler Residuals with Tc= 60 s (Iess, 2012)

Table 5 Range and Doppler accuracies comparisons

	X-Band Opposition	X-Band Conjunction	Ka-Band conjunction	Triple-link (SEP independent)
MPO	-	-	-	3 um/s @1000s Two-way
Messenger	0.06 mm/s @60 s 1σ two-way (Dominigue, 2007)	0.4mm/s @60s SEP=10° two-way	-	-
Cassini	0.02 mm/s @60s two-way	0.4 mm/s @60s SEP=10° two-way	0.05 mm/s @60s two-way SEP=10° (ADEV=2e-14 @1000s One-way)	3.4 um/s @60s two-way (ADEV=1e-14 @1000s One-way) (Iess, 2003)

Range accuracy is showed but was not considered in the simulations, although useful for constraining more the orbit of the spacecraft, for completeness it is showed the difference of the Messenger mission with the respect to the new MPO mission in which range is required to have very low un-

certainty to exploit the scientific objective of testing general relativity at higher accuracy during cruise.

Table 6 Range accuracies comparison for different Missions

MPO	20cm two-way
Messenger	13.6 m (45.32 ns one-way) 1σ two-way

7.1.2 Attitude error

The spacecraft attitude estimate derives from onboard AOCS exploiting a star tracker and gyroscopes, which are extremely accurate short-term but have a tendency to drift. This drift is operationally calibrated using onboard star trackers, which update the attitude estimate. Additional errors in attitude knowledge, due to mechanical misalignments, thermal instability, and other unknown sources contribute to the root mean square of the final error.

The pointing error is dependent on the imperfect maneuver of the reaction wheels to reach the ideal attitude commanded, this error is usually in the order of 100 arc seconds or more. However his value can be measured.

A pointing error budget should consider the following:

- Ground to orbit effects: effects that cannot be characterized on ground o which contribute residual error
- Thermal effects: effects which occur only in orbit
- AOCS performance: aspects of AOCS performance which contribute errors to the pointing performance
- Residual characterization effects: effect which remain despite pointing calibration

From a filtering point of view the attitude errors can be divided into:

- Random errors
- Systematic errors; expected also after calibration

Where systematic errors fall in 3 categories:

- Sensor and modeling parameter biases (misalignment and erroneous parameters)
- Incorrect of imperfect mathematical models (erroneous assumptions)
- Incorrect reference vector directions

In this analysis only the measurement error is considered using absolute values (AME) of the order of 2.5 to 5 arc seconds for MPO (internal communication) An orbit determination filter takes into account a measurement error that impact on the three axes of the spacecraft frame. In this analysis the same method was applied sharing the random measurement error for each axis, with a ratio of $\sqrt{3}$ of the AME.

It is not required to identify uniquely these three components because different configurations of these three angles may give the same result as this is an ill-posed problem. the only thing that matter is to make the optical measurement aware of the uncertainty associated with it.

How each error reproject on the camera pixels coordinates is approximately seen as:

- a camera rotation along the focal axis
- two camera rotations along the perpendicular axes, that result in a shift of the pixels

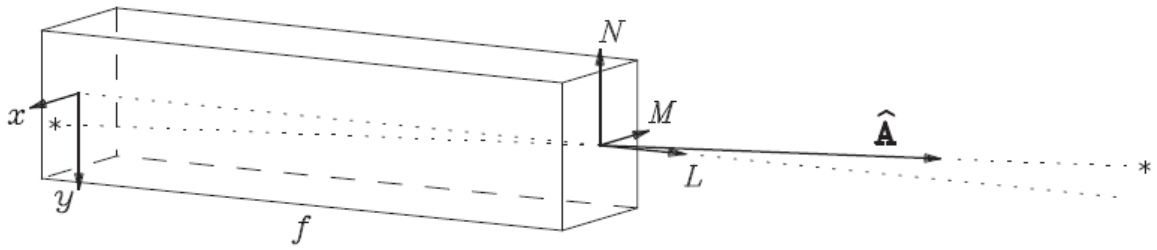

Figure 35 Camera Coordinates System

for example, on the corner of the MPO camera a rotation ϵ_L of 5 arcseconds gives

$$\epsilon_L \sqrt{2\left(\frac{l}{2}\right)^2} = 0.03\ pixel \quad (34)$$

While for the other two axis the attitude errors ϵ_N and ϵ_M projects directly in a pixel offset, the angular dimension of a pixel for MPO is of

$$\frac{dx}{f} = 2.5'' \quad (35)$$

therefore an angular error of 5'' is equivalent to an offset of two pixels.
An AME of 2.5-5'' at 1 sigma may be the state-of-the art of sophisticated spacecraft systems. For Cassini the AME is at least ten times higher.

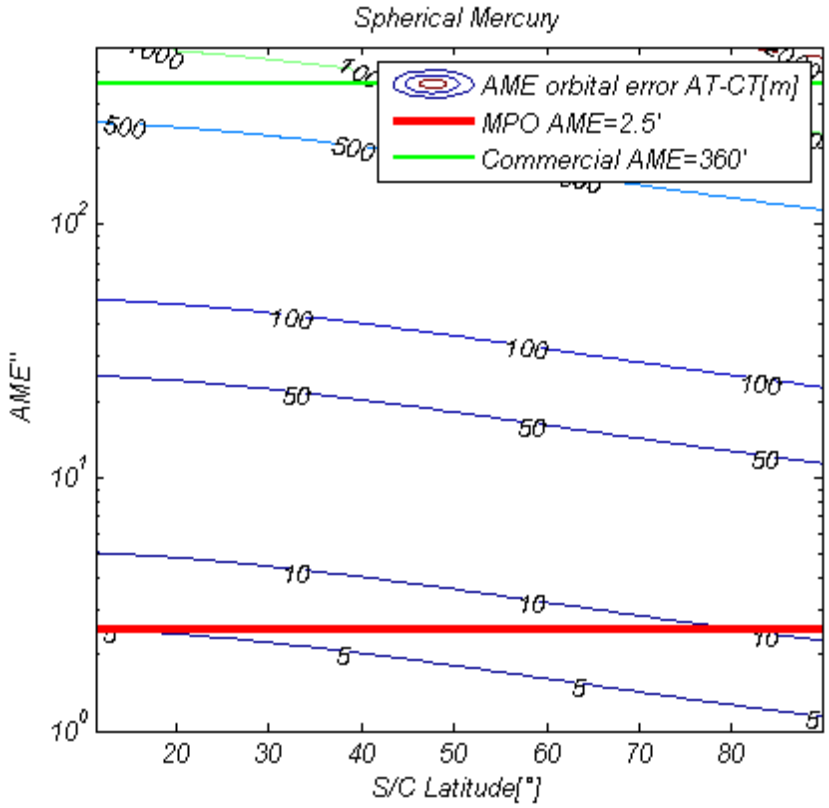

Figure 36 orbital position error due to a virtual translation equivalent to the AME error(from periherm to semilatus rectum)

An offset effect derived from systematic errors was also considered.

7.1.3 AME/TTE global effect

The ground-track error due to AME and TTE can be visualized in a square-root way by projecting its effect as a function the prove orbital velocity.
Definitions:

AME=Attitude Measurement Error

TTE=Time Tagging Error

AT= Along-track direction

CT=cross-track direction

AME and TTE are influent only in an Along-Track (AT) projected direction and Cross-track (CT) directions, in particular, TTE is influent only in AT as pinpointed in the following graph. The resulting envelope plot by the maximum deviation ofTTE and AME is draft in red.

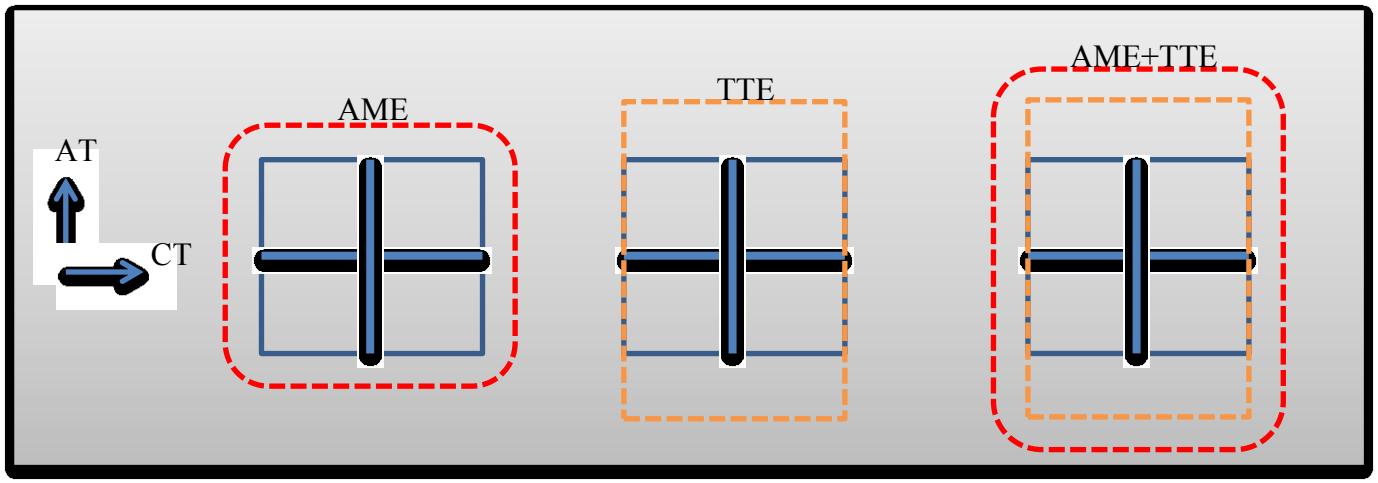

Figure 37 ATCT envelope error due to AME and TTE

7.1.4 Time tagging error

Time tagging is an error due to an offset between the scheduled spacecraft image acquisition timing and the real time of acquisition. This time offset depends on the shutter mechanism, and to the clock timing. It can be expected that a time tagging error would generate an error only in the Along-track projected direction of the camera. From other sources (Pfyffer, 2010) it is predicted that this value will be accurate at under the msec level, equivalent, for an orbiter travelling at 2.7 km/s (this is the value of MPO at periherm, the maximum velocity obtainable) the equivalent ground-track error is of about 28 cm for a TTE of 0.1 msec. To be conservative, a value of 1ms could be used, producing a ground track error at periherm of 2.7 meters.

7.1.5 Pattern Matching error

As described in the image processing chapter of this Thesis, the pattern matching error depend on the typology of salient points and matching algorithm selected, as well as the illumination conditions and the pose difference of the two images. Subpixel accuracy is easily attained with the modern pattern matching algorithms presents, although images with very low elevations cause problems and may fail (Gherardi, 2011).

1σ	**[arcsec]**	**Semi latus rectum [pixel]**	**Semi latus rectum (pe jected [m]**
Attitude Measurement Error	2.5	0.9	10.5 (4.8)

Time tagging Error (along-track)	1 ms	0.2	1.9 (2.6)
Pattern matching Error	0.26	0.1	1.1(0.5)
Total Error(RSS)			10.7 (5.5)

Figure 38 Camera error budget at Semi-latus Rectum

7.2 Unobservability to correlated errros

As in altimetric measurements, crossover optical observables suffer the insensitivity to spacecraft position errors with comparable period of the sampling time of the images. As a consequence, the unobservability of some errors affecting the orbit can cause over-optimistic uncertainty estimation.

The proof can be obtained while considering the crossover optical observables may defined in a simplified version as an homographic projection where the displacement contribute to the optical observables difference is dependent on a direct difference between the position of the probe at the two reference times of image acquisition

$$z_j = H\left(z_i - \frac{KR\left(X_i - X_j\right)}{z_{CAM}}\right) \quad (36)$$

A correlation can be observed considering that shorter time span gives higher error correlation. This error in the spacecraft state at the times of the image acquisition t_i and t_j is modeled as two contributions, a constant error, in common between the two states and a variable error. Shorter the time between two successive analysis, higher the constant part of the error, reducing the possibility to infer this effect of the orbit with this method.

$$\varepsilon_i = \varepsilon_0 + \Delta\varepsilon_i \quad (37)$$

$$\varepsilon_j = \varepsilon_0 + \Delta\varepsilon_j \quad (38)$$

and the true spacecraft state perturbed by this error becomes

$$X_i = X_i^T + \varepsilon_i \quad (39)$$

$$X_j = X_{j\,true}^T + \varepsilon_j \quad (40)$$

We may define also a boresight between the spacecraft centers and relate the positions at times t_i and t_j

$$X_j^T = X_i^T + \Delta X^T \quad (41)$$

$$X_j = X_i^T + \Delta X^T + \varepsilon_j \quad (42)$$

And finally the position difference is

$$X_j - X_i = \Delta X^T + \varepsilon_j - \varepsilon_i = \Delta X^T + \varepsilon_0 + \Delta\varepsilon_j - (\varepsilon_0 + \Delta\varepsilon_i) = \Delta X^T + \varepsilon_j - \varepsilon_{j-p} \quad (43)$$

Only the variable part of the error influence the computed observable while the dependence to the constant part is absent.

This error term is considered for a smooth trajectory (a trajectory with no abrupt changes as for a maneuver). Missions as MPO presents two daily desaturation maneuvers, made with a propulsion system, that increase the variable part of the error. This effect is observed by crossover optical observables.

A possible solution is to use the latest solution of a radiometric track, and exploit the image crossover only for the dark pass in which maneuver may be scheduled in a sequential Kalman filter.

Otherwise a registration is needed after a chain of observations is done, generating a set of crossovers that reuse past images after a longer time span. this procedure indeed comes closer to an absolute methodology, where landmarks are estimated with more and more images, though this methodology for a planetary orbiter may be suited only for a global postprocessing filtering scheme spanning years, for Science outputs.

7.3 Conclusions

Doppler and range could provides for MPO an uncertainty in the spacecraft position of 5-10 m for both the AT and CT directions while for the radial component also below meters (for a mission requirement as well as for simulations conducted in (Genova, 2012).
Those results are obtained thanks to a state-of-the art Doppler system, capable of achieving accuracies of the order of μm/s @1000, that thanks to a Multi-Frequency Link are, available at every solar angle, and to a novel wideband ranging system, based upon a pseudo-noise modulation scheme, that will be able to reach the great accuracy of 20 cm (two-way).
The results achieved with Doppler and range alone, discourage the use of an optical system for an MPO navigation system (and not in general for other missions with less demanding accuracy in Doppler and Range) but three different points are interesting to explore:

- The spacecraft accuracy achieved is referred to a whole year batch simulation; what happens in classical real-time navigation is that the accuracy is reduced in a sequential way,

step by step while new batches of tracking data arrive, assuming the uncertainties are higher in real-time with respect to a batch post processing at the end of the mission.

- The MPO spacecraft is covered daily by a period of tracking, what happens in the dark period (meaning there is no Doppler and range coverage), is that the uncertainty necessarily increase, though it would not increase very much because of the smoothness of the orbit, it will do it abruptly because of the presence of two desaturation maneuvers scheduled daily.
- Finally there are preferential directions of informations for range and Doppler, that contributes in the deterioration of the orbit accuracy in some periods, e.g. when the orbital plane is nearly perpendicular to the LOS between Earth and the probe.

These three points are a valid reason to go deeper in the analysis and try to evaluate some eventual improvements in the navigation approach.

8 Optical Observables implementation in an Orbit Determination Filter

8.1 Optical observable formulation

The definition requires to identify the main subjects that are the camera of the spacecraft and the target of the camera. In this particular situation the target will be a planet or a moon for which the combination of spacecraft altitude, focal length gives a view that is a local area of the surface of the target than the view of a limb. This condition is typical for a low orbiter or a flyby made for gravity purposes. Also the term of landmarks will be not used directly, it will be a subproduct of the computation. The camera is considered a payload of the spacecraft.
Once the inertial direction from the camera to the target, the orientation of the camera and the mapping projection are determined, the main informations for defining the observable are given.
Because c is not infinite, there is a delay time τ between the time the observed target emanate photons $t'$and the time of acquisition t at the camera.

$$t' = t - \tau \quad (44)$$

Therefore the direction of the camera is not the geometric position vector but the apparent position vector of the target, the direction from which the photons appear to come.
It the position of the target P^I in the solar system barycenter and its velocity $\dot{P}^I$ and the position R^I and velocity $\dot{R}^I$ of the observer are known, then the geometric relative position is

$$T(t) = R^I(t) - P^I(t) \quad (45)$$

The value of the light time is computed iteratively by

$$\tau = \frac{|T^I(t)|}{c} = \frac{|R^I(t) - P^I(t-\tau)|}{c} \quad (46)$$

Where $R(t)$ is the S/C position at half the exposure time at acquisition and $P(t-\tau)$ is the target position one light time before and c is light velocity (therefore as the observation is retarded).
Two iterations suffices.

$$\frac{\partial \tau}{\partial T^I} = \frac{sign(T^I)}{c} \quad (47)$$

In the condition of a low orbiting spacecraft with a nadir pointing camera a value for the first guess approximation of the light time is to choose the altitude of the spacecraft at the time of observation.

$$\tau = \frac{alt(t)}{c} \quad (48)$$

In this study the target position is the composition of the planet ephemeris and the body-fixed position of a point on the surface (the target of the acquisition)

$$P^I(t\ -\tau\ ) = P_M^I(t\ -\tau\ ) + p_T^I(t\ -\tau\ ) \quad (49)$$

The true position of the target as seen from the camera in an inertial SDR, corrected for light time, is:

$$T^I(t\ ) = R^I(t\ ) - P^I(t\ -\tau\ ) \quad (50)$$

Differing from the geometrical position of the target by

$$\Delta T^I(t\ ) = P^I(t\ ) - P^I(t\ -\tau\ ) \quad (51)$$

The camera and the target are not at rest with respect to the Solar System barycenter, then it is necessary to consider Planetary aberration, that shift the light direction toward the velocity apex of the camera, the apparent direction from which the camera detects the incoming light.
The apparent position is found by a Newtonian formulation sufficient for optical navigation purposes (if the reference frame notation is absent, it is intended as an inertial reference frame)

$$A(t\ ) = T(t\ ) + |T(t\ )|\left[\frac{\dot{T}(t\ )}{c}\right] \quad (52)$$

Where

$$\dot{T}(t\ ) = \dot{R}(t\ ) - \dot{P}(t\ -\tau\ ) \quad (53)$$

The velocity $\dot{P}(t\ -\tau\ )$ is computed only by means of newtonian effects (Moyer, s.d.).

$$\dot{P}^I(t\ -\tau\ ) = \frac{\partial \mathbb{T}_B^I(t\ -\tau\ )}{\partial t} P^B(t\ -\tau\ ) \quad (54)$$

Then a rotation matrix relating the inertial apparent vector reference frame with the camera reference frame is given

$$A^C(t\ ) = -\mathbb{T}_I^C(t\ )A^I(t\ ) \quad (55)$$

A minus value indicate that the boresight vector positive in the camera to object direction.
Where, in the most general case of a camera with azimuth/elevation control

$$\mathbb{T}_I^C(t\ ) = \mathbb{R}_y(El\ )\mathbb{R}_z(Az\ )\mathbb{A}_I^{SC}(t_i) \quad (56)$$

And $\mathbb{A}_I^{SC}(t\ )$ is the attitude of the S/C from the AOCS determination system
Finally a gnomonic projection is given that project the tridimensional position of the target in the camera reference frame to the image plane in units of length.

$$\begin{bmatrix} x \\ y \end{bmatrix} = \frac{f}{A_3^C(t_i)} \begin{bmatrix} A_1^C(t_i) \\ A_2^C(t_i) \end{bmatrix} \quad (57)$$

f is the focal length (usually expressed in millimeters).

Real optics can suffer from five classical third-order aberrations:

- Spherical aberration

- Coma
- Distortion
- Astigmatism
- Curvature of field

The three dominant terms arise from cubic radial distortion ϵ_r and tip and tilt misalignments ϵ_M and ϵ_N.

$$\begin{bmatrix}\Delta x\\ \Delta y\end{bmatrix} = \begin{bmatrix}x(x^2+y^2) & xy & x^2\\ y(x^2+y^2) & y^2 & xy\end{bmatrix}\begin{bmatrix}\epsilon_r\\ \epsilon_M\\ \epsilon_N\end{bmatrix} \quad (58)$$

And the corrected image location becomes

$$\begin{bmatrix}x'\\ y'\end{bmatrix} = \begin{bmatrix}x+Dx\\ y+Dy\end{bmatrix} \quad (59)$$

The other terms of aberration can in general be absorbed in the camera calibration.
The next step is to convert the image plane coordinates in units of length to the effective pixel positions in adimensional units referred as pixels coordinates. A digital picture contains a rectangular array of numbers, each of which is a pixel (contraction of picture element). from TV cameras terminology the horizontal coordinate is referred to as sample, while the vertical direction as line coordinate (because the pictures were sampled while doing line-by-line scans). There is also no agreement if to define the first pixel coordinate as (0,0) or (1,1), we will consider it as a function of the programming language used (Owen, 2011).

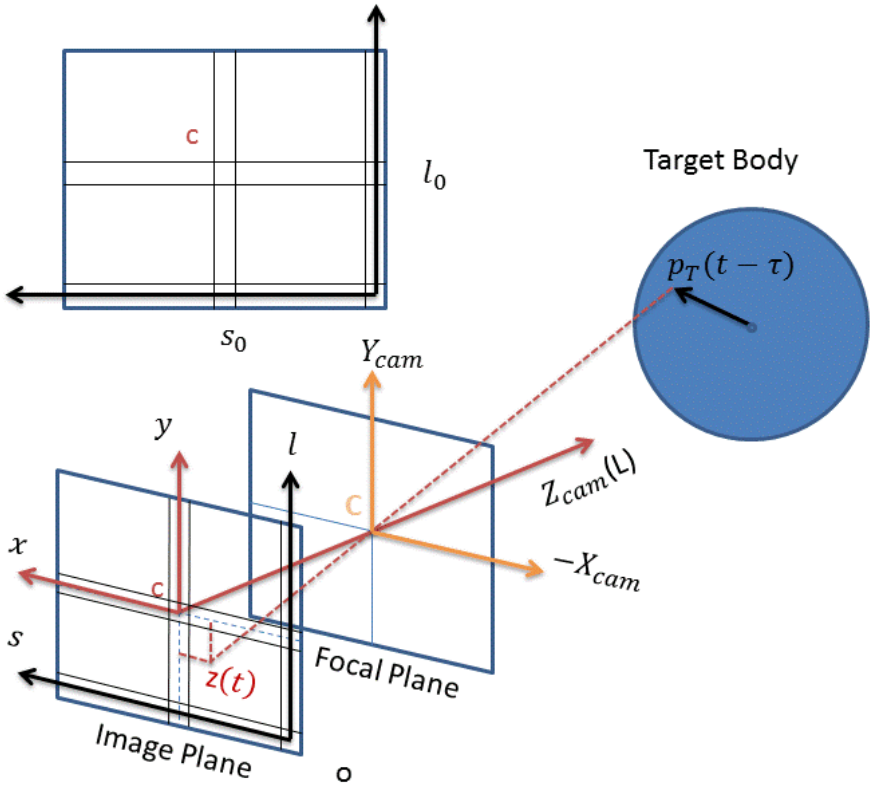

Figure 39 Camera coordinate reference frame

A simple linear transformation suffices in converting length coordinates to sample and line coordinates

$$\begin{bmatrix} s \\ l \end{bmatrix} = \begin{bmatrix} s_0 \\ l_0 \end{bmatrix} + \begin{bmatrix} K_x & K_{xy} \\ K_{yx} & K_y \end{bmatrix} \begin{bmatrix} x' \\ y' \end{bmatrix} \quad (60)$$

Where the matrix *K* contains the reciprocal of the pixel dimensions(pixel/mm). Notice that there can be also a rotation in *K*. s_0 and l_0 represents the coordinates of the optical axis that for definition gives x=y=0.
In this formulation there is an evidence that an implicit rotation in *K* is effectively the same as a rotation of the camera body itself, therefore it is common practice to hold K_x fixed and to hold K_{xy} fixed at zero. then *f* can be estimated to account for overall variations in scale, K_y to determine aspect ratio of the pixel grid, and K_{yx} to find the angle between the sample and line axes.

Now it is necessary to describe the landmark position with respect to another view, describing the possible existing relation between two overlapped images.
Two overlapped images acquired with the same camera, are therefore determined by the sampling time. Each sampling time t_i and t_j refer to a different position of the spacecraft through the orbit and will determine a different path between the viewed target and the camera.
Schematically the geometry can be decomposed in participants and legs.
Participants:

1. Spacecraft position and attitude at time t_j
2. Planet ephemeris, orientation and target position at time $t_j - \tau_j$

3. Spacecraft position and attitude at time t_i
4. Planet ephemeris, orientation and target position at time $t_j - \tau_j$

Legs:

1. Leg j, defined as the geometry including the camera and the target when the reference image j is shot
2. Leg I, defined as the geometry including the camera and the target when the secondary image i is shot

The picture of the pair, that has been acquired first, is defined (arbitrarily) as the reference, and as secondary, the picture of the pair acquired last.

$$t_j < t_i$$

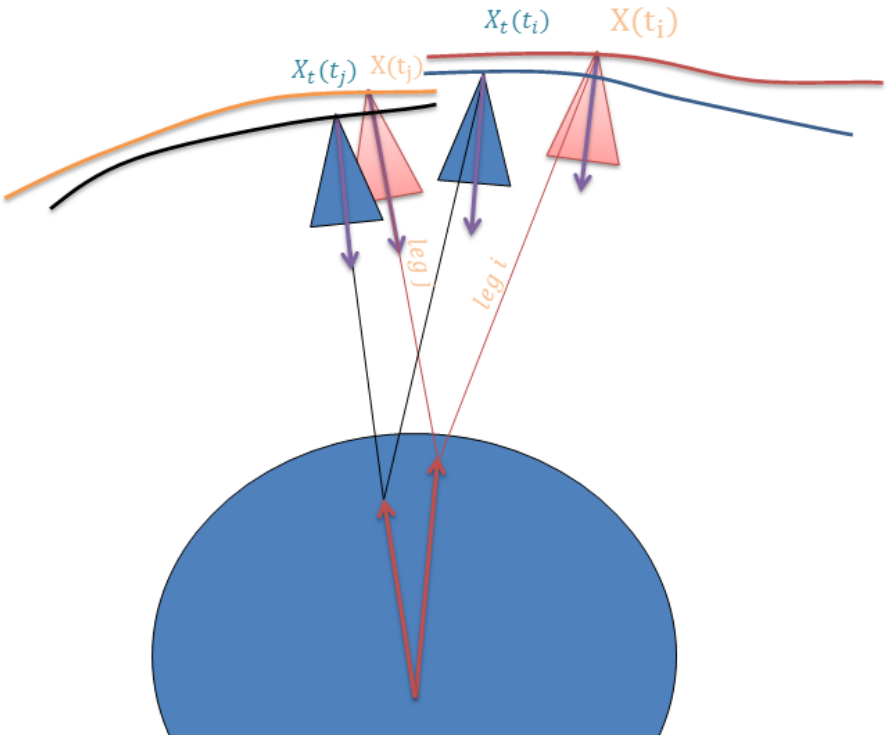

Figure 40 Overlap images legs geometry

The true positions are, for each leg

$$T^I(t_i) = R^I(t_i) - P^I(t_i - \tau_i) \quad (61)$$
$$T^I(t_j) = R^I(t_j) - P^I(t_i - \tau_j) \quad (62)$$

In a body-fixed reference frame we expect that each point seen in two overlapped images, acquired at the sampling time t_i and t_j , is the same

$$P^B(t_i - \tau_i) = P^B(t_j - \tau_j) \quad (63)$$

substituting, a relation between the true position at time t_i with respect to the landmark position at time $t_j - \tau_j$ can be formulated

$$T^I(t_i) = R^I(t_i) - P^I(t_i - \tau_i) = R^I(t_i) - \mathbb{T}_B^I(t_i - \tau_i)P^B(t_i - \tau_i) = R^I(t_i) - \mathbb{T}_B^I(t_i - \tau_i)P^B(t_j - \tau_j) \quad (64)$$

The next simplification permits to formulate a crossover optical observable in an easiest way, the concept is that instead of having a relation between all pixel coordinates in one image with all pixel coordinates in an overlapped image, it is chosen to relate only the image center of one image to the overlapped one.
As a consequence, with the camera center at time t_j, projected on the surface at time $t_j - \tau_j$, one can obtain $P^B(t_j - \tau_j)$ of the camera center.

$$P^B(t_j - \tau_j) = \mathbb{T}_B^I(t_j - \tau_j)^{-1} P^I(t_j - \tau_j) \quad (65)$$

In the camera reference frame

$$A^C(t_j) = \begin{bmatrix} 0 \\ 0 \\ A_3^C(t_j) \end{bmatrix} \quad (66)$$

with this definition, the distortion contributes do not apply because x(t_j)=y(t_j)=0
Then $A_3^C(t_j)$ is computed by applying raytracing to an ellipsoid fitting the target planet. This is a methodology that cannot satisfy a possible mission to an asteroid where the shape depart highly from an ellpisoid model, and a digital elevation model should be applied in the raytracing procedure.
A rotation from the camera frame to the inertial frame is applied

$$A^I(t_j) = -\mathbb{T}_I^C(t_j)^{-1} A^C(t_j) \quad (67)$$

And the aberration term has to be computed inverting the following formula

$$A(t_j) = T(t_j) + |T(t_j)| \left[\frac{\dot{T}(t_j)}{c}\right] \quad (68)$$

And from

$$T(t_j) = R(t_j) - P(t_j - \tau_j) \quad (69)$$

the inertial landmark position is recovered

$$P^I(t_j - \tau_j) = R(t_j) - T(t_j) \quad (70)$$

τ_j is then evaluated

$$\tau_j = \frac{|R(t_j) - P(t_j - \tau_j)|}{c} \quad (71)$$

and all terms required to compute the optical observables are given.

8.2 Attitude error in the optical observables

Typical values for an error in the camera pointing are of the order of arc minutes or less therefore can be considered small, with this in mind, the formulation of the optical observables can be augmented with an attitude matrix that consider also an intermediate infinitesimal rotation accounting

for additional frames; an offset in the spacecraft frame accounting for pointing offset due to reaction wheels inaccuracy and a camera pointing error due to uncertainties of various sources as the time varying thermal effects on the optics.
S/C Attitude with respect to an inertial reference frame is a ground truth as it's provided by the AOCS team. In simulation, a CK kernel with a S/C nadir pointing condition can be produced. then the rotation transformation between the S/C frame and the camera frame can be modeled in the following way.
To consider camera attitude measurement errors, it is necessary to know what there is inside $\mathbb{T}_I^C$, the true attitude matrix provided by the AOCS team is$\widetilde{\mathbb{T}}_I^{SC}$, the other are estimated or considered

$$\mathbb{T}_I^C = \mathbb{T}_{CB}^C \mathbb{T}_{CB'}^{CB} \mathbb{T}_{SC'}^{CB'} \mathbb{T}_{SC}^{SC'} \widetilde{\mathbb{T}}_I^{SC} \quad (72)$$

In the former equation, there are five reference frames:

1. Inertial frame
2. S/C frame, AOCS determined Ground truth
3. S/C measurement error (AME)corrected frame
4. Camera basement frame
5. Camera systematic pointing error corrected frame
6. Camera frame

with the following relations

$$\mathbb{T}_{CB'}^{CB} = \{I - [e_x]\} \quad (73)$$

$$\mathbb{T}_{SC'}^{CB'} = \{I - [\delta\theta_x]\} \quad (74)$$

where e is a bias vector that take into account systematic pointing errors (referred to camera misalignment) and $\delta\theta\,(t)$ is a time varying vector coping with attitude measurement errors of the attitude determination system that can be driven by a white noise.
A systematic pointing error is not associated with the pointing error that instead is variable through time and known. The typical sources of attitude data is a product made by NAIF, a CK kernel, but this kind of data do not provide an associated uncertainty given by an AOCS product $\widetilde{\mathbb{T}}_I^{SC}$, therefore a reasonable uncertainty value has to be assumed.
The attitude measurement error can be modeled as a process noise, to have an associated covariance that should not reduce with more observations (as the associated noise of the AOCS determination system) (Stastny N., 1998).

1.1 Optical observables partial derivatives

Once image processing, produces the observed observables $(s, l)_c$, these measurements must be processed in an orbit determination filter, along with radiometric data (Doppler, range and so on), and a priori uncertainties, with the target of estimating the spacecraft state. This process require residuals and partial derivatives of the measurements with respect to filter parameters. Partial derivatives are found differentiating the aforementioned equations for the predicted optical measurements. Parameters for which partial derivatives may be computed, are subdivided in 4 main categories:

1. Dynamic parameters
2. Target parameters
3. Optical parameters

4. Optical bias parameters

Dynamical parameters influence the spacecraft trajectory and include the spacecraft state at epoch; the state and mass of perturbing bodies; the scheduled maneuvers inside the processed window of time including the epoch and all the data arc to be filtered; non gravitational accelerations.

Target parameters perturbs the state of the target. Orbital elements, masses, and so on.

Optical parameters affect the gnomonic projection into sample and line. they do not affect the spacecraft trajectory, or the target ephemeris, but they enter in the calculation of the measurement.

Optical bias parameters are intended to absorb systematic errors.

Or from a filter point of view described in the chapter about the orbit determination process:
1. dynamic parameters
2. bias parameters
3. stochastic parameters
4. consider parameters

8.2.1 Single arc vs. multi arc considerations

Generally the formulation of partial derivatives, changes if the filter is capable of processing data in a multi-arc formulation, i.e. a formulation where local parameters (the spacecraft state), are not correlated between arcs.

In a classical estimation the optical observable defined above may be formulated generally as

$$\frac{\partial z}{\partial q} = \frac{\partial z}{\partial s_i}\frac{\partial s_i}{\partial q} + \frac{\partial z}{\partial s_k}\frac{\partial s_k}{\partial q} + \frac{\partial z}{\partial q} \quad (75)$$

where q is a parameter influencing the measurements.

Substituting q with the spacecraft state at epoch it becomes

$$\frac{\partial z}{\partial s_{0j}} = \frac{\partial z}{\partial s(t)}\frac{\partial s(t)}{\partial s_{0j}} + \frac{\partial z}{\partial q}\frac{\partial q}{\partial s_{0j}} = \frac{\partial z}{\partial s_i}\frac{\partial s_i}{\partial s_{0j}} + \frac{\partial z}{\partial s_j}\frac{\partial s_j}{\partial s_{0j}} \quad (76)$$

In a multi-arc formulation, partials should be computed with respect to each local parameter from any arc that enter in the optical observable formulation defined above.

For example if the observable depends on the local spacecraft state defined in two different arcs defined with a window $[t_{s1}, t_{e1}]$ and $[t_{s2}, t_{e2}]$ with

$$t_{s1} < t_j < t_{e1}$$

$$t_{s2} < t_i < t_{e2}$$

$$t_{e1} < t_{s2}$$

and

$$z = s[s(t_i), s(t_j)] \quad (77)$$

then

$$\frac{\partial z}{\partial s_{0j}} = \frac{\partial z}{\partial s_i}\frac{\partial s_i}{\partial s_{0i}}\frac{\partial s_{0i}}{\partial s_{0j}} + \frac{\partial z}{\partial s_j}\frac{\partial s_j}{\partial s_{0j}} + \frac{\partial z}{\partial q}\frac{\partial q}{\partial s_{0j}} = \frac{\partial z}{\partial s_j}\frac{\partial s_j}{\partial s_{0j}} \quad (78)$$

$$\frac{\partial z}{\partial s_{0i}} = \frac{\partial z}{\partial s_i}\frac{\partial s_i}{\partial s_{0i}} + \frac{\partial z}{\partial s_j}\frac{\partial s_j}{\partial s_{0j}}\frac{\partial s_{0j}}{\partial s_{0i}} + \frac{\partial z}{\partial q}\frac{\partial q}{\partial s_{0j}} = \frac{\partial z}{\partial s_i}\frac{\partial s_i}{\partial s_{0i}} \quad (79)$$

$$\frac{\partial z}{\partial q} = \frac{\partial z}{\partial s_i}\frac{\partial s_i}{\partial q} + \frac{\partial z}{\partial s_j}\frac{\partial s_j}{\partial q} + \frac{\partial z}{\partial q} \quad (80)$$

Showing that the two arcs are in general uncorrelated but the measure itself has a dependence on both.

The primary partial derivatives used for optical spacecraft navigation are now formulated.

1.1.1 Partials of dynamic and target parameters

The main vector parameter for which is necessary to express partial derivatives of the measurements is the spacecraft state at epoch.
The first differentiation can be done for the true vector

$$\frac{\partial T(t_i)}{\partial q} = \frac{\partial R(t_i)}{\partial q} - \frac{\partial P(t_i-\tau_i)}{\partial q} + \frac{\partial P(t_i-\tau_i)}{\partial (t_i-\tau_i)}\frac{\partial \tau_i}{\partial q} \quad (81)$$

$\frac{\partial R(t_i)}{\partial q}$ is considered available from the Orbit Determination Software used or interpolated from files.
Because $\tau_i = \frac{|T(t_i)|}{c}$

$$\frac{\partial \tau_i}{\partial q} = \frac{1}{c}\frac{\partial |T(t_i)|}{\partial q} = \frac{1}{c}\left(\hat{T}(t_i)\cdot\frac{\partial T(t_i)}{\partial q}\right) \quad (82)$$

For this there is an exact solution

$$\frac{\partial T(t_i)}{\partial q} = \frac{\partial R(t_i)}{\partial q} - \frac{\partial P(t_i-\tau_i)}{\partial q} + \frac{\dot{P}(t_i-\tau_i)}{c}\frac{\dot{T} - \frac{\partial\left(R(t_i)-P(t_i-\tau_i)\right)}{\partial q}}{1+\left(\frac{\dot{P}\cdot\dot{T}}{c}\right)} \quad (83)$$

Then the aberration vector can be differentiated

$$\frac{\partial A(t_i)}{\partial q} = \frac{\partial T(t_i)}{\partial q} + \frac{\dot{T}(t)}{c}\left(\hat{T}\cdot\frac{\partial T(t_i)}{\partial q}\right) + \frac{|T|}{c}\frac{\partial \dot{T}(t_i)}{\partial q} \quad (84)$$

and for the true vector velocity

$$\frac{\partial \dot{T}(t_i)}{\partial q} = \frac{\partial[\dot{R}^I(t_i) - \dot{\mathbb{T}}_B^I(t_i-\tau_i)P^B(t_i-\tau_i)]}{\partial q} = \frac{\partial \dot{R}^I(t_i)}{\partial q} - \frac{\partial \dot{\mathbb{T}}_B^I(t_i-\tau_i)}{\partial q}P^B(t_i-\tau_i) - \dot{\mathbb{T}}_B^I(t_i-\tau_i)\frac{\partial P^B(t_i-\tau_i)}{\partial q} \quad (85)$$

the dependency of the landmark with respect to the rotational state of the target body at time t_i is highlighted.
The above partials should be rotated then into a camera coordinate system

$$\frac{\partial A^C}{\partial q} = \mathbb{T}_I^C(t_i)\frac{\partial A^I}{\partial q} + \frac{\partial \mathbb{T}_I^C(t_i)}{\partial q}A^I \quad (86)$$

The dynamic parameters usually propagate only through the first term; the second term handles the various pointing angles errors which enters $\mathbb{T}_I^C(t_i)$.
Then differentiating the relation for the transformation into the focal plane

$$\begin{bmatrix}\frac{\partial x}{\partial q}\\ \frac{\partial y}{\partial q}\end{bmatrix} = \frac{f}{A_3^C(t_i)}\begin{bmatrix}\frac{\partial A_1^C}{\partial q}\\ \frac{\partial A_2^C}{\partial q}\end{bmatrix} - \frac{f}{\left(A_3^C(t_i)\right)^2}\begin{bmatrix}A_1^C(t_i)\\ A_2^C(t_i)\end{bmatrix}\frac{\partial A_3^C}{\partial q} \quad (87)$$

the remaining differentiations depend on the camera deformation

$$\begin{bmatrix}\frac{\partial \Delta x}{\partial q}\\ \frac{\partial \Delta y}{\partial q}\end{bmatrix} = \begin{bmatrix}\frac{\partial \Delta x}{\partial x} & \frac{\partial \Delta x}{\partial y}\\ \frac{\partial \Delta y}{\partial x} & \frac{\partial \Delta y}{\partial y}\end{bmatrix}\begin{bmatrix}\frac{\partial x}{\partial q}\\ \frac{\partial y}{\partial q}\end{bmatrix} \quad (88)$$

The corrected position partials are expressed as

$$\begin{bmatrix}\frac{\partial x'}{\partial q}\\ \frac{\partial y'}{\partial q}\end{bmatrix} = \begin{bmatrix}\frac{\partial x}{\partial q}\\ \frac{\partial y}{\partial q}\end{bmatrix}_{\Delta\bar{x}=cost} + \begin{bmatrix}\frac{\partial \Delta x}{\partial q}\\ \frac{\partial \Delta y}{\partial q}\end{bmatrix} = \begin{bmatrix}\frac{\partial x}{\partial q}\\ \frac{\partial y}{\partial q}\end{bmatrix}_{\Delta\bar{x}=cost} + \frac{\partial C}{\partial q}\begin{bmatrix}\epsilon_1\\ \epsilon_2\\ \epsilon_3\end{bmatrix} + C\frac{\partial}{\partial q}\begin{bmatrix}\epsilon_1\\ \epsilon_2\\ \epsilon_3\end{bmatrix} =$$

$$\begin{bmatrix}\frac{\partial s}{\partial q}\\ \frac{\partial l}{\partial q}\end{bmatrix} = \frac{\partial K}{\partial q}\begin{bmatrix}x'\\ y'\end{bmatrix} + K\begin{bmatrix}\frac{\partial x'}{\partial q}\\ \frac{\partial y'}{\partial q}\end{bmatrix} \quad (89)$$

The homographic formulation between two different observations in time, shows up relating the body-fixed surface vector and the leg j, providing a dependence to the state at the epoch relative to leg j.

$$\frac{\partial P(t_i-\tau_i)}{\partial q} = \frac{\partial P(t_i-\tau_i)}{\partial R(t_j)}\frac{\partial R(t_j)}{\partial q} \quad (90)$$

expanding this formulation

$$\frac{\partial P(t_i-\tau_i)}{\partial q} = \frac{\partial[\mathbb{T}_B^I(t_i-\tau_i)P^B(t_i-\tau_i)]}{\partial q} = \frac{\partial\left[\mathbb{T}_B^I(t_i-\tau_i)\mathbb{T}_I^B(t_j-\tau_j)\left[R^I(t_j)-T^I(t_j)\right]\right]}{\partial q} =$$
$$\frac{\partial \mathbb{T}_B^I(t_i-\tau_i)}{\partial q}\mathbb{T}_I^B(t_j-\tau_j)P^B(t_i-\tau_i) + \mathbb{T}_B^I(t_i-\tau_i)\frac{\partial \mathbb{T}_I^B(t_j-\tau_j)}{\partial q}P^B(t_i-\tau_i) + \mathbb{T}_B^I(t_i-\tau_i)\mathbb{T}_I^B(t_j-\tau_j)\left[\frac{\partial R^I(t_j)}{\partial q}-\frac{\partial T^I(t_j)}{\partial q}\right] \quad (91)$$

in which now appear also the dependency with rotational state at time t_j,
The partial derivatives can now be specialized to each single parameter considered for a possible estimation.

8.2.2 Spacecraft state partials

The partials of the optical observables with respect to the spacecraft state at time t_i are computed by the following relation

$$\frac{\partial \boldsymbol{z}}{\partial \boldsymbol{R}(t_i)} = \frac{\partial \boldsymbol{z}}{\partial \boldsymbol{x'}} \frac{\partial \boldsymbol{x'}}{\partial \boldsymbol{x}} \frac{\partial \boldsymbol{x}}{\partial \boldsymbol{A^C}(t_i)} \frac{\partial \boldsymbol{A^C}(t_i)}{\partial \boldsymbol{A^I}(t_i)} \frac{\partial \boldsymbol{A^I}(t_i)}{\partial \boldsymbol{T^I}(t_i)} \frac{\partial \boldsymbol{T^I}(t_i)}{\partial \boldsymbol{R^I}(t_i)} \quad (92)$$

in which each contribution is listed hereafter

$$\frac{\partial \boldsymbol{z}}{\partial \boldsymbol{x'}} = K \quad (93)$$

$$\frac{\partial \boldsymbol{x'}}{\partial \boldsymbol{x}} = I_2 + \begin{bmatrix} \frac{\partial \Delta x}{\partial x} & \frac{\partial \Delta x}{\partial y} \\ \frac{\partial \Delta y}{\partial x} & \frac{\partial \Delta y}{\partial y} \end{bmatrix} \quad (94)$$

$$\begin{bmatrix} \frac{\partial \Delta x}{\partial x} \\ \frac{\partial \Delta x}{\partial y} \\ \frac{\partial \Delta y}{\partial x} \\ \frac{\partial \Delta y}{\partial y} \end{bmatrix} = \begin{bmatrix} r^2 + 2x^2 & y & 2x \\ 2xy & x & 0 \\ 2xy & 0 & y \\ r^2 + 2y^2 & 2y & x \end{bmatrix} \begin{bmatrix} \epsilon_1 \\ \epsilon_2 \\ \epsilon_3 \end{bmatrix} \quad (95)$$

$$\frac{\partial \boldsymbol{A^C}(t_i)}{\partial \boldsymbol{A^I}(t_i)} = -\mathbb{T}_I^C(t_i) \quad (96)$$

$$\frac{\partial \boldsymbol{A^I}(t_i)}{\partial \boldsymbol{T^I}(t_i)} = I_3 + \frac{\dot{T}(t)}{c}\left(\hat{T}\right) \quad (97)$$

with the landmark defined by the geometry at time t_j , independent by the spacecraft state at time t_i

$$\frac{\partial P(t_i - \tau_i)}{\partial \boldsymbol{R^I}(t_i)} = 0 \quad (98)$$

And similarly for time t_j

$$\frac{\partial \boldsymbol{z}}{\partial R(t_j)} = \frac{\partial \boldsymbol{z}}{\partial \boldsymbol{x'}} \frac{\partial \boldsymbol{x'}}{\partial \boldsymbol{x}} \frac{\partial \boldsymbol{x}}{\partial \boldsymbol{A^C}(t_i)} \frac{\partial \boldsymbol{A^C}(t_i)}{\partial \boldsymbol{A^I}(t_i)} \frac{\partial \boldsymbol{A^I}(t_i)}{\partial \boldsymbol{T^I}(t_i)} \frac{\partial \boldsymbol{T^I}(t_i)}{\partial \boldsymbol{R^I}(t_j)} \quad (99)$$

In this case the landmark has a dependence with the state at time t_j

$$\frac{\partial P(t_i - \tau_i)}{\partial \boldsymbol{R^I}(t_j)} \neq 0 \quad (100)$$

$$\frac{\partial \boldsymbol{T}^I(t_i)}{\partial \boldsymbol{R}_x^I(t_j)} = -\frac{\partial \boldsymbol{P}^I(t_i-\tau_i)}{\partial \boldsymbol{R}_x^I(t_j)} + \frac{\dot{\boldsymbol{P}}^I(t_i-\tau_i)}{c}\frac{\dot{\boldsymbol{T}}^I - \frac{\partial\left(-\boldsymbol{P}^I(t_i-\tau_i)\right)}{\partial \boldsymbol{R}_x^I(t_j)}}{1+\left(\frac{\dot{\boldsymbol{P}}^I\cdot\dot{\boldsymbol{T}}}{c}\right)} \quad (101)$$

$$\frac{\partial \boldsymbol{P}(t_i-\tau_i)}{\partial \boldsymbol{R}^I(t_j)} = \mathbb{T}_B^I(t_i-\tau_i)\mathbb{T}_B^I\left(t_j-\tau_j\right)^{-1} \quad (102)$$

where

$$\frac{\partial \boldsymbol{T}^I(t_j)}{\partial \boldsymbol{R}^I(t_j)} = 0 \quad (103)$$

$$\begin{bmatrix}\frac{\partial x}{\partial \boldsymbol{A}^C}\\ \frac{\partial y}{\partial \boldsymbol{A}^C}\end{bmatrix} = \begin{bmatrix} f/A_z^C(t_i) & 0 & -\frac{f}{\left(A_z^C(t_i)\right)^2}A_x^C(t_i) \\ 0 & f/A_z^C(t_i) & -\frac{f}{\left(A_z^C(t_i)\right)^2}A_y^C(t_i)\end{bmatrix} \quad (104)$$

$$\begin{bmatrix}\frac{\partial \Delta x}{\partial x}\\ \frac{\partial \Delta x}{\partial y}\\ \frac{\partial \Delta y}{\partial x}\\ \frac{\partial \Delta y}{\partial y}\end{bmatrix} = \begin{bmatrix} r^2+2x^2 & y & 2x \\ 2xy & x & 0 \\ 2xy & 0 & y \\ r^2+2y^2 & 2y & x\end{bmatrix}\begin{bmatrix}\epsilon_1\\ \epsilon_2\\ \epsilon_3\end{bmatrix} \quad (105)$$

with

$$\begin{bmatrix}x\\ y\end{bmatrix} = \frac{f}{A_3^C(t_i)}\begin{bmatrix}A_1^C(t_i)\\ A_2^C(t_i)\end{bmatrix} \quad (106)$$

and

$$C_{cam} = \begin{bmatrix} r^2+2x^2 & y & 2x \\ 2xy & x & 0 \\ 2xy & 0 & y \\ r^2+2y^2 & 2y & x\end{bmatrix} \quad (107)$$

$$\frac{\partial \boldsymbol{x'}}{\partial \boldsymbol{x}} = \begin{bmatrix}\frac{\partial x'}{\partial x} & \frac{\partial x'}{\partial y}\\ \frac{\partial y'}{\partial x} & \frac{\partial y'}{\partial y}\end{bmatrix} = \begin{bmatrix}\frac{\partial x'}{\partial x} & \frac{\partial x'}{\partial y}\\ \frac{\partial y'}{\partial x} & \frac{\partial y'}{\partial y}\end{bmatrix}_{\Delta\bar{x}=cost} + \begin{bmatrix}\frac{\partial \Delta x}{\partial x} & \frac{\partial \Delta x}{\partial y}\\ \frac{\partial \Delta y}{\partial x} & \frac{\partial \Delta y}{\partial y}\end{bmatrix} \quad (108)$$

$$\begin{bmatrix}\frac{\partial x'}{\partial x} & \frac{\partial x'}{\partial y}\\ \frac{\partial y'}{\partial x} & \frac{\partial y'}{\partial y}\end{bmatrix}_{\Delta\bar{x}=cost} = I_2 \quad (109)$$

$$\begin{bmatrix}\frac{\partial s}{\partial x'}\\ \frac{\partial l}{\partial y'}\end{bmatrix} = K \quad (110)$$

1.1.2 Target partials

1.1.2.1 Partials with respect to gravitational harmonics

The gravitational harmonics depends indirectly by the spacecraft state at time t_i and t_j. $\frac{\partial \boldsymbol{R^I}(t_j)}{\partial \boldsymbol{G.H.}}$ is provided by the integrator of the orbit determination software.

$$\frac{\partial \boldsymbol{z}}{\partial \boldsymbol{R^I}(t_j)} \frac{\partial \boldsymbol{R^I}(t_j)}{\partial \boldsymbol{G.H.}} \quad (111)$$

1.1.2.2 Partials with respect to planetary orientation parameters

$$z = z[\mathbb{T}_I^B(POP, t_i), \mathbb{T}_I^B\big(POP, t_j\big)] \quad (112)$$

$$\frac{\partial \boldsymbol{z}}{\partial \boldsymbol{POP}} = \frac{\partial \boldsymbol{z}}{\partial \mathbb{T}_I^B} \frac{\partial \mathbb{T}_I^B}{\partial \boldsymbol{POP}} = \frac{\partial \boldsymbol{z}}{\partial \mathbb{T}_I^B(t_i)} \frac{\partial \mathbb{T}_I^B(t_i)}{\partial \boldsymbol{POP}} + \frac{\partial \boldsymbol{z}}{\partial \mathbb{T}_I^B(t_j)} \frac{\partial \mathbb{T}_I^B(t_j)}{\partial \boldsymbol{POP}} \quad (113)$$

The derivatives of the rotational models depends on the rotational model selected in the experiment

$$\frac{\partial \mathbb{T}_I^B}{\partial \boldsymbol{POP}} \quad (114)$$

Derivatives of different rotational models can be found in (Meriggiola, 2012) and will not be listed here. But for completeness the other required relations are showed

$$\frac{\partial \boldsymbol{z}}{\partial \mathbb{T}_I^B(t_i)} = \frac{\partial \boldsymbol{z}}{\partial \boldsymbol{x'}} \frac{\partial \boldsymbol{x'}}{\partial \boldsymbol{x}} \frac{\partial \boldsymbol{x}}{\partial \boldsymbol{A^C}(t_i)} \frac{\partial \boldsymbol{A^C}(t_i)}{\partial \boldsymbol{A^I}(t_i)} \frac{\partial \boldsymbol{A^I}(t_i)}{\partial \boldsymbol{T^I}(t_i)} \frac{\partial \boldsymbol{T^I}(t_i)}{\partial \boldsymbol{P^I}(t_i - \tau_i)} \frac{\partial \boldsymbol{P^I}(t_i - \tau_i)}{\partial \mathbb{T}_I^B(t_i)} \quad (115)$$

with

$$\frac{\partial \boldsymbol{P^I}(t_i - \tau_i)}{\partial \mathbb{T}_I^B(t_i)} = \boldsymbol{P}^B\big(t_j - \tau_j\big) \quad (116)$$

$$\frac{\partial \boldsymbol{z}}{\partial \mathbb{T}_I^B(t_j)} = \frac{\partial \boldsymbol{z}}{\partial \boldsymbol{x'}} \frac{\partial \boldsymbol{x'}}{\partial \boldsymbol{x}} \frac{\partial \boldsymbol{x}}{\partial \boldsymbol{A^C}(t_i)} \frac{\partial \boldsymbol{A^C}(t_i)}{\partial \boldsymbol{A^I}(t_i)} \frac{\partial \boldsymbol{A^I}(t_i)}{\partial \boldsymbol{T^I}(t_i)} \frac{\partial \boldsymbol{T^I}(t_i)}{\partial \boldsymbol{P^I}(t_i - \tau_i)} \frac{\partial \boldsymbol{P^I}(t_i - \tau_i)}{\partial \mathbb{T}_I^B(t_j)} \quad (117)$$

and

$$\frac{\partial \boldsymbol{P^I}(t_i - \tau_i)}{\partial \mathbb{T}_I^B(t_i)} = \mathbb{T}_B^I(t_i - \tau_i) \boldsymbol{P}^B\big(t_j - \tau_j\big) \quad (118)$$

One serie of strong hypothesis for the proposed methodology at Mercury is the following (not valid in general):

a. Short period of image sampling Ts
b. smooth target surface, small field of view
c. Nadir pointing camera

The hypothesis a) result in a simplification of the partial derivatives with respect to planetary orientation parameters that are not expected to influence the estimation

$$\frac{\partial z}{\partial POP} \cong 0 \quad (119)$$

1.1.2.3 Partials with respect to topographic harmonics

This complication will be studied in another situation. E.g. Integration of crossover altimeter data with camera data.
Hypothesis c) result in an assumption that topographic harmonics do not influence the estimation

$$\frac{\partial z}{\partial T.H.} \cong 0 \quad (120)$$

Those hypothesis together with the intrinsic weakness of the camera signal in the line of sight direction (nadir), provide another result

$$\frac{\partial A_Z^C}{\partial q} \cong 0 \quad (121)$$

This result imply that altimetric informations at the instant of image acquisition could improve the total informative content.

1.1.3 Optical parameters partials

As described before, optical parameters are:

1. Focal length
2. Distortion coefficients
3. Components of K matrix
4. Camera center
5. Pointing angle errors

1.1.3.1 Partials of optical observables with respect to attitude measurement error

The attitude measurement errors are also expressed for the leg i and j separately.

$$\frac{\partial z}{\partial \delta\theta(t_i)} = \frac{\partial \boldsymbol{z}}{\partial \boldsymbol{x\prime}} \frac{\partial \boldsymbol{x\prime}}{\partial \boldsymbol{x}} \frac{\partial \boldsymbol{x}}{\partial \boldsymbol{A^C}(t_i)} \frac{\partial \boldsymbol{A^C}(t_i)}{\partial \delta\theta(t_i)} \quad (122)$$

$$\boldsymbol{A^C}(t_i) = \mathbb{T}_I^C(t_i)\boldsymbol{A^I}(t_i) \quad (123)$$

$$\mathbb{T}_I^C(t_i) = \mathbb{R}_y(el_i)\mathbb{R}_z(Az_i)\{I - [e_x]\}\{I - [\delta\theta_x]\}\mathbb{A}_I^{SC}(t_i) \quad (124)$$

$$\frac{\partial \boldsymbol{A^C}(t_i)}{\partial \delta\theta(t_i)} = \mathbb{R}_y(el_i)\mathbb{R}_z(Az_i)\{I - [e_x]\}[-\mathbb{A}_I^{SC}(t_i)\boldsymbol{A^I}(t_i)]_x \quad (125)$$

For leg j instead

$$\frac{\partial z}{\partial \delta\theta(t_j)} = \frac{\partial \boldsymbol{z}}{\partial \boldsymbol{x\prime}} \frac{\partial \boldsymbol{x\prime}}{\partial \boldsymbol{x}} \frac{\partial \boldsymbol{x}}{\partial \boldsymbol{A^C}(t_i)} \frac{\partial \boldsymbol{A^C}(t_i)}{\partial \boldsymbol{A^I}(t_i)} \frac{\partial \boldsymbol{A^I}(t_i)}{\partial \boldsymbol{T^C}(t_i)} \frac{\partial \boldsymbol{T^C}(t_i)}{\partial \boldsymbol{P^I}(t_i - \tau_i)} \frac{\partial \boldsymbol{P^I}(t_i - \tau_i)}{\partial \boldsymbol{T^I}(t_j)} \frac{\partial \boldsymbol{T^I}(t_j)}{\partial \boldsymbol{A^I}(t_j)} \frac{\partial \boldsymbol{A^I}(t_j)}{\partial \delta\theta(t_j)} \quad (126)$$

where

$$\frac{\partial \boldsymbol{T^C}(t_i)}{\partial \boldsymbol{P^I}(t_i - \tau_i)} = -I_3 \quad (127)$$

$$\frac{\partial \boldsymbol{P}^I(t_i-\tau_i)}{\partial \boldsymbol{T}^I(t_j)} = -\mathbb{T}_B^I(t_i-\tau_i)\mathbb{T}_B^I\left(t_j-\tau_j\right)^{-1} \quad (128)$$

$$\frac{\partial T^I(t_j)}{\partial \boldsymbol{A}^I(t_j)} = \left[\frac{\partial \boldsymbol{A}^I(t_j)}{\partial T^I(t_j)}\right]^{-1} \quad (129)$$

$$\frac{\partial \boldsymbol{A}^I(t_j)}{\partial \boldsymbol{T}^I(t_j)} = I_3 + \frac{\dot{T}(t)}{c}\left(\hat{T}\cdot I_3\right) \quad (130)$$

$$\boldsymbol{A}^I\left(t_j\right) = \mathbb{T}_C^I\left(t_j\right)\boldsymbol{A}^C\left(t_j\right) \quad (131)$$

and

$$\frac{\partial \boldsymbol{A}^I(t_j)}{\partial \delta\theta(t_j)} == -\left(\mathbb{A}_I^{SC}\left(t_j\right)\right)^T\{I+[\epsilon_X]\}\left[\mathbb{R}_z^T\left(Az_j\right)\mathbb{R}_y^T\left(el_j\right)\boldsymbol{A}^C\left(t_j\right)\right]_x \quad (132)$$

where $\theta\delta(t_j)$ has been neglected

And finally

$$\frac{\partial z}{\partial \delta\theta} = \frac{\partial z}{\partial \delta\theta(t_i)} + \frac{\partial z}{\partial \delta\theta(t_j)} \quad (133)$$

1.1.4 Optical bias parameters partials

Optical bias parameters are used for systematic errors.

1.1.4.1 Systematic camera misalignment

$$\frac{\partial z}{\partial \epsilon(t_i)} = \frac{\partial \boldsymbol{z}}{\partial \boldsymbol{x\prime}}\frac{\partial \boldsymbol{x\prime}}{\partial \boldsymbol{x}}\frac{\partial \boldsymbol{x}}{\partial \boldsymbol{A^C}(t_i)}\frac{\partial \boldsymbol{A^C}(t_i)}{\partial \epsilon(t_i)} \quad (134)$$

$$\boldsymbol{A}^C(t_i) = \mathbb{T}_I^C(t_i)\boldsymbol{A}^I(t_i) \quad (135)$$

$$\mathbb{T}_I^C(t_i) = \mathbb{R}_y(el_i)\mathbb{R}_z(Az_i)\{I-[e_x]\}\{I-[\delta\theta_x(t_i)]\}\mathbb{A}_I^{SC}(t_i) \quad (136)$$

$$\frac{\partial \boldsymbol{A^C}(t_i)}{\partial \epsilon(t_i)} = \mathbb{R}_y(el_i)\mathbb{R}_z(Az_i)[-\{I-[\delta\theta_x(t_i)]\}\mathbb{A}_I^{SC}(t_i)\boldsymbol{A^I}(t_i)]_x \quad (137)$$

for leg j

$$\frac{\partial z}{\partial \epsilon(t_j)} = \frac{\partial \boldsymbol{z}}{\partial \boldsymbol{x\prime}}\frac{\partial \boldsymbol{x\prime}}{\partial \boldsymbol{x}}\frac{\partial \boldsymbol{x}}{\partial \boldsymbol{A^C}(t_i)}\frac{\partial \boldsymbol{A^C}(t_i)}{\partial \boldsymbol{A^I}(t_i)}\frac{\partial \boldsymbol{A^I}(t_i)}{\partial \boldsymbol{T^I}(t_i)}\frac{\partial \boldsymbol{T^I}(t_i)}{\partial \boldsymbol{P^I}(t_i-\tau_i)}\frac{\partial \boldsymbol{P^I}(t_i-\tau_i)}{\partial \boldsymbol{T^I}(t_j)}\frac{\partial \boldsymbol{T^I}(t_j)}{\partial \boldsymbol{A^I}(t_j)}\frac{\partial \boldsymbol{A^I}(t_j)}{\partial \epsilon(t_j)} \quad (138)$$

$$\mathbb{T}_I^C\left(t_j\right) = \mathbb{R}_y\left(el_j\right)\mathbb{R}_z\left(Az_j\right)\{I-[e_x]\}\left\{I-\left[\delta\theta_x(t_j)\right]\right\}\mathbb{A}_I^{SC}(t_j) \quad (139)$$

$$\mathbb{T}_C^I\left(t_j\right) = \left(\mathbb{A}_I^{SC}\left(t_j\right)\right)^T\left\{I+\left[\delta\theta(t_j)_x\right]\right\}\{I+[e_x]\}\,\mathbb{R}_z^T\left(Az_j\right)\mathbb{R}_y^T\left(el_j\right) \quad (140)$$

$$\frac{\partial \boldsymbol{A}^I(t_j)}{\partial \epsilon(t_j)} = -\left(\mathbb{A}_I^{SC}(t_j)\right)^T \{I + [\delta\theta(t_j)_X]\} \left[\mathbb{R}_z^T(Az_j)\mathbb{R}_y^T(el_j)\boldsymbol{A}^C(t_j)\right]_x \quad (141)$$

And finally

$$\frac{\partial z}{\partial \epsilon} = \frac{\partial z}{\partial \epsilon(t_i)} + \frac{\partial z}{\partial \epsilon(t_j)} \quad (142)$$

8.3 Target shape model effects on optical observables

One of the major hypothesis of this study is to consider the intersection computation with an ellipsoid shape without adding considers of the error due to shape mismodeling. It is required to prove this hypothesis will not yield a wrong conclusion.
In the following it is evaluated the error committed using a sphere, an ellipse or ellipsoid.
The intersection computation can be done at different level of approximation; modeling the planet as a sphere, an ellipsoid or a complex surface with a Digital Elevation Model associated with it.
To correctly define what can be used and if the surface uncertainty should be considered in the estimation it is necessary to evaluate the variation due to bulging and surface "rugosity" (the presence of mountains, craters and cracks).

Table 7 Solar System mountains range

Body	Mountain name	Height
Mercury	Caloris Montes	< 3 km
Moon	Mons Huygens	5.5 km
Mars	Olympus Mons	21.9 km
Vesta	Rheasilvia central peak	22 km
Iapetus	Equatorial ridge	20 km
Mimas	Herschel central peak	7 km

A pixel offset due to variations from a theoretical ellipsoid model caused by a presence of a mountain has been modeled in a simplified model considering different ground-track resolution (height and focal length dependent) and change of ground altitude due by the presence of a mountain.
Following the geometry in the following figure Figure 41 Geometry of a surface height error on optical observables the relations are:

$$H_T = H + \Delta H \quad (143)$$

$$l = \sqrt{\overline{co}^2 + H_T^2} \quad (144)$$

$$\gamma = \operatorname{acos}\left(\frac{\overline{co}}{l}\right) \quad (145)$$

$$d = \frac{\Delta H}{\sin(\gamma)} \quad (146)$$

$$B = 2c + o \quad (147)$$

$$G = \sqrt{H_T^2 + c^2} \quad (148)$$

$$\theta = \text{acos}\left(\frac{c}{G}\right) \quad (149)$$

$$\beta = \pi - \theta - \gamma \quad (150)$$

$$m = l - d \quad (151)$$

$$\alpha = \text{asin}\left(o\frac{sin(\beta)}{m}\right) \quad (152)$$

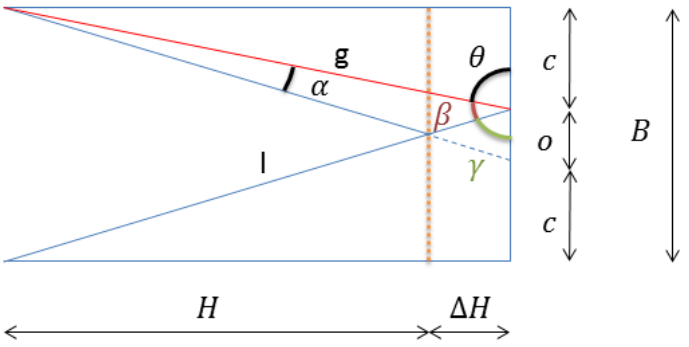

Figure 41 Geometry of a surface height error on optical observables

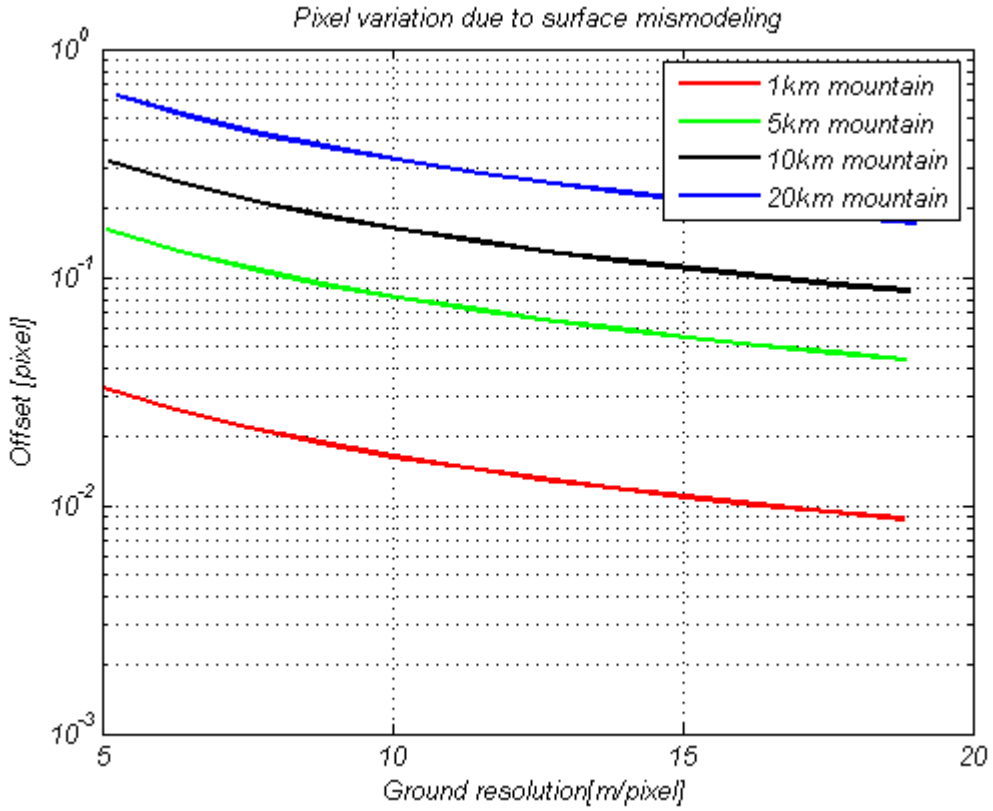

Figure 42 Pixel offset due to mountains mismodeling

it can be evinced that this effect is consistent, if considering Pattern matching error under 0.1 pixel also for moons like Iapetus (equatorial ridge) and a DEM model should be considered.
In the following a DEM model will be not considered for our analysis at Mercury, but it should be evaluated when applied to a different mission scenario.

It is also evident that an ellipsoid model needs to be used because the differences between a spherical and elliptical model could generate height altitudes of tens to hundreds of km.

Table 8 Solar system bodies mean radius versus flattening

Body	Mean radius	Flattening	Radius difference
Mercury	2439.7 km	~0	2.2 km
Iapetus	735.6 km	0.047	35 km

8.4 Partials validation

Analytical partials were validated by means of a comparison to numerical partials.

8.4.1 Validation of spacecraft state partials

State partials are validated comparing the first order finite differenced partials, with respect to the analytical ones with respect to the state at epoch. This comparison is done applying an offset to one single state coordinate at the time

$$\frac{\partial \boldsymbol{z}}{\partial \boldsymbol{S}(t_{0j})} = \frac{z\left(\Delta S(t_{0j}) + S(t_{0j})\right) - z\left(S(t_{0j})\right)}{\Delta S(t_{0j})} \quad (153)$$

8.4.2 Validation of manoeuver partials

Similarly to state partials, also maneuver partials can be compared to finite difference partials.The requirement is that the observable is generated by an image pair surrounding the manoeuver epoch, or $t_1 < t_{man} < t_2$.

The first order finite difference partials are

$$\frac{\Delta z}{\Delta V_M} = \frac{z_T - z(V_{Man} + \delta V_{Man})}{\delta V_M} \quad (154)$$

computed separately for each manoeuver direction.

8.4.3 Validation of pointing errors partials

The validation of the pointing error partials was done computing an expected pixel variation due to a pointing offset and verifying the same result in the partials for each leg.

Rotation around the axes orthogonal to the focal axis

$$\frac{pdx}{f} \sim \delta\theta_M, \delta\theta_N \quad (155)$$

Rotation around the focal axis

$$\frac{1024\sqrt{2}\,dx}{f} \sim \delta\theta_L \quad (156)$$

8.5 Sensibility Analysis

Sensibility analysis can be used for a preliminary study. It provides a tool to evaluate the impact of each parameter uncertainty in the measurements, an eventual conclusion is then to decide whether to consider or not a subtle parameter in the estimation filter (consider parameters are those quantities that are not estimated explicitly in the orbit determination).
A sensibility analysis has been done for some parameters not to be estimated but whose uncertainty may have to be considered in the estimation filter.
Observables variations caused by a focal length error:

$$\Delta z = \frac{\partial z}{\partial \mathrm{f}} \Delta \mathrm{f} \quad (157)$$

Observables variations caused by a systematic pointing error:

$$\Delta z = \frac{\partial z}{\partial \epsilon} \epsilon \quad (158)$$

Observables variations caused by a measurement pointing error:

$$\Delta z = \frac{\partial z}{\partial \theta(t)} \Delta \theta \quad (159)$$

Observables variations caused by planetary orientation parameters modeling errors:

$$\Delta z = \frac{\partial z}{\partial POP} \Delta POP \quad (160)$$

From these partials the following conclusions were obtained:

- from a sensing instrument with the characteristics of HRIC the focal length shall be calibrated to values better than 1e-3% for a pixel scaling effect (away from the focal axis) less than the pattern matching ideal value of 0.01 pixels, while for an instrument with the same parameters of ISS the value should be slightly more relaxed, to 2e-3% (equivalent to the order of 10um)
- Sequential optical measurement are sampled daily, this construction gives an insensitivity to perturbations by low frequency high amplitude POP. Furthermore the methodology is applied at high latitude, making insensitive this observable to oscillations like chandler wobble, (more effective evidently at low latitude).
- When an attitude pointing error of 2.5'' is applied to a camera with HIRC characteristics, the expected pixel shift on line and sample directions if of about 1 pixel, for a single leg, while in the focal axis direction is of 1/100 of a pixel. Is important to notice that the contribution due to both legs is of similar intensity. This effect is maximum if the error to sample and line axis rotations directions in one leg is of opposite sign with respect to the error in the other leg, while almost annihilate if the errors are equal and of the same sign the effect. For an attitude bias instead, for the very same reason, it becomes insensitive, requiring an absolute calibration (eg. using stars) for the reduction of this bias to a negligible level (eg. under the pattern matching level).

9 Results

9.1 Simulation environment

A simulation environment has been set up, based on MONTE, an Orbit Determination software of the Jet Propulsion Laboratory, available at the University of Bologna for research purposes.
This program was upgraded with the optical observables defined in the former chapter, written as a plug-in python class.
The routine comprises a simulation block that generates a true trajectory, followed by the computation of a spacecraft synthetic attitude file, with the constraint of a Nadir pointing camera. Successively, with customizable input constrains an image acquisition schedule is generated as a list of pairs of shutter times for the camera and provided for the last routine that generates the novel optical observables. In parallel also Doppler measurements are generated with a routine that simulate a typical radiometric tracking schedule.
To reproduce real observed measurements, white random noise is added to Doppler and to the optical observables.
The same apply for the attitude file, that as in real navigation, is not exact but is the result of another estimation process by the AOCS, therefore afflicted by possible systematic errors and time varying pointing errors.
The next step is the estimation process. Offsets can be added to the true values of each solve-for parameter, and a trajectory is evaluated with this biased setup. Doppler and Optical measurements are then computed with this new setup, with their associated partial derivatives, using the attitude resulted from the simulation block. Finally a filter process all the data and produce an estimation of the solve-for parameters, reiterating the estimation process typically from 2 to 5 times.

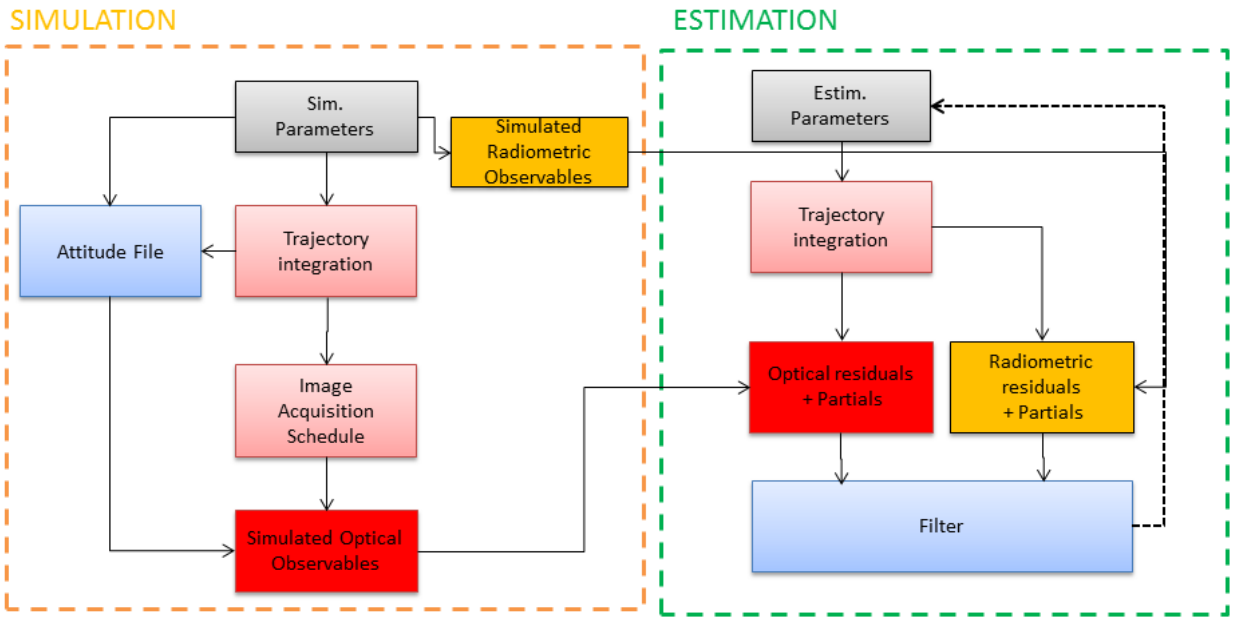

Figure 43 Simulation and Estimation process

9.1.1 Accelerometers

To reach state-of-the-art accuracy in orbit determination, modern space crafts uses accelerometers. MPO uses ISA, a tri-axial accelerometer, which purpose is to avoid modeling of non-gravitational accelerations with approximate formulations in orbit determination. In fact, for the case of MPO, the values of non-gravitational accelerations, are measured directly by ISA and the values can be applied directly on the dynamical models during the orbit determination process. This technique produces a so called "a posteriori drag-free" probe. For the following simulations a value of 10e-9 m/s^2 of residual non-gravitational acceleration was used (Iafolla, 2010).

9.1.2 Maneuvers

For Cassini the manoeuvres planned for Orbit Trim manoeuvres, i.e. manoeuvers for maintaining the reference mission orbit, are of the order of [10 m/s - 0.01 m/s] (Williams, 2008).

For the MPO Orbiter Spacecraft, there are four thrusters, mounted on the radiator face in the –Y cross-track direction, inclined inwards of 30° with respect to the normal of the radiator plane. This configuration exploit the difficulty of changing the orbital plane. But when applying a reaction wheels desaturation manoeuvres, the unperfected alignment, generate a trajectory change.
In this geometry, possible values due to unaligned thrusters are (internal com.):

- 0 mm/s along track
- < 17 mm/s radial (nadir)
- 42 mm/s out of plane

These manoeuvers are planned twice a day and strategically one of the two is scheduled inside an X-Band tracking pass (MPO can achieve this because of its steerable antenna). There are no planned manoeuvers during Ka-Band tracking to not degrade scientific results. The other manoeuver remain uncovered by tracking.

9.2 Simulated Polar orbiter: Cassini

This simulation was conducted describing a polar orbiter around a Moon with the characteristics of mass and size of Titan, using Cassini parameters as a test-bed, in particular for the ISS NAC camera intrinsic parameters.

For the orbit the following Keplerian parameters were selected:

- semi-major axis: 4384.21 km
- eccentricity: 1
- Orbit inclination: 89.9°
- RAAN: 0.1°
- Argument of Periapsis: 0.1°
- Orbital period: 5h

The measurements were a set of 76 points for Two-way X-Band Doppler Observables, while 10 optical data points in sample and line and a pattern matching error of 0.01 pixel
The estimation apriori value offset was of

- Position error : 0.1*km
- Velocity error : 1e-6 *km/s

Other characteristics:

- FOV : 11 km
- Ground Resolution : 92.1 pixel/km, 10.8 m/pixel

The following camera intrinsic parameter were used

- Focal length : 2000 mm
- N Pixel : 1024x1024
- Pixel dimension : 12um

An analysis was conducted at varying SEP angles, influencing the expected X-Band Doppler noise

Table 9 Doppler Noise at varying SEP for a simulated mission

SEP	Two-Way X band Noise @60s
30°	2.8 mHz
180°	0.56 mHz

The first conclusion was that there was effectively no improvement in the final solution adding optical observables in the aforementioned solar conjunction simulation environment. But two particular conditions were then analysed:

- Doppler Weak geometry (Earth-Probe direction normal to orbital plane)
- Solution variation through time, plotting the partial solution given step-by-step processing sequentially each observable, called by the navigation Team an History Plot

Comparing the two SEP conditions in a situation of weak geometry the optical signal became informative.
The following plot represent the final filter solution in a condition of weakness of Doppler observables (RAAN changed to have a nearly perpendicular orbit with respect to S/C-Earth direction) and in conditions of high SEP (30 degrees) is highly influenced by optical data.

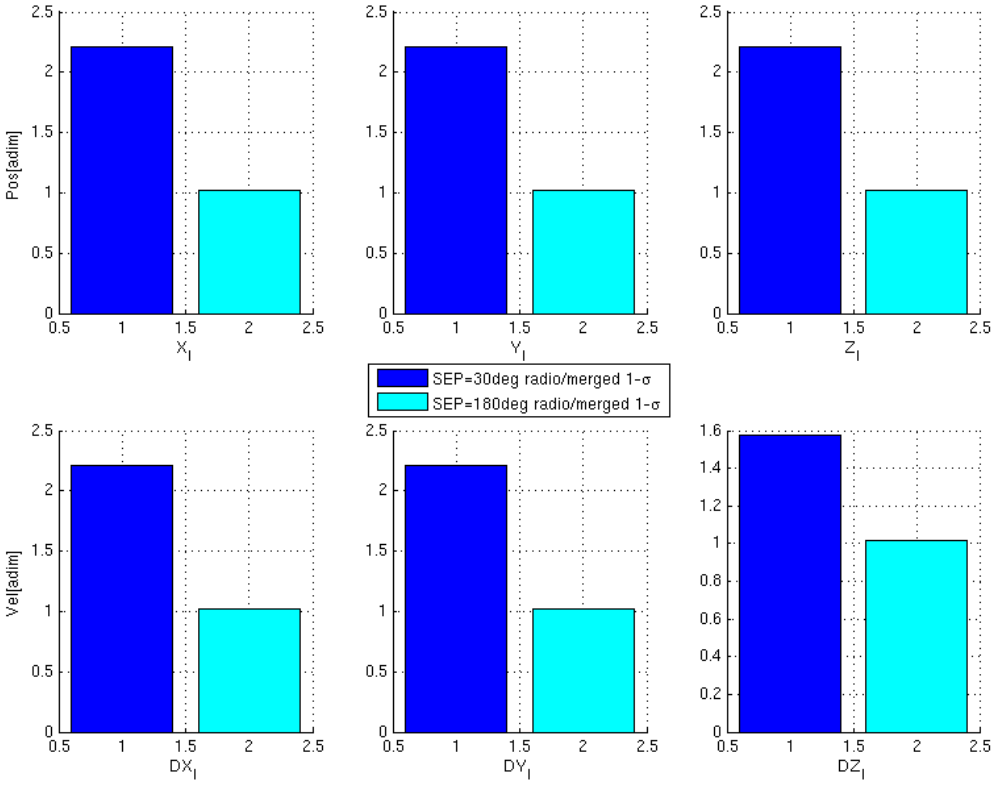

Figure 44 Consider solution improvement in a condition of weak geometry and SEP variations

The following History Plot represent a condition with no improvement in the final solution.
After processing all data with SEP of 180° shows that in an intermediate period the optical observables supported Doppler, until the Doppler informative content is sufficient to converge to the same result. This is what is expected in a weak condition; if the arc of observation is longer, the weakness problem is solved.
The dotted vertical yellow lines indicates the sampling of an optical image, the second image permit to generate a first optical observable that contributes to reduce the uncertainty of the state at epoch as a proof of the information content carried by the optical images.

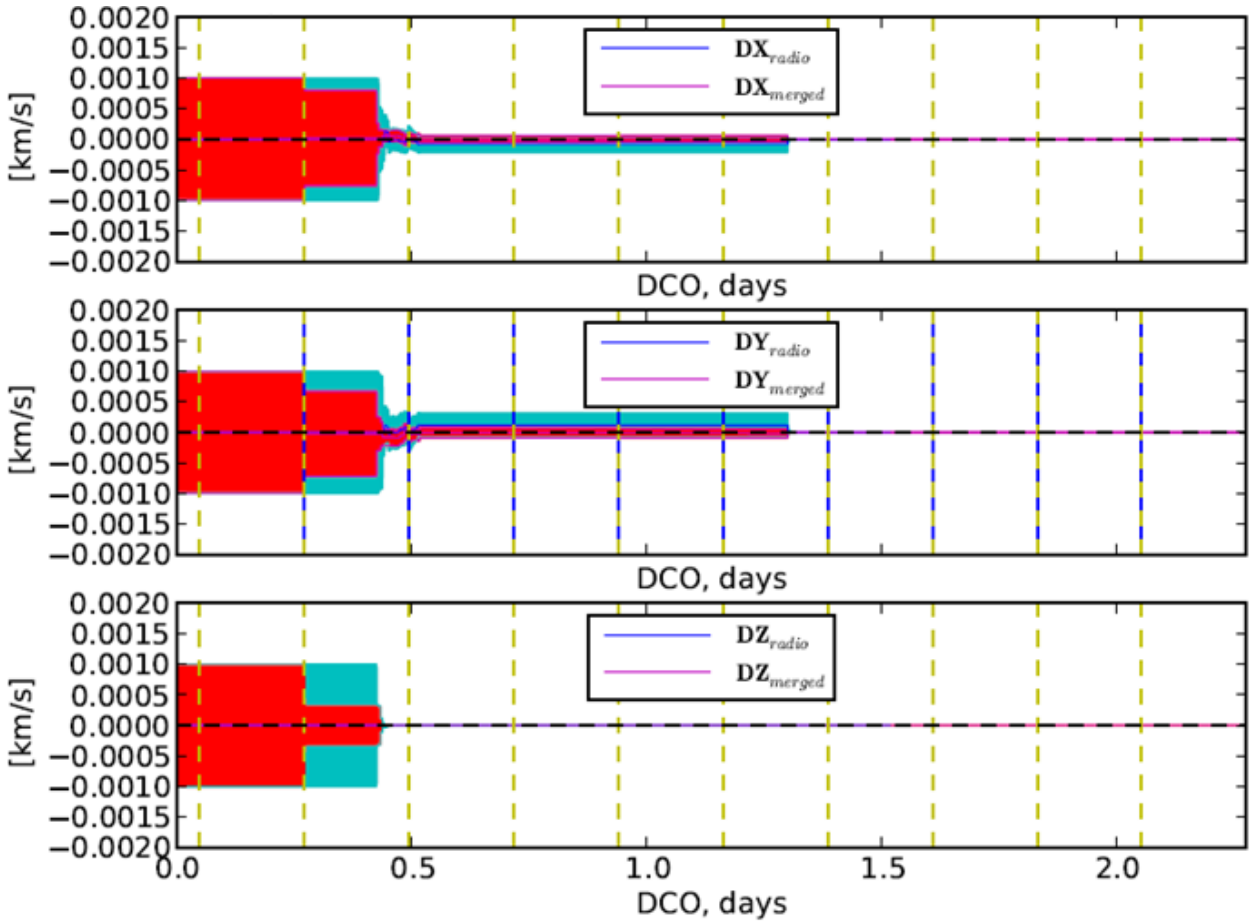

Figure 45 History Plot: Probe Velocity Estimation. Vertical dotted Yellow lines indicates the acquisition of an image

Moreover a set of manoeuvres were estimated using the following parameters

State offset:

- $\Delta Position$: 0.1 km,
- $\Delta Velocity$: 1e-5 km/s

State apriori uncertainty

- σ_{Pos} =1 km
- σ_{Vel} =1e-3 km/s

Orbit Trim Maneuver Values

- DeltaMass = -0.4 kg
- Δman = [1e-4 m/s 1e-5 m/s 1e-4 m/s]
- σ_{Man} = [1e-1 m/s 1e-2 m/s 1e-1 m/s]

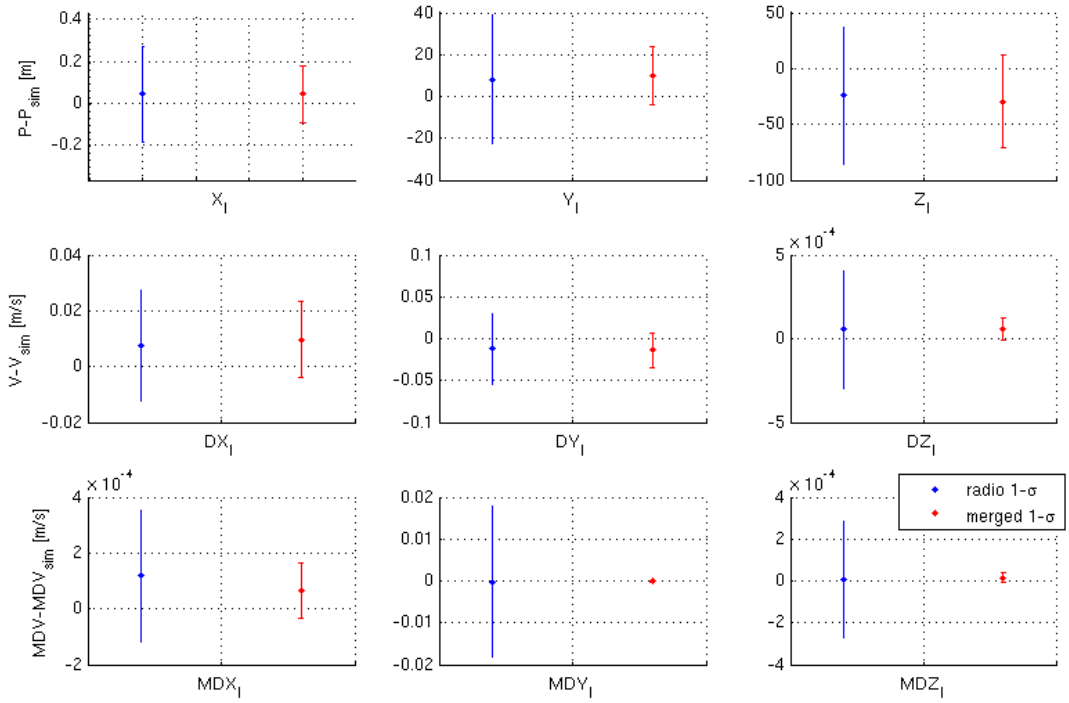

Figure 46 Orbiter State and Maneuvers estimation

In this plot is evinced that the informative content of impulsive manoeuvres carried by optical observables is high and can be in theory estimated.

9.3 Simulated Polar orbiter: MPO

In this alternative scenario, an Orbiter has been defined on Mercury with the characteristic orbit expected for MPO at the start of the operative phase.
For the orbit the following Keplerian parameters were selected:

- semi-major axis: 3396.7645 km
- eccentricity: 0.167
- Orbit inclination: 79.9°
- RAAN: 260°
- Argument of Periapsis: 0.1°
- Orbital period: 2.3 h

An impulsive manoeuver for Orbit Trim of

$$\Delta V_{Man}=[7.0 \text{ mm/s}, 5.0\text{e-}4 \text{ mm/s}, 3.0\text{e-}3 \text{ mm/s}]$$

A set of 5 days coverage at an integration time of 1000 s for Two-way X-Band Doppler Observables with noise of 0.16 mHz @1000 s and for Ka-Band at 1.1mHz@1000s while 3 optical data points in sample and line and a pattern matching error of 0.01 pixel, was simulated.

The following camera intrinsic parameters were used (From HRIC)

- Focal length : 800 mm
- N Pixel : 2048x2048
- Pixel dimension : 10um

9.3.1 Convergence analysis

In this setup X-Band and Ka-band Doppler are augmented with optical observables with an almost zero PM error (an ideal 1e-4 pattern matching pixel noise) and with no attitude measurement errors. Only three optical observables are used and the result provides an improvement in the estimation in terms of delta solution and consider sigma.
The optical observables are scheduled sequentially.

State apriori offset error:

- $\Delta Position$: 1 m,
- $\Delta Velocity$: 0.1 mm/s

State apriori uncertainty

- σ_{Pos} =1 km
- σ_{Vel} =1 m/s

Orbit Trim Maneuver Values

- DeltaMass = 0 kg
- Δman = [0 mm/s 0 mm/s 0 mm/s]
- σ_{Man} = [5 mm/s 5 mm/s 5 mm/s]

Table 10 convergence solution: state bias, one manoeuver, no AME, no PM error

Doppler

Parameter	BaseNom	Value	/Sigma	Apsig	Sigma	/Apsig	totDelta	/Apsig	Unit
State/MPO/Mercury/EME2000/X		-1.3161243e+02	-1.3161340e+02	3.9e+06	1.0000000e+00	3.3704165e-05	0.000	-9.61409e-04	0.001 km
State/MPO/Mercury/EME2000/Y		1.8917807e+03	1.8917797e+03	2.3e+08	1.0000000e+00	8.3848702e-06	0.000	-9.90224e-04	0.001 km
State/MPO/Mercury/EME2000/Z		-2.4212404e+03	-2.4212414e+03	5.8e+08	1.0000000e+00	4.1641308e-06	0.000	-9.94976e-04	0.001 km
State/MPO/Mercury/EME2000/DX		-6.5781160e-01	-6.5781169e-01	6.1e+07	1.0000000e-03	1.0864264e-08	0.000	-8.76950e-08	0.000 km/sec
State/MPO/Mercury/EME2000/DY		-1.9042685e+00	-1.9042686e+00	2.0e+08	1.0000000e-03	9.4749552e-09	0.000	-8.91541e-08	0.000 km/sec
State/MPO/Mercury/EME2000/DZ		-1.9448474e+00	-1.9448475e+00	1.6e+08	1.0000000e-03	1.2359822e-08	0.000	-1.14313e-07	0.000 km/sec
Impulse Burn/MPO/OTM0000X/DX		1.0000000e-06	1.0010075e-06	9.5e+02	5.0000000e-06	1.0486687e-09	0.000	1.00750e-09	0.000 km/sec
Impulse Burn/MPO/OTM0000X/DY		1.0000000e-06	1.0003964e-06	2.1e+03	5.0000000e-06	4.7883052e-10	0.000	3.96356e-10	0.000 km/sec
Impulse Burn/MPO/OTM0000X/DZ		1.0000000e-06	9.9972388e-07	4.7e+03	5.0000000e-06	2.1215288e-10	0.000	-2.76119e-10	0.000 km/sec

Merged

Parameter	BaseNom	Value	/Sigma	Apsig	Sigma	/Apsig	totDelta	/Apsig	Unit
State/MPO/Mercury/EME2000/X		-1.3161243e+02	-1.3161343e+02	4.5e+08	1.0000000e+00	2.9168941e-07	0.000	-9.99436e-04	0.001 km
State/MPO/Mercury/EME2000/Y		1.8917807e+03	1.8917797e+03	2.6e+09	1.0000000e+00	7.2801379e-07	0.000	-1.00014e-03	0.001 km
State/MPO/Mercury/EME2000/Z		-2.4212404e+03	-2.4212414e+03	3.2e+09	1.0000000e+00	7.6096314e-07	0.000	-9.98855e-04	0.001 km
State/MPO/Mercury/EME2000/DX		-6.5781160e-01	-6.5781171e-01	3.0e+09	1.0000000e-03	2.2100666e-10	0.000	-1.05490e-07	0.000 km/sec
State/MPO/Mercury/EME2000/DY		-1.9042685e+00	-1.9042686e+00	3.4e+09	1.0000000e-03	5.5295382e-10	0.000	-9.95065e-08	0.000 km/sec
State/MPO/Mercury/EME2000/DZ		-1.9448474e+00	-1.9448475e+00	2.8e+09	1.0000000e-03	6.8995510e-10	0.000	-9.98347e-08	0.000 km/sec
Impulse Burn/MPO/OTM0000X/DX		1.0000000e-06	9.9999907e-07	5.3e+05	5.0000000e-06	1.8996901e-12	0.000	-9.30313e-13	0.000 km/sec
Impulse Burn/MPO/OTM0000X/DY		1.0000000e-06	9.9998840e-07	5.1e+04	5.0000000e-06	1.9546147e-11	0.000	-1.15981e-11	0.000 km/sec
Impulse Burn/MPO/OTM0000X/DZ		1.0000000e-06	1.0000046e-06	1.4e+05	5.0000000e-06	7.2330170e-12	0.000	4.56434e-12	0.000 km/sec

The merged solution is better in terms of consider sigma; it's also evident by the observation of the delta correction on the OTM manoeuver parameters that a more stable solution has been achieved, probably provided by a de-correlation to the state velocity at epoch given by the information carried by optical observables.

In this next setup also a maneuver offset error is added. It's still possible to observe an improvement in the estimation in terms of delta solution and consider sigma of the Merged solution with respect to the Doppler one.
The optical observables are scheduled with a sequential schedule each 8 hours.

State apriori offset error:

- $\Delta Position$: 1 m,
- $\Delta Velocity$: 0.1 mm/s

State apriori uncertainty

- σ_{Pos} =1 km
- σ_{Vel} =1 m/s

Orbit Trim Maneuver Values

- DeltaMass = 0 kg
- Δman = [0.1 mm/s 0.1 mm/s 0.1 mm/s]
- σ_{Man} = [5 mm/s 5 mm/s 5 mm/s]

Table 11 convergence solution: state bias, one maneuver, maneuver bias, no AME, no PM error

Doppler										
Parameter	BaseNom	Value	/Sigma	Apsig	Sigma	/Apsig	totDelta	/Apsig	Unit	
State/MPO/Mercury/EME2000/X		-1.3161243e+02	-1.3161339e+02	3.9e+06	1.0000000e+00	3.3704163e-05	0.000	-9.57153e-04	0.001	km
State/MPO/Mercury/EME2000/Y		1.8917807e+03	1.8917797e+03	2.3e+08	1.0000000e+00	8.3848698e-06	0.000	-9.88627e-04	0.001	km
State/MPO/Mercury/EME2000/Z		-2.4212404e+03	-2.4212414e+03	5.8e+08	1.0000000e+00	4.1641307e-06	0.000	-9.94272e-04	0.001	km
State/MPO/Mercury/EME2000/DX		-6.5781160e-01	-6.5781169e-01	6.1e+07	1.0000000e-03	1.0864264e-08	0.000	-8.60758e-08	0.000	km/sec
State/MPO/Mercury/EME2000/DY		-1.9042685e+00	-1.9042686e+00	2.0e+08	1.0000000e-03	9.4749548e-09	0.000	-8.72326e-08	0.000	km/sec
State/MPO/Mercury/EME2000/DZ		-1.9448474e+00	-1.9448475e+00	1.6e+08	1.0000000e-03	1.2359822e-08	0.000	-1.16435e-07	0.000	km/sec
Impulse Burn/MPO/OTM0000X/DX		1.1000000e-06	1.0004074e-06	9.5e+02	5.0000000e-06	1.0486687e-09	0.000	-9.95926e-08	0.020	km/sec
Impulse Burn/MPO/OTM0000X/DY		1.1000000e-06	1.0000003e-06	2.1e+03	5.0000000e-06	4.7883050e-10	0.000	-9.99997e-08	0.020	km/sec
Impulse Burn/MPO/OTM0000X/DZ		1.1000000e-06	9.9992249e-07	4.7e+03	5.0000000e-06	2.1215288e-10	0.000	-1.00078e-07	0.020	km/sec
Merged										
State/MPO/Mercury/EME2000/X		-1.3161243e+02	-1.3161344e+02	4.5e+08	1.0000000e+00	2.9168940e-07	0.000	-1.00022e-03	0.001	km
State/MPO/Mercury/EME2000/Y		1.8917807e+03	1.8917797e+03	2.6e+09	1.0000000e+00	7.2801382e-07	0.000	-1.00189e-03	0.001	km
State/MPO/Mercury/EME2000/Z		-2.4212404e+03	-2.4212414e+03	3.2e+09	1.0000000e+00	7.6096313e-07	0.000	-1.00105e-03	0.001	km
State/MPO/Mercury/EME2000/DX		-6.5781160e-01	-6.5781171e-01	3.0e+09	1.0000000e-03	2.2100667e-10	0.000	-1.03384e-07	0.000	km/sec
State/MPO/Mercury/EME2000/DY		-1.9042685e+00	-1.9042686e+00	3.4e+09	1.0000000e-03	5.5295382e-10	0.000	-1.00990e-07	0.000	km/sec
State/MPO/Mercury/EME2000/DZ		-1.9448474e+00	-1.9448475e+00	2.8e+09	1.0000000e-03	6.8995513e-10	0.000	-9.82859e-08	0.000	km/sec
Impulse Burn/MPO/OTM0000X/DX		1.1000000e-06	1.0000037e-06	5.3e+05	5.0000000e-06	1.8996901e-12	0.000	-9.99963e-08	0.020	km/sec
Impulse Burn/MPO/OTM0000X/DY		1.1000000e-06	1.0000398e-06	5.1e+04	5.0000000e-06	1.9546147e-11	0.000	-9.99602e-08	0.020	km/sec
Impulse Burn/MPO/OTM0000X/DZ		1.1000000e-06	9.9998512e-07	1.4e+05	5.0000000e-06	7.2330171e-12	0.000	-1.00015e-07	0.020	km/sec

The same result is obtained, with a slight improvement in the consider sigma and a better delta solution.

In the following run an ideal pattern matching error of 0.01 pixel has been considered, while the weight conservatively to 0.02 pixels.

Table 12 convergence solution: state bias, one maneuver, maneuver bias, no AME, PM error

Doppler										
Parameter	BaseNom	Value	/Sigma	Apsig	Sigma	/Apsig	totDelta	/Apsig	Unit	
State/MPO/Mercury/EME2000/X		-1.3161243e+02	-1.3161339e+02	3.9e+06	1.0000000e+00	3.3704163e-05	0.000	-9.57153e-04	0.001	km
State/MPO/Mercury/EME2000/Y		1.8917807e+03	1.8917797e+03	2.3e+08	1.0000000e+00	8.3848698e-06	0.000	-9.88627e-04	0.001	km
State/MPO/Mercury/EME2000/Z		-2.4212404e+03	-2.4212414e+03	5.8e+08	1.0000000e+00	4.1641307e-06	0.000	-9.94272e-04	0.001	km
State/MPO/Mercury/EME2000/DX		-6.5781160e-01	-6.5781169e-01	6.1e+07	1.0000000e-03	1.0864264e-08	0.000	-8.60758e-08	0.000	km/sec
State/MPO/Mercury/EME2000/DY		-1.9042685e+00	-1.9042686e+00	2.0e+08	1.0000000e-03	9.4749548e-09	0.000	-8.72326e-08	0.000	km/sec
State/MPO/Mercury/EME2000/DZ		-1.9448474e+00	-1.9448475e+00	1.6e+08	1.0000000e-03	1.2359822e-08	0.000	-1.16435e-07	0.000	km/sec
Impulse Burn/MPO/OTM0000X/DX		1.1000000e-06	1.0004074e-06	9.5e+02	5.0000000e-06	1.0486687e-09	0.000	-9.95926e-08	0.020	km/sec
Impulse Burn/MPO/OTM0000X/DY		1.1000000e-06	1.0000003e-06	2.1e+03	5.0000000e-06	4.7883050e-10	0.000	-9.99997e-08	0.020	km/sec
Impulse Burn/MPO/OTM0000X/DZ		1.1000000e-06	9.9992249e-07	4.7e+03	5.0000000e-06	2.1215288e-10	0.000	-1.00078e-07	0.020	km/sec
Merged										
State/MPO/Mercury/EME2000/X		-1.3161243e+02	-1.3161344e+02	3.9e+06	1.0000000e+00	3.3699802e-05	0.000	-1.00812e-03	0.001	km
State/MPO/Mercury/EME2000/Y		1.8917807e+03	1.8917797e+03	2.3e+08	1.0000000e+00	8.3838486e-06	0.000	-1.00005e-03	0.001	km
State/MPO/Mercury/EME2000/Z		-2.4212404e+03	-2.4212414e+03	5.8e+08	1.0000000e+00	4.1636580e-06	0.000	-9.99285e-04	0.001	km
State/MPO/Mercury/EME2000/DX		-6.5781160e-01	-6.5781170e-01	6.1e+07	1.0000000e-03	1.0862866e-08	0.000	-1.02516e-07	0.000	km/sec

State/MPO/Mercury/EME2000/DY	-1.9042685e+00	-1.9042686e+00	2.0e+08	1.0000000e-03	9.4737919e-09	0.000	-1.00931e-07	0.000 km/sec
State/MPO/Mercury/EME2000/DZ	-1.9448474e+00	-1.9448475e+00	1.6e+08	1.0000000e-03	1.2358284e-08	0.000	-9.85144e-08	0.000 km/sec
Impulse Burn/MPO/OTM0000X/DX	1.1000000e-06	1.0010887e-06	9.5e+02	5.0000000e-06	1.0486401e-09	0.000	-9.89113e-08	0.020 km/sec
Impulse Burn/MPO/OTM0000X/DY	1.1000000e-06	9.9982889e-07	2.1e+03	5.0000000e-06	4.7876934e-10	0.000	-1.00171e-07	0.020 km/sec
Impulse Burn/MPO/OTM0000X/DZ	1.1000000e-06	9.9981269e-07	4.7e+03	5.0000000e-06	2.1214128e-10	0.000	-1.00187e-07	0.020 km/sec

The final solution shows an almost equivalent consider sigma, but still a more consistent solution.

The next case, completes the scenario. An absolute attitude measurement error of 2.5 arc seconds is considered in the filter that provides a slightly higher consider sigma with respect to the Doppler only solution.
The optical weight is consequently changed to a new value of

$$\sqrt{\sigma_{PM}^2 + \sigma_{AME}^2} \approx 1pixel$$

the final solution shows no improvement in the consider sigma solution as expected because of the AME degradation.
The solution is computed using two different image overlapping schemes, the referenced schedule and the sequential schedule the converged delta solution is compatible with 3σ of the true value.

Table 13 Convergence analysis: estimating a state bias with no AME , no PM error and one manoeuver

Doppler

Parameter	BaseNom	Value	/Sigma	Apsig	Sigma	/Apsig	totDelta	/Apsig	Unit
State/MPO/Mercury/EME2000/X		-1.3161243e+02	-1.3161339e+02	3.9e+06	1.0000000e+00	3.3704163e-05	0.000	-9.57153e-04	0.001 km
State/MPO/Mercury/EME2000/Y		1.8917807e+03	1.8917797e+03	2.3e+08	1.0000000e+00	8.3848698e-06	0.000	-9.88627e-04	0.001 km
State/MPO/Mercury/EME2000/Z		-2.4212404e+03	-2.4212414e+03	5.8e+08	1.0000000e+00	4.1641307e-06	0.000	-9.94272e-04	0.001 km
State/MPO/Mercury/EME2000/DX		-6.5781160e-01	-6.5781169e-01	6.1e+07	1.0000000e-03	1.0864264e-08	0.000	-8.60758e-08	0.000 km/sec
State/MPO/Mercury/EME2000/DY		-1.9042685e+00	-1.9042686e+00	2.0e+08	1.0000000e-03	9.4749548e-09	0.000	-8.72326e-08	0.000 km/sec
State/MPO/Mercury/EME2000/DZ		-1.9448474e+00	-1.9448475e+00	1.6e+08	1.0000000e-03	1.2359822e-08	0.000	-1.16435e-07	0.000 km/sec
Impulse Burn/MPO/OTM0000X/DX		1.1000000e-06	1.0004074e-06	9.5e+02	5.0000000e-06	1.0486687e-09	0.000	-9.95926e-08	0.020 km/sec
Impulse Burn/MPO/OTM0000X/DY		1.1000000e-06	1.0000003e-06	2.1e+03	5.0000000e-06	4.7883050e-10	0.000	-9.99997e-08	0.020 km/sec
Impulse Burn/MPO/OTM0000X/DZ		1.1000000e-06	9.9992249e-07	4.7e+03	5.0000000e-06	2.1215288e-10	0.000	-1.00078e-07	0.020 km/sec

Merged reference image schedule

Parameter	BaseNom	Value	/Sigma	Apsig	Sigma	/Apsig	totDelta	/Apsig	Unit
State/MPO/Mercury/EME2000/X		-1.3161243e+02	-1.3161342e+02	3.9e+06	1.0000000e+00	3.3704153e-05	0.000	-9.89549e-04	0.001 km
State/MPO/Mercury/EME2000/Y		1.8917807e+03	1.8917797e+03	2.3e+08	1.0000000e+00	8.3848674e-06	0.000	-9.96992e-04	0.001 km
State/MPO/Mercury/EME2000/Z		-2.4212404e+03	-2.4212414e+03	5.8e+08	1.0000000e+00	4.1641291e-06	0.000	-9.98829e-04	0.001 km
State/MPO/Mercury/EME2000/DX		-6.5781160e-01	-6.5781170e-01	6.1e+07	1.0000000e-03	1.0864260e-08	0.000	-9.71959e-08	0.000 km/sec
State/MPO/Mercury/EME2000/DY		-1.9042685e+00	-1.9042686e+00	2.0e+08	1.0000000e-03	9.4749519e-09	0.000	-9.64653e-08	0.000 km/sec
State/MPO/Mercury/EME2000/DZ		-1.9448474e+00	-1.9448475e+00	1.6e+08	1.0000000e-03	1.2359818e-08	0.000	-1.03834e-07	0.000 km/sec
Impulse Burn/MPO/OTM0000X/DX		1.1000000e-06	9.9914206e-07	9.5e+02	5.0000000e-06	1.0486687e-09	0.000	-1.00858e-07	0.020 km/sec
Impulse Burn/MPO/OTM0000X/DY		1.1000000e-06	1.0002992e-06	2.1e+03	5.0000000e-06	4.7883038e-10	0.000	-9.97008e-08	0.020 km/sec
Impulse Burn/MPO/OTM0000X/DZ		1.1000000e-06	1.0001334e-06	4.7e+03	5.0000000e-06	2.1215287e-10	0.000	-9.98666e-08	0.020 km/sec
Camera Frame/Nadir MPO SC Frame/POINTING ERROR M		0.0000000e+00	0.0000000e+00	0.0e+00	4.0093769e-04	4.0093769e-04	1.000	0.00000e+00	0.000 deg
Camera Frame/Nadir MPO SC Frame/POINTING ERROR N		0.0000000e+00	0.0000000e+00	0.0e+00	4.0093769e-04	4.0093769e-04	1.000	0.00000e+00	0.000 deg
Camera Frame/Nadir MPO SC Frame/POINTING ERROR L		0.0000000e+00	0.0000000e+00	0.0e+00	4.0093769e-04	4.0093769e-04	1.000	0.00000e+00	0.000 deg

Merged sequential image schedule

Parameter	BaseNom	Value	/Sigma	Apsig	Sigma	/Apsig	totDelta	/Apsig	Unit
State/MPO/Mercury/EME2000/X		-1.3161243e+02	-1.3161348e+02	3.9e+06	1.0000000e+00	3.3704160e-05	0.000	-1.04449e-03	0.001 km
State/MPO/Mercury/EME2000/Y		1.8917807e+03	1.8917797e+03	2.3e+08	1.0000000e+00	8.3848693e-06	0.000	-1.01212e-03	0.001 km
State/MPO/Mercury/EME2000/Z		-2.4212404e+03	-2.4212414e+03	5.8e+08	1.0000000e+00	4.1641293e-06	0.000	-1.00586e-03	0.001 km
State/MPO/Mercury/EME2000/DX		-6.5781160e-01	-6.5781172e-01	6.1e+07	1.0000000e-03	1.0864262e-08	0.000	-1.13689e-07	0.000 km/sec
State/MPO/Mercury/EME2000/DY		-1.9042685e+00	-1.9042686e+00	2.0e+08	1.0000000e-03	9.4749538e-09	0.000	-1.13478e-07	0.000 km/sec
State/MPO/Mercury/EME2000/DZ		-1.9448474e+00	-1.9448475e+00	1.6e+08	1.0000000e-03	1.2359821e-08	0.000	-8.32871e-08	0.000 km/sec
Impulse Burn/MPO/OTM0000X/DX		1.1000000e-06	1.0005546e-06	9.5e+02	5.0000000e-06	1.0486687e-09	0.000	-9.94454e-08	0.020 km/sec
Impulse Burn/MPO/OTM0000X/DY		1.1000000e-06	9.9982732e-07	2.1e+03	5.0000000e-06	4.7883048e-10	0.000	-1.00173e-07	0.020 km/sec
Impulse Burn/MPO/OTM0000X/DZ		1.1000000e-06	9.9991437e-07	4.7e+03	5.0000000e-06	2.1215289e-10	0.000	-1.00086e-07	0.020 km/sec
Camera Frame/Nadir MPO SC Frame/POINTING ERROR M		0.0000000e+00	0.0000000e+00	0.0e+00	4.0093769e-04	4.0093769e-04	1.000	0.00000e+00	0.000 deg
Camera Frame/Nadir MPO SC Frame/POINTING ERROR N		0.0000000e+00	0.0000000e+00	0.0e+00	4.0093769e-04	4.0093769e-04	1.000	0.00000e+00	0.000 deg
Camera Frame/Nadir MPO SC Frame/POINTING ERROR L		0.0000000e+00	0.0000000e+00	0.0e+00	4.0093769e-04	4.0093769e-04	1.000	0.00000e+00	0.000 deg

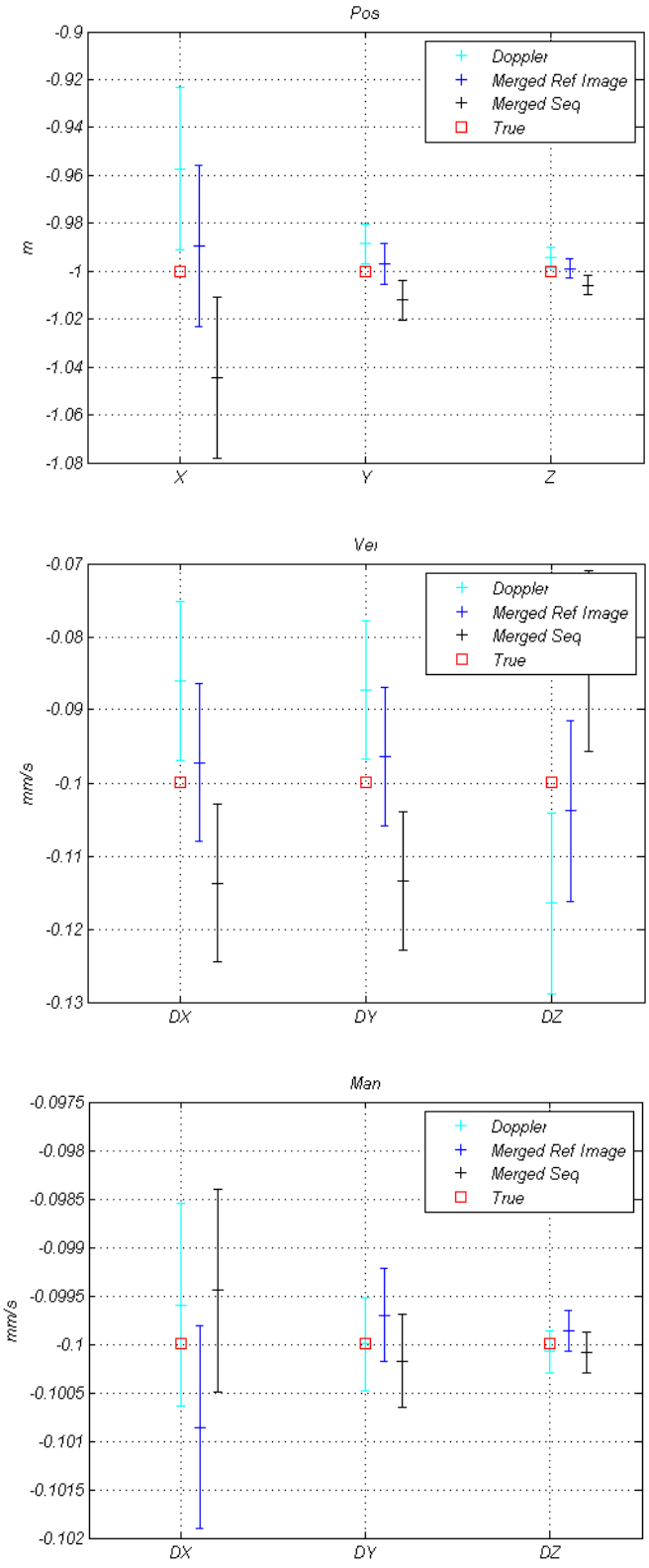

Figure 47 Comparison between Doppler and Merged solutions with sequential and reference image processing

This solution shows no real improvements in terms of delta solution and consider sigma.

9.3.2 Realistic scenario

As seen before the improvements obtained are subtle in an MPO scenario, but it can be hypnotized to reduce the AME to 1 arc second (it can be seen as using a camera with higher resolution or a

condition in which the images are acquired at a lower altitude) and increase the noise due to a less performing radiometric system.
An MPO Like scenario has been prepared, including Two-Way daily X-Band doppler tracking coverage at Canberra with a noise of 5 mHz @1000 s and a malfunction on Two-way daily Ka-Band Doppler tracking coverage at Goldstone.
A desaturation maneuverer has been also planned inside and outside a Doppler tracking coverage pass and optical observables every 8 hours. Red vertical lines indicates manoeuvres that are also covered by one of the two daily tracking passes.

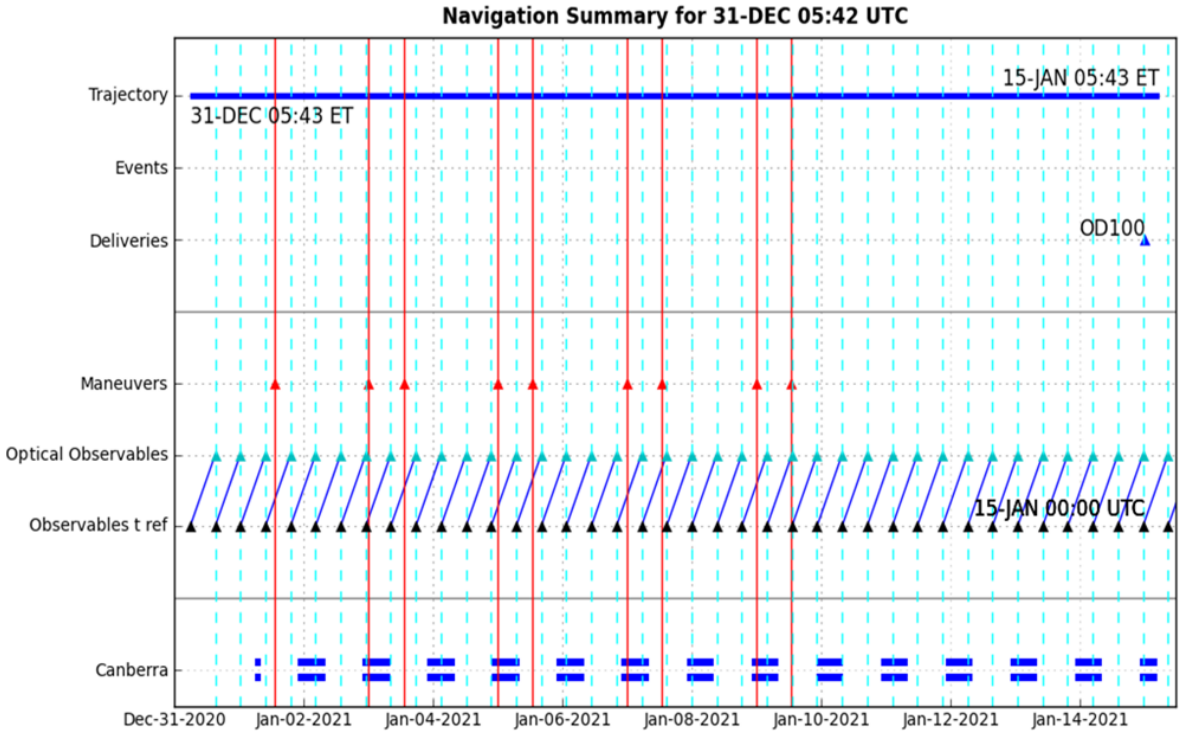

Figure 48 Observations schedule

The following History Plot represents a condition with improvement in the final solution.
The dotted vertical cyan lines indicates the sampling of an optical image, while the solid orange lines indicates manoeuvres.

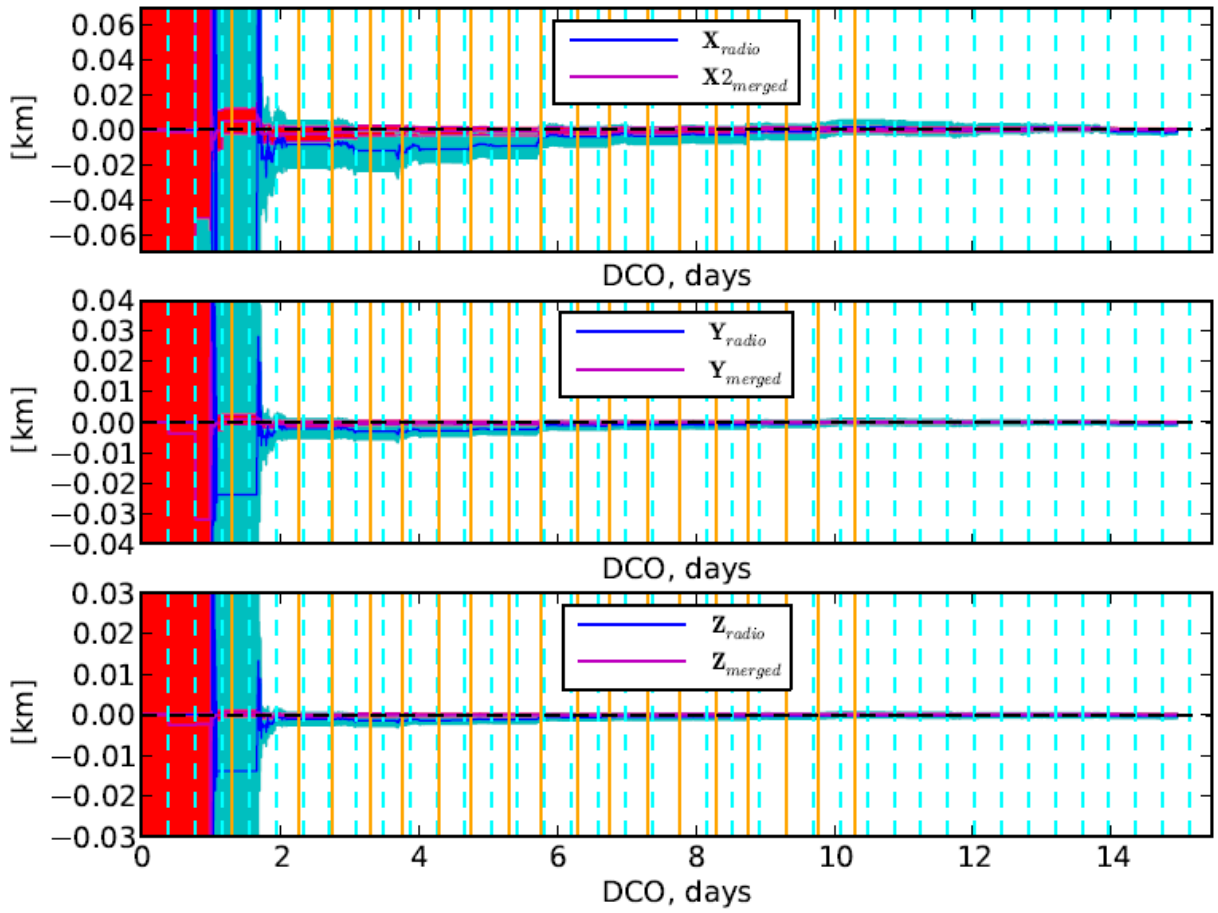

Figure 49 History Plot. in solid yellow are represented the maneuvers times, in dotted cyan the sampled images

This plot shows, as a ratio between the uncertainty of the merged case with respect to the doppler-only case, that there is a strong aid given by the optical observables at the beginning of the filtering process, because no Doppler measurements are present yet, and as radiometric data is processed, this improvement tends to reduce but is still present at the end of the 15 days arc.

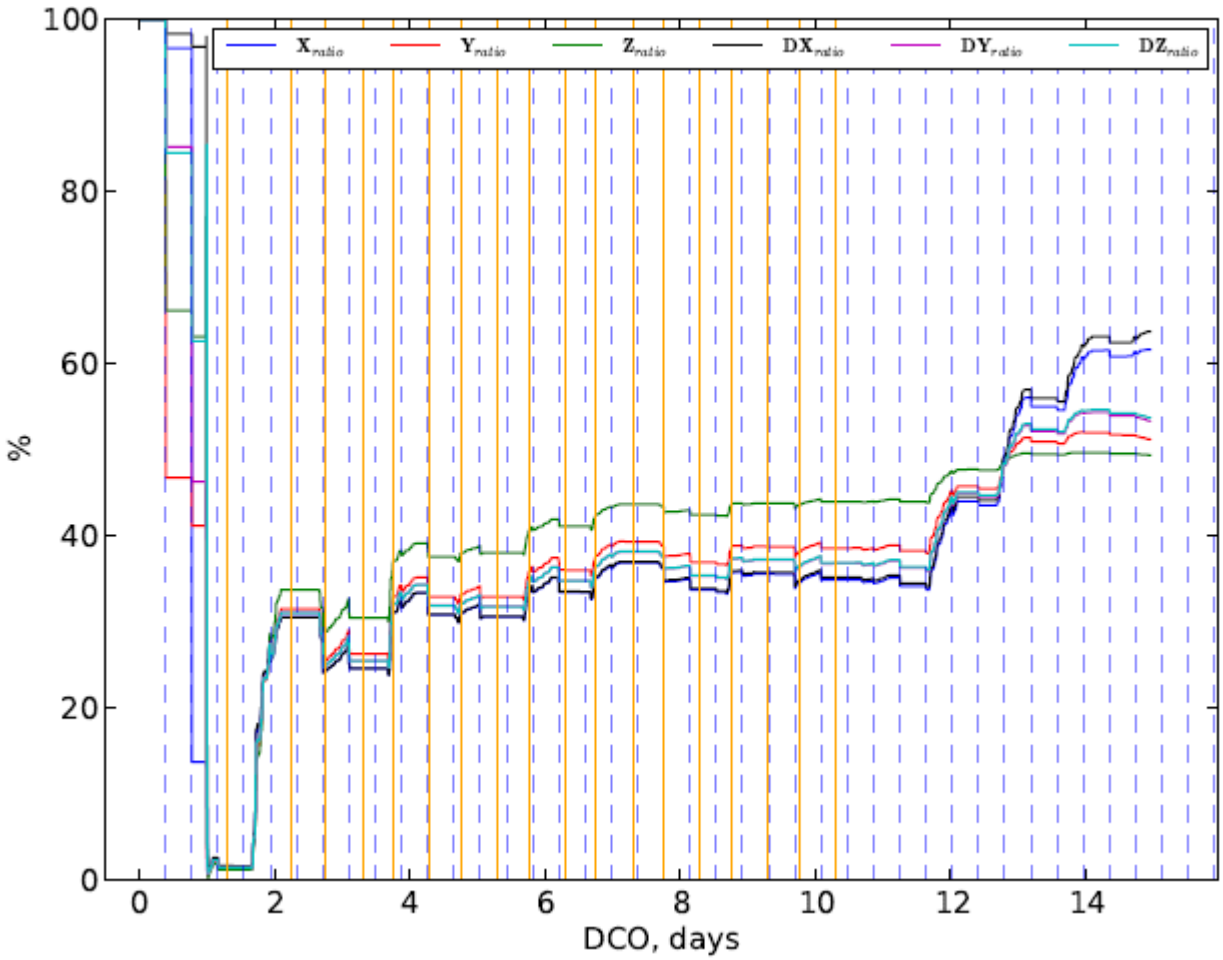

Figure 50 Merged and doppler-only uncertainty ratio as new data arrives

We have observed also that there was a subtle improvement on the estimation of maneuvers (also in this case depending on the attitude pointing error entity) . Where the ratio is computed by:

$$ratio[\%] = \frac{\sigma_{merged}}{\sigma_{doppler}} 100 \quad (161)$$

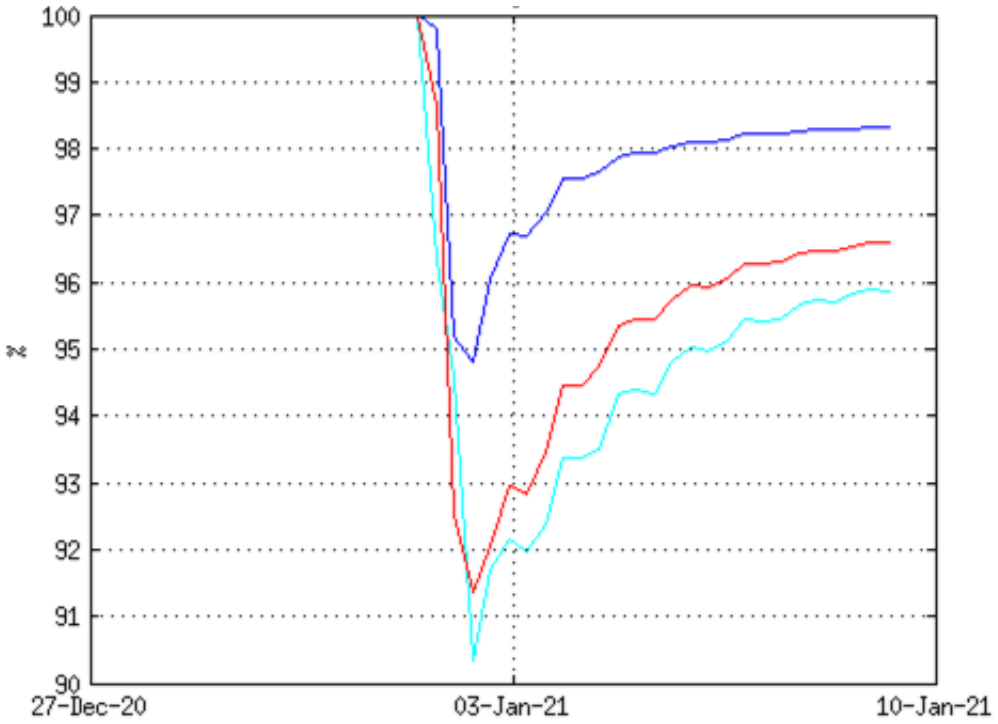

Figure 51 History plot: Maneuver estimation uncertainty

This last plot shows the distribution of optical residuals obtained from the simulation in pixel.

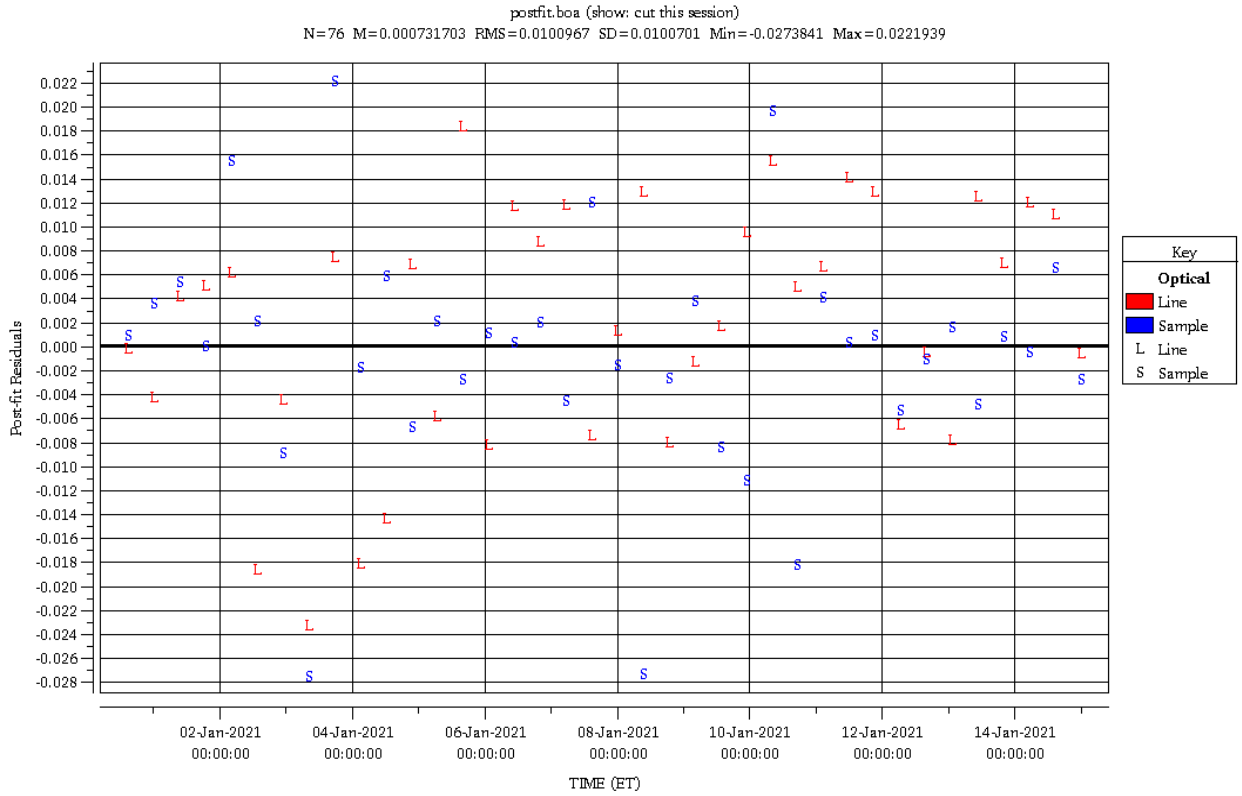

Figure 52 Optical Residuals

10 Conclusions

The basis for this PhD was born from a research of optical navigation introduced in a research that aimed the estimation of the attitude of a LEO terrestrial satellite using the concept of homographic projection between pairs of optical images called STARS (Bevilacqua, 2010). This basic concept has been studied in deep in this research period for a very different function, orbit determination for deep space probes. To propose a new methodology to spacecraft navigation teams, an all-around proof of concept has to be evaluated, therefore this thesis had to space from image generation to acquisition schedules and planning, to covariance analysis and estimation.
A possible expression of the optical observables in an Homography like formulation has been presented and, because of its relative expression between two times, it's not sufficient as a standalone measurement for an automatic navigation system, nor for ground-based navigation systems. The solution was to explore the complementarity due to target-spacecraft relative information given by the presented optical observables with respect to radiometric navigation.
A simulated orbital setup using Cassini and MPO as two reference missions, was designed. For MPO the objective was to have the most similar configuration of the real mission but in this scenario, the radiometric system itself was already at an high performance level.
It was showed that the complementarity is present in case of degradation due to solar plasma due to proximity to solar conjunction (with no MFL) and with concomitant geometric weakness of Doppler measurements. It has been shown how attitude error and pattern matching error are determinant on the usability of this methodology. A slight stabilization effect on the Kalman filter process was also observed.
A final interesting result is about maneuvers executed inside an optical measurement, showing how optical observables are highly sensitive to abrupt changes in orbit trajectory.

A collaboration with DEIS group of the University of Bologna, that provided high resolution synthetic images of the Mercury surface at desired illumination conditions for this methodology, permitted to validate the pattern matching feasibility, following a proposed requirement in terms of schedule of polar images (and consequently of illumination variations) for an hypothetical polar mission to Mercury exploiting this methodology.

Because the filter used for the present research was a Kalman filter, the visualization of the contribute of each new optical observable through time in terms of covariance and corrections could be analyzed step by step. This analysis permitted to observe that also in conditions in which a Merged batch did not improve with respect to an only Doppler batch, the sequential covariance reduction was better. This result gives an interesting hint that his methodology may be useful for automatic spacecraft navigation in which the radiometric link has less coverage or is absent at all.

References

Anon., s.d. Autonomous Optical Navigation (AUTONAV) DS1 Technology Validation Report.

Bay, H., 2008. Speeded-up robust features (SURF).. *Computer Vision and Image Understanding archive.*

Bevilacqua, A., 2010. Standalone Three-Axis Attitude Determination From Earth Images. *AAS.*

Bhaskaran, S., 1996. Autonomous Optical Navigation for Interplanetary Mission.

Bhaskaran, S., 1998. Orbit Determination Performance Evaluation of the Deep Space 1 Autonomous Navigation System.

Bhaskaran, S., 2012. Autonomous Navigation for Deep Space Missions. *SpaceOps.*

Bierman, G., 1977. *Factorization Methods for Discrete Sequential Estimation.* s.l.:Academic Press.

Cheng Yang, 2002. Optical Landmark Detection for Spacecraft Navigation. *AAS,* p. 19.

Cheng, Y., 2003. A Landmark Based Pinpoint Landing Simulator. *7th international symposium of Artificial Automation.*

Cheng, Y., 2005. Landmark Based Position Estimation for Pinpoint. *IEEE.*

Christian, J., 2009. High-Fidelity Measurement Models for Optical Spacecraft Navigation. *University of Texas*.

Christian, J., 2009. Review of Options for Autonomous Cislunar Navigation. *JSR.*

Christian, J. A., 2010. *Optical navigation for a spacecraft in a planetary system.* s.l.:s.n.

Coucaud, C. K. T., 2011. Probabilistic motion estimation for near real-time navigation and landing on small celestial bodies.. *ISSFD.*

Dominigue, D., 2007. *The MESSENGER Mission to Mercury.* s.l.:Springer.

Fluente De La, S., 2013. *BepiColombo MPO Science Operations Planning Drivers.* s.l., s.n.

Gaskell Robert, 2001. Automated landmark identification for spacecraft navigation.

Gaskell Robert, 2003. Optical only determination of small body shape and topography.

Gaskell Robert, 2005. Landmark Navigation and Target Characterization in a Simulated Itokawa Encounter.

Gaskell, R., 2006. Landmark Navigation Studies and Target Characterization in the. *AIAA,* p. 12.

Gaskell, R., 2008. Characterizing and navigating small bodies with imaging data. *Meteoritics & Planetary Science.*

Genova, A., 2012. *The Geodesy of Mercury with the Missions Messenger and BepiColombo.* s.l.:PhD Thesis.

Gherardi, A., 2011. A Simulation Framework to Assess Pattern Matching Algorithms in a Space Mission.

Gillam S., 2008. The planning of optical navigation pictures for the Cassini extended mission. p. 22.

Iafolla, 2010.

Iess, L., 2003. The Cassini Solar Conjunction Experiment:. *IEEE.*

Iess, L., 2012. *ASTRA: Interdisciplinary study of enhancement of the end-to-end accuracy for spacecraft tracking techniques.* s.l., s.n.

Jackman, C., 2013. Optical Navigation capabilities for deep space missions. *AAS.*

Janschek, K., 2006. *Performance Analysis for Visual Planetary Landing Navigation Using Optical Flow and DEM Matching.* s.l., s.n., p. 17.

Jorda, L., 2010. *3D reconstruction of small bodies from in-situ visible images.* s.l., s.n.

Jun'ichiro, K., 1998. An autonomous optical guidance and navigation around asteroids. *Acta Astronautica.*

Knowles, B., 2012. *Cassini ISS Data Users Guide.* s.l.:Space Science Institute.

Konopliv, A., 2001. *A Global Solution for the Gravity Field, Rotation, Landmarks, and Ephemeris of Eros.* s.l., s.n.

Kubota, T., 2006. *Guidance and Navigation Scheme for Hayabusa Asteroid Exploration and Sample Return Mission.* s.l., s.n.
Mariotti, G., 2013. Experimental validation of a dual uplink multifrequency dispersive noise calibration scheme for Deep Space tracking. *Radio Science.*
Mastrodemos, N., 2011. Optical Navigation for Dawn at Vesta. *AAS.*
Meriggiola, R., 2012. *The determination of the rotational state of celestial bodies.* Rome: PhD Thesis.
Milani, A., 2001. Gravity field and rotation state of Mercury from the BepiColombo Radio Science Experiments. *PSS.*
Misu, T., 1998. Optical Guidance for Autonomous landing of Spacecraft. *IEEE.*
Moyer, T., 2000. *Mathematical formulation of the DPODP.* s.l.:s.n.
Moyer, T., s.d. *Formulation for Observed and Computed Values of Deep Space Network Data Types for Navigation.* s.l.:JPL.
Munoz, P., 2012. *Preparations and strategy for navigation during Rosetta comet Phase.* s.l., s.n.
Owen, W., 2001. NEAR Optical Navigation at Eros.
Owen, W., 2003. *Interplanetary Optical Navigation 101.* s.l., s.n., p. 57.
Owen, W., 2011. Methods of Optical Navigation. *AAS,* p. 19.
Owen, W., 2012. *Optical Navigation preparations for New Horizons Pluto Flyby.* s.l., JPL.
Palli, A., 2012. *Design And Implementation Of An End-To-End Simulator For The BepiColombo Rotation Experiment.* Bologna: PhD Thesis.
Pfyffer, G., 2010. *Libration and obliquity of Mercury from the BepiCOlombo radio science and camera experiments.* s.l.:PhD Thesis.
Riedel, J., 1989. Optical Navigation durint the Voyager Neptune Encounter.
Riedel, J., 2000. *Using Autonomous Navigation for Interplanetary Missions: Mission Operations with Deep Space 1 Autonav.* s.l., s.n.
Shi, J., 1994. Good Features to Track. *IEEE.*
Shuang, L., 2007. Vision-aided inertial navigation for pinpoint planetary landing. *Elsevier.*
Silvestri, D. & Paolo, T., 2012. *Enhancement of trajectiory Determination of Orbiter Spacecraft by using Planetary Optical Images.* Noordwijk, s.n.
Stastny N., 1998. Autonomous Optical Navigation at Jupiter : A Linear Covariance Analysis. p. 18.
Stiles, B., 2008. Determining Titan surface topography from Cassini SAR data. *Elsevier.*
Tapley, B., 2004. *Statistical Orbit Determination.* s.l.:s.n.
Thornton, C., s.d. *Radiometric Tracking Techniques for Deep-Space Navigation.* s.l.:JPL.
Tomasi, C., 1991. *Detection and Tracking of Point Features,* s.l.: s.n.
Tortora, P., 2003. *The Cassini Multifrequency Link Performance During 2002 Solar Conjunction.* s.l.:s.n.
Tortora, P., 2011. *Simulation of BepiColombo's Mercury Rotation Experiment.* s.l., s.n.
Williams, P., 2008. Orbit Control Operations for the Cassini-Huygens Mission. *SpaceOps.*
Zusi, M., 2009. *The High Resolution Imaging Channel of the SIMBIO-SYS suite aboard the BepiColombo mission to Mercury.* s.l.:PhD Thesis.

Appendix: Attitude errors modeling

The following operations are used for the formulation of attitude errors in the optical models.

A single axis rotational error (infinitesimal matrix) can be expressed as

$$E_z = \begin{bmatrix} cos\epsilon & -sin\epsilon & 0 \\ sin\epsilon & cos\epsilon & 0 \\ 0 & 0 & 1 \end{bmatrix} \cong \begin{bmatrix} 1 & -\epsilon & 0 \\ \epsilon & 1 & 0 \\ 0 & 0 & 1 \end{bmatrix} = I + \begin{bmatrix} 0 & -\epsilon & 0 \\ \epsilon & 0 & 0 \\ 0 & 0 & 0 \end{bmatrix} = I + \epsilon^x \quad (162)$$

If a single axis infinitesimal rotation error is applied sequentially to three axes it is obtained

$$E = E_z E_y E_x = \begin{bmatrix} 1 & -\gamma & 0 \\ \gamma & 1 & 0 \\ 0 & 0 & 1 \end{bmatrix} \begin{bmatrix} 1 & 0 & \beta \\ 0 & 1 & 0 \\ -\beta & 0 & 1 \end{bmatrix} \begin{bmatrix} 1 & 0 & 0 \\ 0 & 1 & -\alpha \\ 0 & \alpha & 1 \end{bmatrix} = \{I + \gamma^x\}\{I + \beta^x\}\{I + \alpha^x\} \quad (163)$$

Noticing that holds

$$\gamma^x \alpha^x = 0 \quad (164)$$

$$\{I + \gamma^x\}\{I + \alpha^x\} = I + \gamma^x + \alpha^x \quad (165)$$

And a compact notation is obtained

$$E_z E_y E_x = I + \gamma^x + \beta^x + \alpha^x = I + [\boldsymbol{\epsilon}]_\times \quad (166)$$

Where the term $[\boldsymbol{\epsilon}]_\times$ is the anti-symmetrical operator, sometimes given with the following notation S($\boldsymbol{\epsilon}$)

$$S(\boldsymbol{\epsilon}) = [\boldsymbol{\epsilon}]_\times = \begin{bmatrix} 0 & -\gamma & \beta \\ \gamma & 0 & -\alpha \\ -\beta & \alpha & 0 \end{bmatrix} \quad (167)$$

$\boldsymbol{\epsilon}$ must be a vector with the following useful properties

$$S^T(\boldsymbol{\epsilon}) = -S(\boldsymbol{\epsilon}) = S(-\boldsymbol{\epsilon}) \quad (168)$$

And the notable property

$$S(\boldsymbol{\epsilon})\boldsymbol{v} = \boldsymbol{\epsilon} \times \boldsymbol{v} \quad (169)$$

$$\boldsymbol{\epsilon} \times \boldsymbol{v} = [\boldsymbol{\epsilon}]_\times \boldsymbol{v} = [\boldsymbol{v}]_\times^T \boldsymbol{\epsilon} \quad (170)$$

Then $S(\boldsymbol{\epsilon})$ is the operator $\boldsymbol{\epsilon} \times$.

$$\boldsymbol{\epsilon} = \begin{bmatrix} \alpha \\ \beta \\ \gamma \end{bmatrix} \quad (171)$$

And a three axis rotation can be written as

$$[e]_X v = e \times v \quad (172)$$

where

$$e \times v = det \begin{bmatrix} i & j & k \\ ex & ey & ez \\ vx & vy & vz \end{bmatrix} = \begin{bmatrix} eyvz - ezvy \\ ezvx - exvz \\ exvy - eyvx \end{bmatrix} \quad (173)$$

Or with the three axis skew symmetric notation

$$[e]_X v = \begin{bmatrix} 0 & -ez & ey \\ ez & 0 & -ex \\ -ey & ex & 0 \end{bmatrix} \begin{bmatrix} vx \\ vy \\ vz \end{bmatrix} \quad (174)$$

ϵ^x is the one axis skew symmetric

$$E_y = \begin{bmatrix} cos\epsilon & 0 & sin\epsilon \\ 0 & 1 & 0 \\ -sin\epsilon & 0 & cos\epsilon \end{bmatrix} \cong \begin{bmatrix} 1 & 0 & \epsilon \\ 0 & 1 & 0 \\ -\epsilon & 0 & 1 \end{bmatrix} = I + \begin{bmatrix} 0 & 0 & \epsilon \\ 0 & 0 & 0 \\ -\epsilon & 0 & 0 \end{bmatrix} = I + \epsilon^x \quad (175)$$

Where ϵ is modeled as a bias, gain and zero mean white noise

$$\epsilon(t) = \epsilon_0 + \mathrm{e_G} + \tilde{\epsilon}(\mathrm{t}) \quad (176)$$

The inverse is then

$$[e]_X = \begin{bmatrix} 0 & -ez & ey \\ ez & 0 & -ex \\ -ey & ex & 0 \end{bmatrix} \quad (177)$$

$$E = I_3 - [e]_X \quad (178)$$

$$E^T = I_3 + [e]_X \quad (179)$$

A derivative can be computed using the notations expressed before

$$\mathbb{T}_{BN}^B = \{I - [\boldsymbol{\epsilon}]_\times\} \quad (180)$$

$$\mathbb{T}_I^B = \mathbb{T}_{BN}^B \mathbb{T}_I^{BN} \quad (181)$$

$$R^B = \mathbb{T}_I^B R^I \quad (182)$$

$$\frac{\partial R^B}{\partial \boldsymbol{\epsilon}} = \frac{\partial}{\partial \boldsymbol{\epsilon}} \{-[\boldsymbol{\epsilon}]_\times \mathbb{T}_I^{BN} R^I\} \quad (183)$$

Applying the following property:

$$[\boldsymbol{\epsilon}]_\times \boldsymbol{v} = [\boldsymbol{v}]_\times^T \boldsymbol{\epsilon} \quad (184)$$

$$\frac{\partial R^B}{\partial \boldsymbol{\epsilon}} = \frac{\partial}{\partial \boldsymbol{\epsilon}}\{-[\boldsymbol{\epsilon}]_\times\}\} = [\mathbb{T}_I^{BN} R^I]_\times^T \frac{\partial(-\boldsymbol{\epsilon})}{\partial \boldsymbol{\epsilon}} = -[\mathbb{T}_I^{BN} R^I]_\times^T \begin{bmatrix} 1 \\ 1 \\ 1 \end{bmatrix} = -[\mathbb{T}_I^{BN} R^I]_\times^T = [\mathbb{T}_I^{BN} R^I]_\times \quad (185)$$

The last passage is obtained using the property of anti-symmetric matrix and implicitly using the anti-symmetric operator on [1;1;1] if nothing is applied:

$$S^T(\boldsymbol{v}) = -S(\boldsymbol{v}) \quad (186)$$